GEO-3900

Master's Thesis in Geology

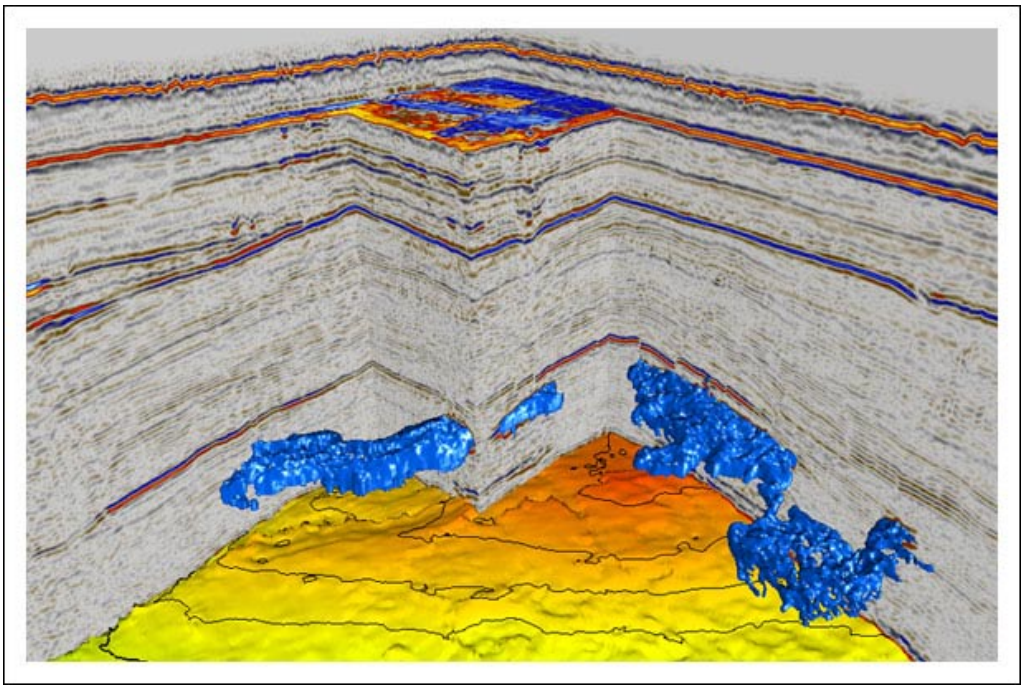

OCCURRENCE OF FREE GAS AND FOCUSED FLUID FLOW SYSTEMS IN THE VESLEMØY HIGH AREA, SW BARENTS SEA

Gustav Pless

Tromsø, May, 2009

Faculty of Science

Department of Geology

University of Tromsø

GEO-3900

Master's Thesis in Geology

OCCURRENCE OF FREE GAS AND FOCUSED FLUID FLOW SYSTEMS IN THE VESLEMØY HIGH AREA, SW BARENTS SEA

Gustav Pless

Tromsø, May, 2009

Occurrence of free gas and focused fluid flow systems in the Veslemøy High area, SW Barents Sea

GUSTAV PLESS

The Faculty of Science – Department of Geology – University of Tromsø, Dramsveien 201, 9037 Tromsø, Norway

---

ABSTRACT

The high-resolution 3D seismic survey EL0001 allowed to document the subsurface fluid migration system and fluid accumulations within Veslemøy High, SW Barents Sea. Fluids migrate both through Cretaceous and Tertiary sediments, but also through younger glacial sediments. Veslemøy High is a structurally isolated high at the Cretaceous and Tertiary levels bounded by N-S trending west-dipping normal faults. Cretaceous to Miocene sediments that consists of deep marine shales dominate in the older part and Plio-Pleistocene successions deposited by glaciomarine processes dominate in the upper part.

Fluid accumulations are identified in L. Paleocene to E. Eocene sediments, and in Pliocene to Pleistocene sediments of glacial origin. An extensive high-seismic amplitude anomaly of 790 km^2 appears to occur in a fan system within the eastern section of the 3D survey extending into Tromsø Basin. High and negative seismic amplitudes indicate appreciable gas accumulations within the fan. On the seafloor the existence of pockmarks suggest that pockmark formation most likely occurred after the ice-sheet retreat and thus between 15 ka and 12.5-11.5 ka. Pockmarks may represent fluid flow events from violent eruptions associated with deglaciation processes.

Some evidence exists that gas may have been generated in deeper basins. Fluids migrated into Veslemøy High primarily along Plio-Pleistocene strata from Sørvestsnaget Basin in the west and along Creataceous-Paleogene strata from Tromsø Basin in the east. As the fluids reach the apex of Veslemøy High vertical migration through giant chimneys and along normal faults dominate. It is important to note that there is no geophysical evidence for fluid migration from Cretaceous sediments that lie directly below the high.

Keywords: Veslemøy High, fluid migration, pockmarks

ACKNOWLEDGEMENTS

This thesis is part of a research project funded by the Norwegian Research Council, called PetroMAKS. The project is led by Professor Doctor Jürgen Mienert of the University of Tromsø and is a cooperation between several research institutions in Norway and abroad. The project focuses on “Refinement of Geophysical methods to improve surveys of basin prospects” and “Development of products to enhance prediction of basin scale vertical fluid flow”.

I wish to express my gratitude to my supervisor Prof. Dr. Jürgen Mienert for helping me with guidance and constructive criticism during this master thesis project, and also to my co-supervisor Ass. Prof. Dr. Stefan Bünz for criticism, guidance and re-processing of the seismic data.

I am also thankful for help provided by StatoilHydro Harstad associated to the wells, Petrobank and openly sharing their knowledge of the study area.

I have had great use of, and fun discussing the geological and geophysical problems encountered with my fellow master- and Phd-students, especially Leif Egil Holbæk-Hanssen and Iver Martens, but also Steinar Hustoft, Sten-Andreas Grundvåg, Wiktor Weibull, Jorge Sanchez Borque, Harald Hansen and Rune Mattingsdal amongst others.

I would also like to thank Runar, Tom Arne, Kristina, Hilde, Jon, Linn, Mads, Kari and the rest of the students at Brakke Sør for the coffee breaks and good times.

Thanks to my family at home for supporting me and my friends in Tromsø for making my 5 years in Tromsø fantastic. Last but not least I would like to thank Anne Mette for everything.

Table of Contents

1 INTRODUCTION

1.1 Objective

The objective of this master thesis is to contribute to a better understanding of geological controls on fluid-migration and accumulation in the area of Veslemøy High in the southwestern Barents Sea. Part of the work consists of visualizing fluid migration using 3D seismic data that encompass sedimentary rocks of Cretaceous and Tertiary age, but also younger glacial sediments on top. Another part of the work concentrates on fluid and gas accumulations beneath glacial sediments that resemble shallow gas reservoirs. Finally, an understanding is to be developed for how sedimentary strata and tectonic developments affect fluid migration in the study area.

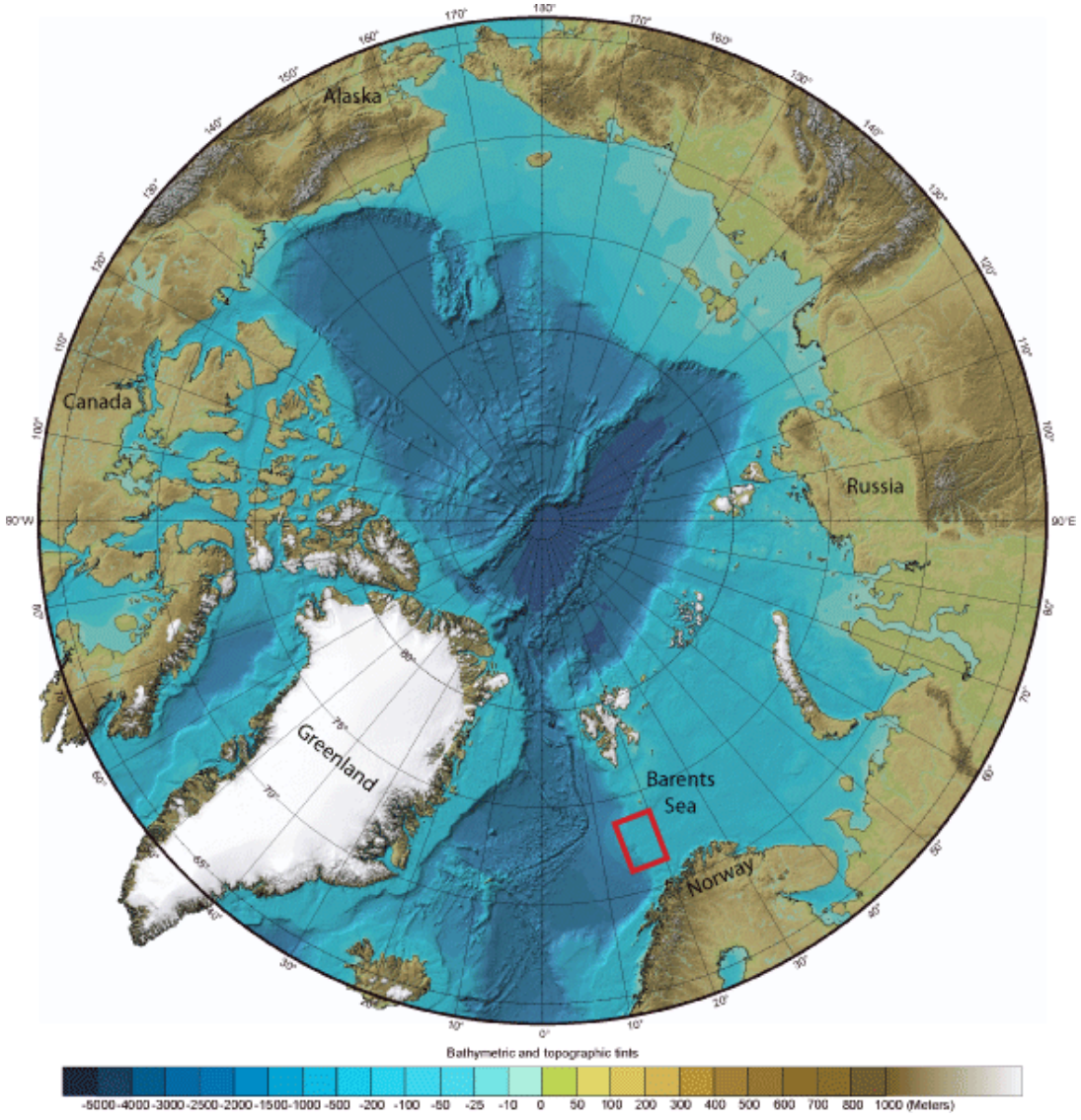

Figure 1.1 Map of the Arctic Sea. Approximate location of study area marked in red. Map from IBCAO (Jakobsson et al., 2008).

1.2 Background - Petroleum Fluid Migration

Fluid flow and accumulation is a subject of interest to both the petroleum industry and academia for several reasons: (1) its presence and associated features can be used as an indicator of deeper prospective reservoirs (Heggland, 1998), (2) gas in shallow sediments may be of commercial interest in the future (Carstens, 2005), (3) shallow-gas accumulations, may reduce the shear strength of the sediments, and pose a hazard to hydrocarbon exploration and development both through mass movements and when drilling, (4) methane escaping into the atmosphere affects the climate, methane is the second most important greenhouse gas and accounts for 15–20% of the radiative forcing added to the atmosphere (IPCC, 1996)

Technological developments during recent years led to the discovery of numerous focused fluid flow systems and the morphological expression of the seabed. Mapping the fluid flow systems is important for understanding their spatial and temporal evolution.

Petroleum fluid migration is divided into two main stages. *Primary migration* out of the source rock that occurs simultaneously with the generation of fluids (Bjørkum and Nadeau, 1998; Aydin, 2000). *Secondary migration* within porous and permeable pathways into an accumulation area or from the seabed into the water column.

Fluid flow is controlled by rock physical properties such as capillary entry pressure, hydraulic conductivity and wettability, and by seal bypass systems (Cartwright et al., 2007). Fractured driven flow is often considered the most common bypass mechanism..

As the solubility of methane and CO_2 rises rapidly with increasing pressure the transportation of fluids dissolved in water depends on depth beneath the seafloor. This thesis will concentrate on secondary migration only, i.e. the migration after hydrocarbons have migrated out of the source rock.

1.2.1 Fluid flow dynamics

Darcy's law explains why fluids flow along a hydrodynamic gradient, i.e. from higher to lower pressures. The fluid flux increases with increasing permeability and/or pressure difference and decreases with increased viscosity.

$$F = k * \frac{\Delta P}{\mu} \qquad \text{(Equation 1.1)}$$

F= Fluid flux [m^3/s] μ= Viscosity

k= Permeability [mD] ΔP= Pressure

Pressure differences can be caused, for example by differential compaction and sedimentation, generation of deep thermogenic and shallow biogenic gas in the subsurface. Permeable sediments allow equalizing the formation to hydrostatic pressure if the pressure generation is slower than fluid flux. In contrast, impermeable sediments may retain overpressures over long periods of time. The hydrostatic pressure is equal to the force exerted by the overlying water column:

$$P = \rho g h \qquad \text{(Equation 1.2)}$$

ρ= Density [kg/m^3]
g= The gravity constant [m/s^2]
h= Height of water column [m]

Overpressure is any pressure exceeding the hydrostatic pressure. As overpressure builds up, fluids show a tendency to enhance the permeability of weak zones with hydro fracturing in order to release pressure and reach an equilibrium state (Berndt, 2005; Hustoft et al., 2007). Fluid flow changes from diffuse to focused. Overpressure may build up until it reaches the fracturing pressure, approximately 70-80% of the lithostatic pressure (Swarbrick et al., 2002; Bünz and Mienert, 2004). Fractured fluid flow pathways can be active for long periods of time (Berndt et al., 2003) or they can only be temporarily active over long periods of time, and such are called episodic fluid expulsions that later become sealed. However, oil and gas (even in liquid form) are less dense then water which makes buoyancy one of the driving factors of migration. Fluids may migrate both in gaseous and liquid phase. Buoyancy increases with increasing density gradients between fluids. Buoyancy enables fluids with lower densities then water to migrate against the hydrodynamic gradient, i.e. in the opposite direction to water flow (Figure 1.2).

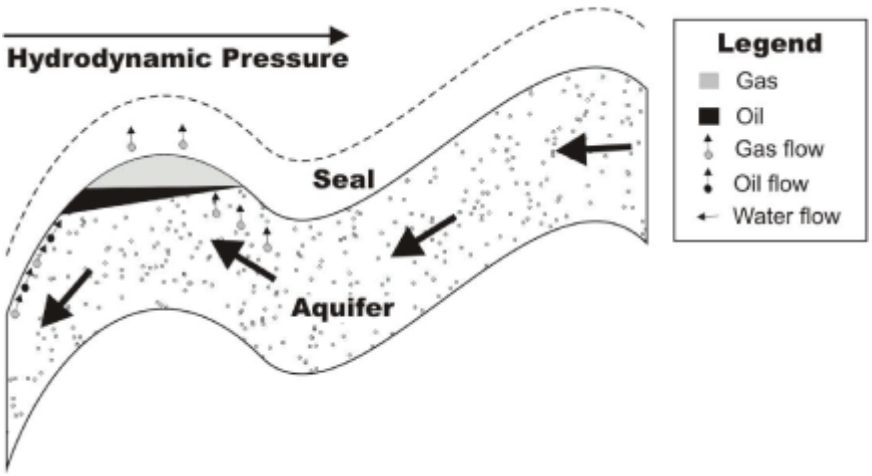

Figure 1.2 Conceptual model of fluid flow where aquifer movement is controlled by the pressure potential field, in contrast low density fluids like gas and oil move up dip due to buoyancy. (After Perrodon, 1983; Weibull, 2008).

1.2.2 Seal bypass systems

Seal bypass systems are defined as seismically resolvable geological features embedded within sealing sequences. They promote cross-stratal fluid migration and allow fluids to bypass the pore network (Cartwright et al., 2007).

Faults, with fracture flow as main mechanism, are the largest group of seal bypass systems. Faults can be the main conduits for fluid flow, especially at greater depths where sediments have become more consolidated or completely lithified (Ligtenberg, 2005). However faults may also act as traps in otherwise permeable sediments (Linjordet and Olsen, 1992). An active, or recently active fault is more likely to act as a conduit for fluid flow then a non active fault i.e. faults most likely act as fluid conduits during active rupture events (Sibson, 1981; Muir, 1994; Hickman et al., 1995). How well a fault may act as a fluid conduit depends also on the age and the burial process since it was created, and the sealing of the fault (Fisher et al., 2003).

A fault can be divided into a fault core, a damage zone and a protholith (Caine, 1996)(Figure 1.3). The fault core is the portion of the fault where most displacement is accommodated. The core consists of fine grained cataclasite-ultracataclasite or phyllonite. While the damage zone is a network of subsidiary structures the protholith is the unaffected rock. Fault cores often act as a conduit for fluid flow during deformation but then become cemented and sealed due to increasingly low permeability. Damage zones are often the conduit if compared to both the fault core and the protholith. The damage zone's permeability is fracture dominated (Caine, 1996). Permeabilities estimated from modeling and laboratory measurements range from 10^{-13}

to 10^{-20} m^2 (1013 mD-0,0001 mD) with higher permeabilities generally associated with the damage zone (Bruhn et al., 1994; Evans et al., 1997; Seront et al., 1998).

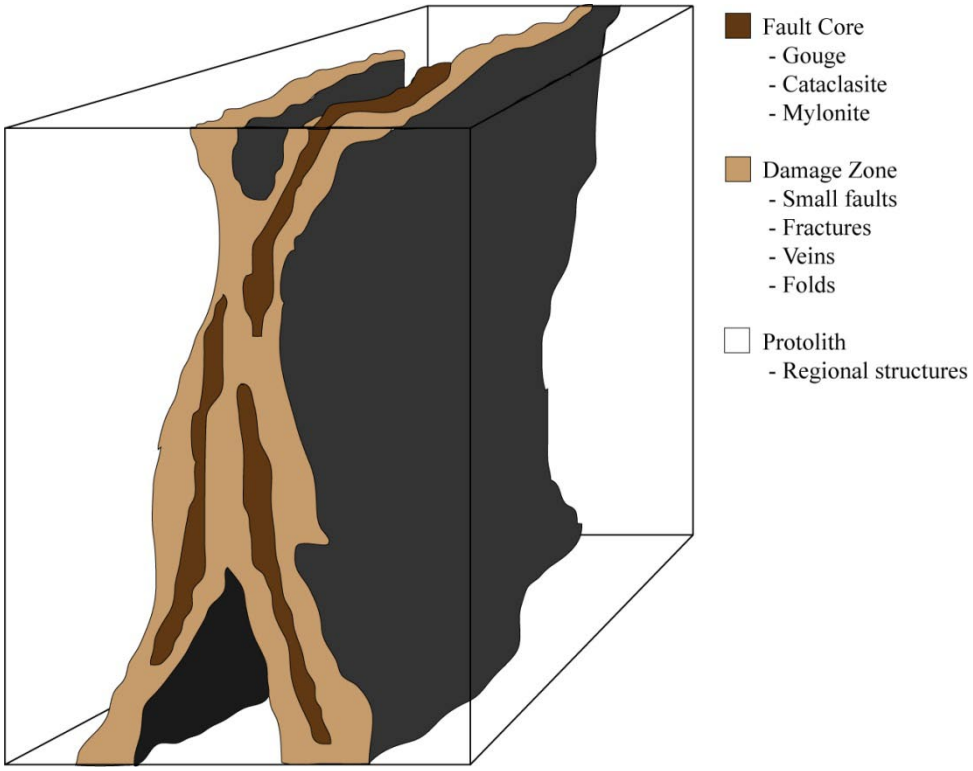

Figure 1.3. Conceptual model modified from Caine et al. (1996) of fault zone with protolith removed. (After Chester and Logan, 1986; Smith et al., 1990)

Regional stress directions and its implications for fault seal

The orientation of the maximum horizontal principal stress is of importance for estimating which faults are closed and which are open for fluid migration. Crustal stress orientations have been inferred from borehole breakout data (Gölke and Brudy, 1996). In the Barents Sea, the horizontal principal stress orientation is approximately N 177°. In the well 7219/9-1, located east of EL0001, the orientation is 164° ± 15° (Gölke and Brudy, 1996). The regional pattern of tectonic stress in the Barents Sea is thought to be related to forces associated with a ridge push. The forces are generated along the Mid-Atlantic ridge and its continuation along the Gakkel Ridge in the arctic. The stresses are N-S trending in the Barents Sea and E-W trending along the mid Norwegian Margin and further south on the European Atlantic margin. (Mueller et al., 1992; Gölke and Coblentz, 1996).

In theory the faults aligned along the regional stress direction (N-S in the Barents Sea) will have a greater tendency for being permeable than faults aligned perpendicular to the stress

direction. N-S trending faults are likely to experience movement along the fault-plane and E-W trending faults are likely to be closed by the forces.

Intrusive bypass

Intrusions may breach the seal in three distinctive ways (Cartwright et al., 2007). First, the intrusion itself may contain the fluids, for example when mud volcanoes form. Second, the intruded material has a much higher permeability then the sealing sequence and acts as a bypass, for example sandstone intrusions. Third, the intrusive event results in fracturing and deformation of the sealing sequence, for example in the sheet zone around salt diapirs. Salt diapirs occur frequently in the areas surrounding Veslemøy High, and are shown to be associated with fluid flow (Andreassen et al., 2007a). The growth of salt diapirs commonly involves folding of overburden and surrounding sediments and radial and concentric faulting. Complex fracture networks are formed in the sheath of drag folds in the contact zone between the salt diapir and the surrounding sediments and immediately above the crest of the diapir. The fracture network may work as conduits for hydrocarbon fluids (Davison et al., 2000). Salt diapirs are however a common trap, it is therefore hypothesized that the fracture systems surrounding salt diapirs is becoming sealed shortly after its generation (Davison et al., 2000).

Pipe bypass

Pipes, being features of small lateral extent, have been difficult to map without high-resolution 3D seismic data. They can be described as columnar zones of disturbed reflections on seismic data. They are commonly seen to originate from crestal regions, e.g., tilted fault block crests, fold crests, or crests of sand bodies with positive topography, which could be the natural path for fluid flow in vertically homogenous strata. Due to the often strong acoustic masking and their vertical structure it appears difficult to identify at which depth they originate (Løseth et al., 2008). Pipe structures are highly variable and poorly understood. They may display deformed formations, acoustic pull-down or pull-up effects, stacked pockmark craters, doming and localized strong amplitude anomalies.

1.2.3 Seismic indications of hydrocarbon

Hydrocarbons can be recognized in seismic data in a number of ways. Seismic reflections are a result of acoustic impedance (AI) changes; AI is a product of density and P-wave velocity. It has been shown that even small quantities of gas in sediment drastically reduce its P-wave velocity (Domenico, 1974, 1977). The change in P-wave velocity combined with density

differences can be observed in seismic data in different ways. Bright spots, dim spots, flat spots, phase reversal, velocity sag, low frequency shadow, amplitude shadow and gas chimney/pipe, are all considered to be direct hydrocarbon indicators (DHIs) (Sheriff, 2006).

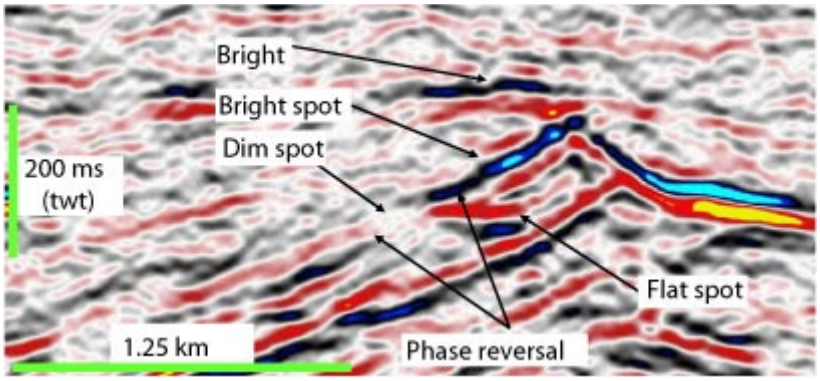

Figure 1.4. Bright spots, dim spots, flat spots and phase reversal are considered hydrocarbon indicators and may suggest the presence of hydrocarbon in a reservoir. (Figure from Løseth et al., 2008)

A *bright spot* is the reflection from the top of a gas bearing zone, it is an area of stronger amplitudes then surrounding data, an *amplitude anomaly*. It is characterized by a negative reflection coefficient. Bright spots located on scattered reflections along a fault are often referred to as *flags*.

A *dim spot* is also a reflection from the top of a gas bearing zone but in this case the gas is contained in the pore space of sediments with much higher AI then overlying sediments. This would give a strong reflection except for where gas is present, at such a locality the reflection would be weaker or dim.

A *flat spot* is the reflection from the gas-water/oil-water contact. It is horizontal or sub-horizontal and has a positive reflection coefficient.

Phase reversal is when a reflector changes laterally from a positive polarity to a negative polarity. This may be an indication of hydrocarbons as sediments containing hydrocarbons have a significantly lower AI.

The lower velocity of sediments containing gas leads to longer two-way times (TWT) and causes underlying reflections to sag below hydrocarbon accumulations, this is known as *velocity sag* and is the same effect as *push-down* or *pull-down*. Pull-up can be the opposite effect of push-down only now the reflectors are overlain by a large high velocity zone, for example salt.

Low frequency shadow, *amplitude shadow* and gas chimney/pipe can be grouped under *acoustic masking* which refers to areas with highly distorted amplitude and phase of the

reflectors. This is because acoustic energy is absorbed and scattered by hydrocarbons. Vertical zones of acoustic masking have been referred to as *seismic chimneys* (Heggland, 1997, 1998). Narrower circular zones of acoustic masking have been referred to as *acoustic pipes*. Pipes can be further subdivided into blowout, seepage, hydrothermal and dissolution pipes (Cartwright et al., 2007). Blowout pipes have been defined as "cylindrical or steeply conical zones of intense disruption of stratal reflections typically developed directly above localized breach points of underlying fluid source interval; linked to pockmarks; disturbed amplitude anomalies are common" (Cartwright et al., 2007). Seepage pipes are defined as for blowout pipes but they have no link to pockmarks. Pipes and chimneys can be associated with both push-down and/or pull-up effects.

The flanks of pipes may show pull-up effects (Hustoft et al., 2007). The cause of this deformation has been interpreted as a combination of a high velocity due to high velocity material in the flanks of the chimneys. For example, carbonate cementation or gas hydrate can be associated with the pull-up formation of the chimney (Westbrook, 2008). When the pull-up effect is not due to a velocity effect but due to sediment deformation it has been referred to as intrasedimentary doming (Judd, 2007). It is thought to be caused by vertical sediment movements due to upwards fluid flow.

1.2.4 Gas hydrates

When methane-laden fluids reach the shallow geosphere and here the gas hydrate stability zone (GHSZ), gas hydrates may form. Gas hydrates are ice-like crystals that form from low-molecular weight gas and water molecules. 1 m3 of hydrates may contain as much as 180 m3 of gas under standard temperature and pressure (STP) conditions (Sloan, 1998). Four conditions are necessary in order to form gas hydrates; 1) adequate gas molecules to form the hydrate, 2) sufficient water molecules to form the hydrate, 3) a temperature within the hydrate phase equilibrium region, and 4) a pressure within the hydrate phase equilibrium region. If these four conditions are met gas hydrates can form within the GHSZ. Factors contributing to the determination of GHSZ thickness are amongst others; ocean bottom water temperature, geothermal gradient, salinity of the formation water, composition of gas, pressure and varying sea level (Sloan, 1990; Bünz and Mienert, 2004).

The gas hydrate stability conditions in the SW Barents Sea was modeled to identify the GHSZ in 3D seismic data (Chand et al., 2008). The results show that the gas hydrate stability zone in the Barents Sea region is highly variable and controlled by the percentage of higher order

hydrocarbon gases, heat flow and salt tectonics. Local variations in bottom water temperature play a less important role. The GHSZ was presumably distinctly increased during glacial times due to high pressure and low temperature beneath the Barents Sea ice sheet. Extensive melting of gas hydrates was suggested to accompany the period of warming after the last glacial maximum (LGM). Figure 1.5 displays gas hydrate stability zone (GHSZ) thickness variations for different geothermal gradient and gas compositions. A higher geothermal gradient leads to a thinner GHSZ, and a higher percentage of higher order hydrocarbon gases lead to a thicker GHSZ. These variables suggest a GHSZ thickness of 0-200 m in Veslemøy High. Gas hydrates in sediments will, if the concentration of hydrates in the pore space of sediments is high enough, increase the interval P-wave velocity. At the base of the GHSZ gas hydrates are no longer stable and the sediments will contain free gas instead of gas hydrates. This causes a large velocity decrease and a negative acoustic impedance contrast, thereby creating a strong reflection with a phase reversal compared to the seafloor reflection. This phase reversal is often found to mimic the seafloor and it is therefore named Bottom Simulating Reflector (BSR).

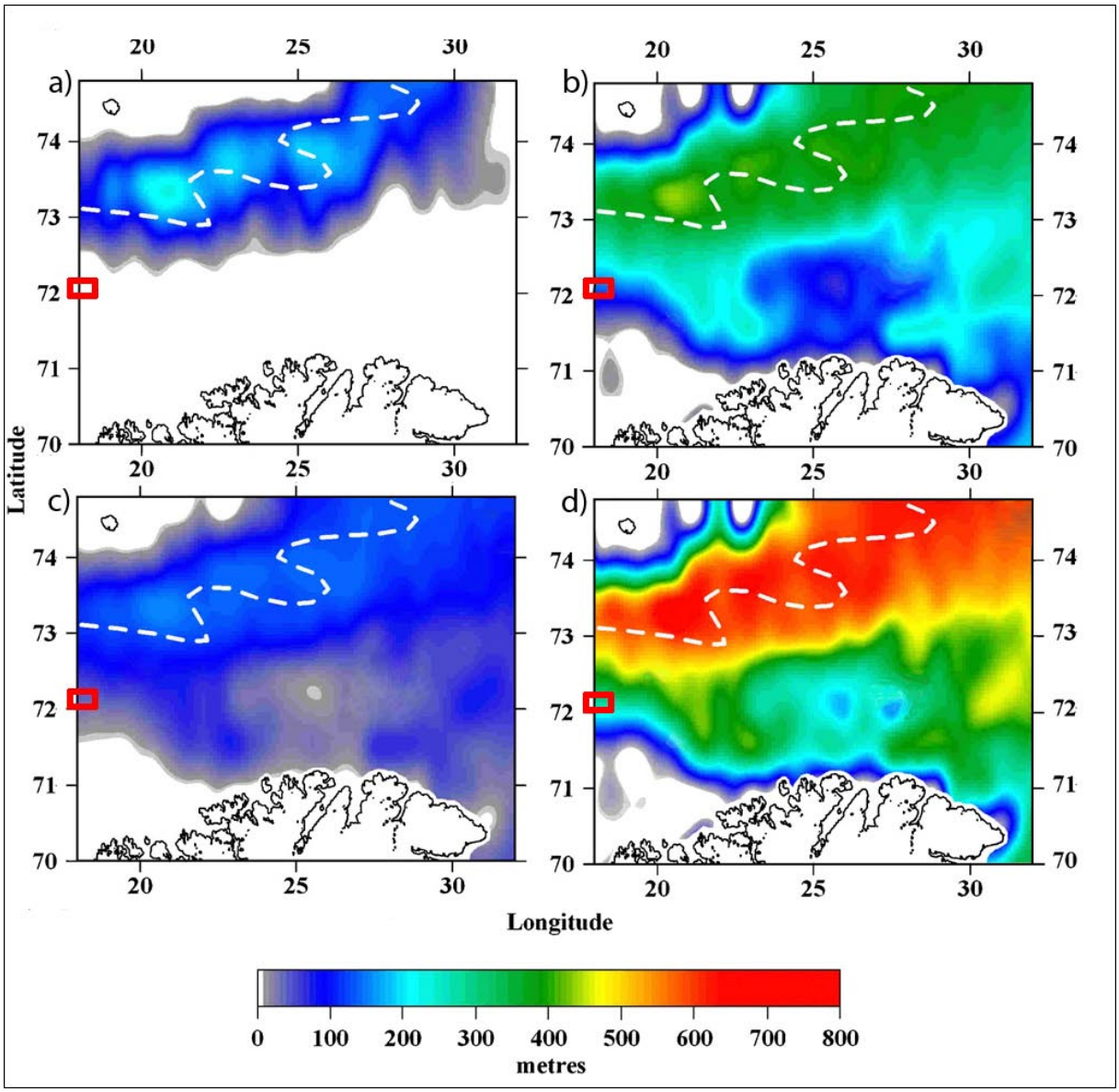

Figure 1.5. Gas hydrate stability field for different gas compositions and geothermal gradients assuming a sea water (salinity: 35 SU) system. Approximate location of EL0001 dataset is marked with a red rectangle. a) 100% methane and sea water at geothermal gradient of 31 C/km. b) 96% methane+3% ethane+1% propane and sea water at geothermal gradient of 31 C/km. c) 96% methane+3% ethane+1% propane and sea water at geothermal gradient of 69 C/km d) 96% methane+3% ethane+1% propane and sea water at geothermal gradient of 22.8 C/km. (After Chand et al., 2008).

1.2.5 Pockmarks

The development of 3D mapping in the 1960 allowed the discoveries of seabed morphological features such as pockmarks. They were first described in detail by King and McLean (1970). They described it as "A concave crater-like depression of the type that occurs in profusion on mud bottoms across the Scotian Shelf ". They had no proof as to why it was formed but interpreted it as being formed by upward-migrating gas bubbles lifting the sediments and putting them into suspension. Similar features were soon described in many other locations (e.g. Hovland, 1981; Hovland and Judd, 1988). Pockmarks are generally formed in soft, fine-

grained seabed sediments by the escape of fluid or gas into the water column (Hovland and Judd, 1988). Because pockmarks with rims caused by violent eruptions are very rare it is thought that the main process in creating pockmarks is fluids redistributing the fine-grained material in the sediments. The fine-grained material is then transported away with currents (Hovland et al., 2002). Normal pockmarks range in size from 10-700 m width and may be up to several tens of meters in depth (Hovland et al., 2002). The large pockmarks are often accompanied by several smaller size, sub-seismic resolution, pockmarks (Figure 1.6).

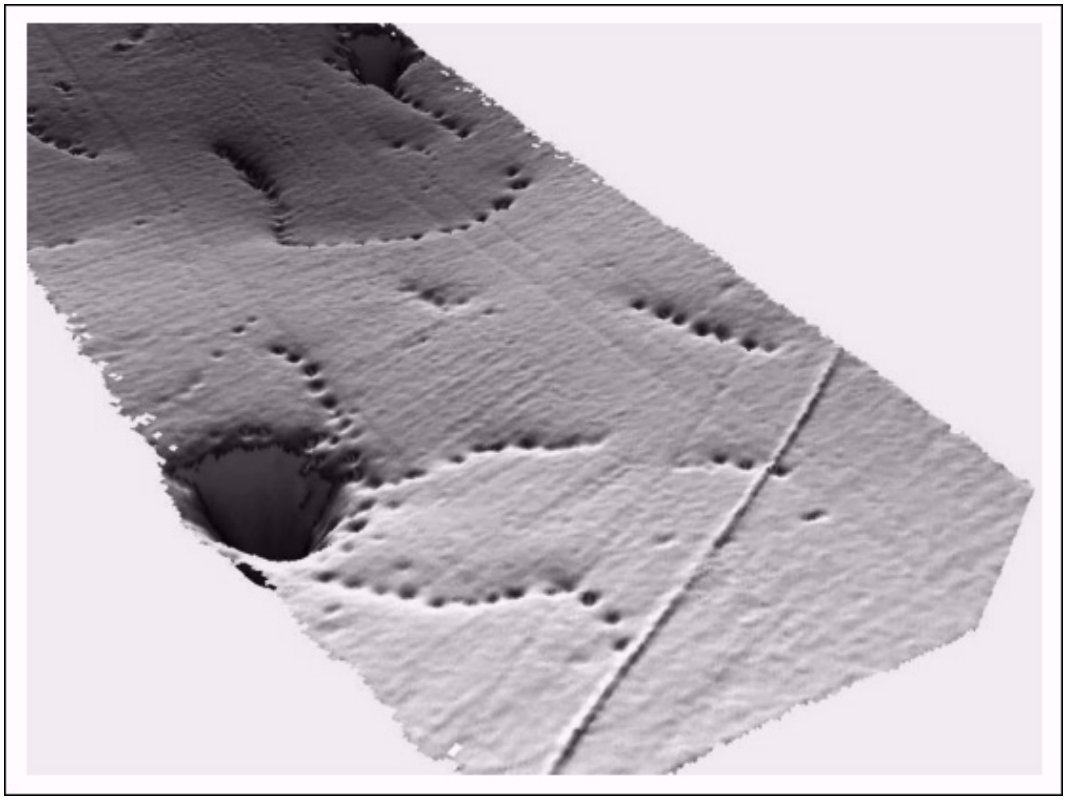

Figure 1.6 Two large pockmarks and strings of small pockmarks occurring adjacent to a 20 inch gas pipeline located on the seabed at 300m depth off Norway. Notice the strings of small pockmarks which won't be resolved in seismic data. From Hovland et al. (2002).

2 STUDY AREA

The Barents Sea, situated at the north-western corner of the Eurasian continental shelf, is a 200-400 m deep epicontinental sea bounded by passive continental margins in the west and north, Novaya Zemlya in the East and the Norwegian Coast in the south. Veslemøy High study area is located between 72° and 72°30´ N, and the 3D seismic survey EL0001 covers an area of 990 km^2 between 71° 59' 59.6" N and 72° 11' 49.4" N, and between 17° 20' 33.8" E and 18° 38' 59.5" E (Figure 2.1). Bordering Veslemøy High to the west lies Sørvestsnaget Basin, Tromsø Basin to the south and southwest, Bjørnøyrenna Fault Complex to the East and Bjørnøya Basin to the North (Figure 2.1). Tectonic structures show deep seated west-facing faults (Faleide et al., 1993). The depth from the seabed to base Tertiary in Veslemøy High is estimated to be 2-3 km and the depth to base Cretaceous is estimated to be 4-5 km. The crystalline basement is at 8 km depth in the western part and 13 km in the northeast (Mjelde et al., 2002). The geological background of the study area is mainly based on work by Fiedler et al., (1996), Norwegian Petroleum Directorate bulletin no 6, (Gabrielsen et al., 1990) and on Reset et al., (2003).

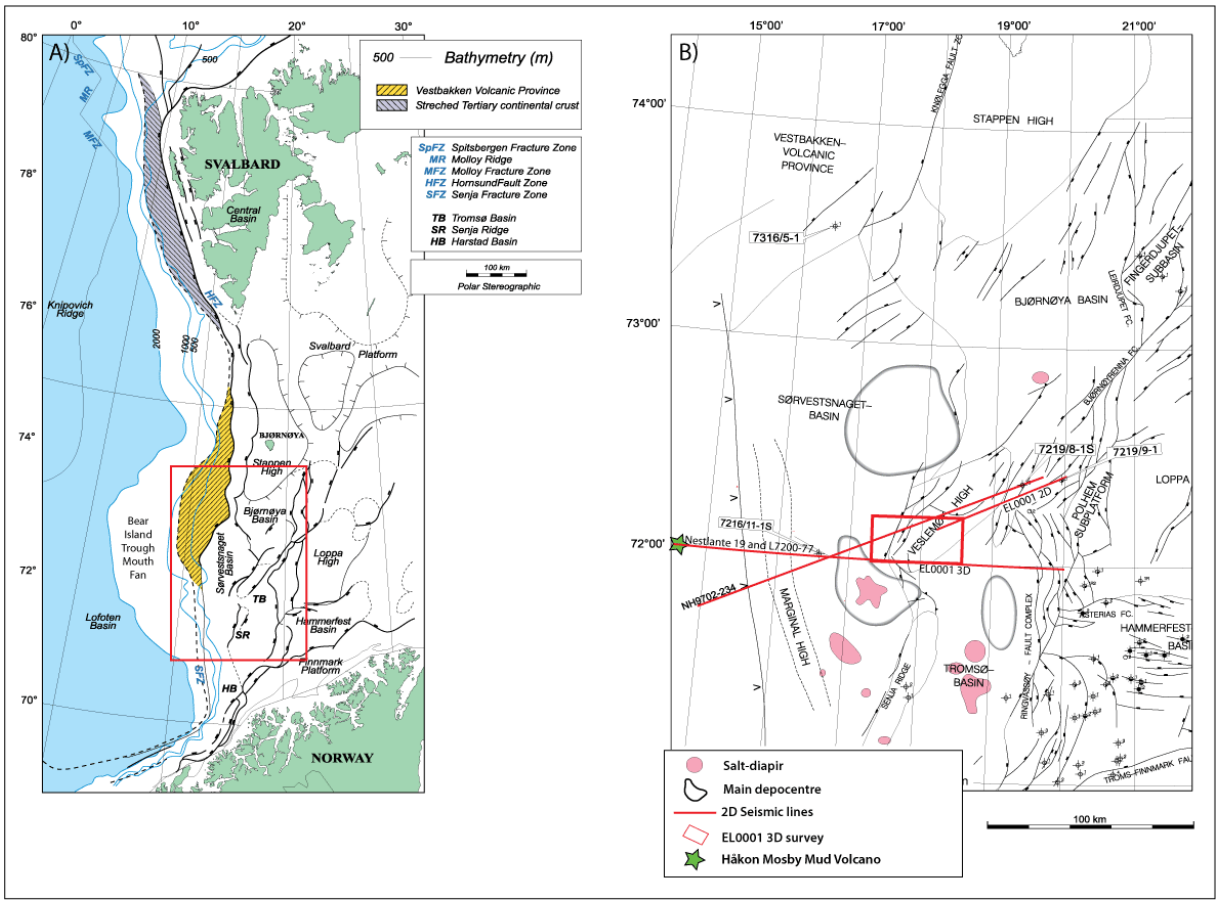

Figure 2.1. Map of study area shows a) general and b) detailed tectonic structures including working area (Ryseth et al., 2003).

2.1 Tectonic development of the southwestern Barents Sea

The southwestern Barents Sea lies in the northern part of the post-Caledonian North Atlantic rift system. The area has gone through several episodes of crustal extension and basin formation, from the Late Paleozoic until Early Tertiary.

2.1.1 Late Paleozoic to Early Mesozoic

A 300 km wide and 600 km long rift zone formed mainly during middle Carboniferous times (Gudlaugsson et al., 1998). It extended in a northeast direction and was a direct continuation of the northeast Atlantic rift between Greenland and Norway. The rift zone had a fan-shape and was composed of rift basins and intrabasinal highs with orientations ranging from north-easterly in the main rift zone to northerly at the present western continental margin.

From the beginning of Late Carboniferous the tectonic development was dominated by regional subsidence. This development was interrupted by a Permian to Early Triassic rifting phase and the formation of North trending structures (Gudlaugsson et al., 1998).

2.1.2 Early Mesozoic to Present

Since Middle Jurassic times, the tectonic development of the south-western Barents Sea comprises two main stages (Faleide et al., 1993), which is late Mesozoic rifting and basin formation, and early Tertiary opening of the Norwegian-Greenland sea and preceding rifting. This rifting was largely controlled by the already existing and deep-seated faults.

The Mesozoic rifting and basin formation shows two main phases (Faleide et al., 1993). The first is the Mid-Kimmerian tectonic phase (Middle to Late Jurassic) (Faleide et al., 1984), characterized by rifting and generation of normal faults, and thus sedimentary basins. The second is the Late Kimmerian tectonic phase (Late Jurassic to Early Cretaceous), which is characterized by development of deep-seated normal faults along zones of weakness in the Caledonian basement.

During Cretaceous and Early Tertiary, prior and during the opening of the Norwegian-Greenland Sea, the Western Barents Sea margin was reactivated by regional transform faulting and shearing. This led to subsidence and westward tilting of the shelf. Due to this a massive westward progradational sequence was developed, followed by an uplift and erosion during Neogene.

During Early Tertiary the entire south-western Barents Sea was situated within an overall transform setting (Faleide, 1991; Faleide et al., 1993). Uplift began in the Late Cretaceous and continued into the Early Paleocene.

Prior the Norwegian-Greenland Sea opening in the Early Eocene there was a tectonic regime of strike-slip. Regional dextral shear occurred along N-NW trending faults bounded by the Ringvassøy-Loppa Fault Complex in the east and the Senja Fracture Zone in the west (Faleide et al., 1988; Faleide, 1991; Breivik et al., 1998).

The opening of the Greenland Sea along the North Atlantic-Arctic rift became the dominant and large-scale influence on the tectonic development of the South-West Barents Sea for most of the Tertiary.

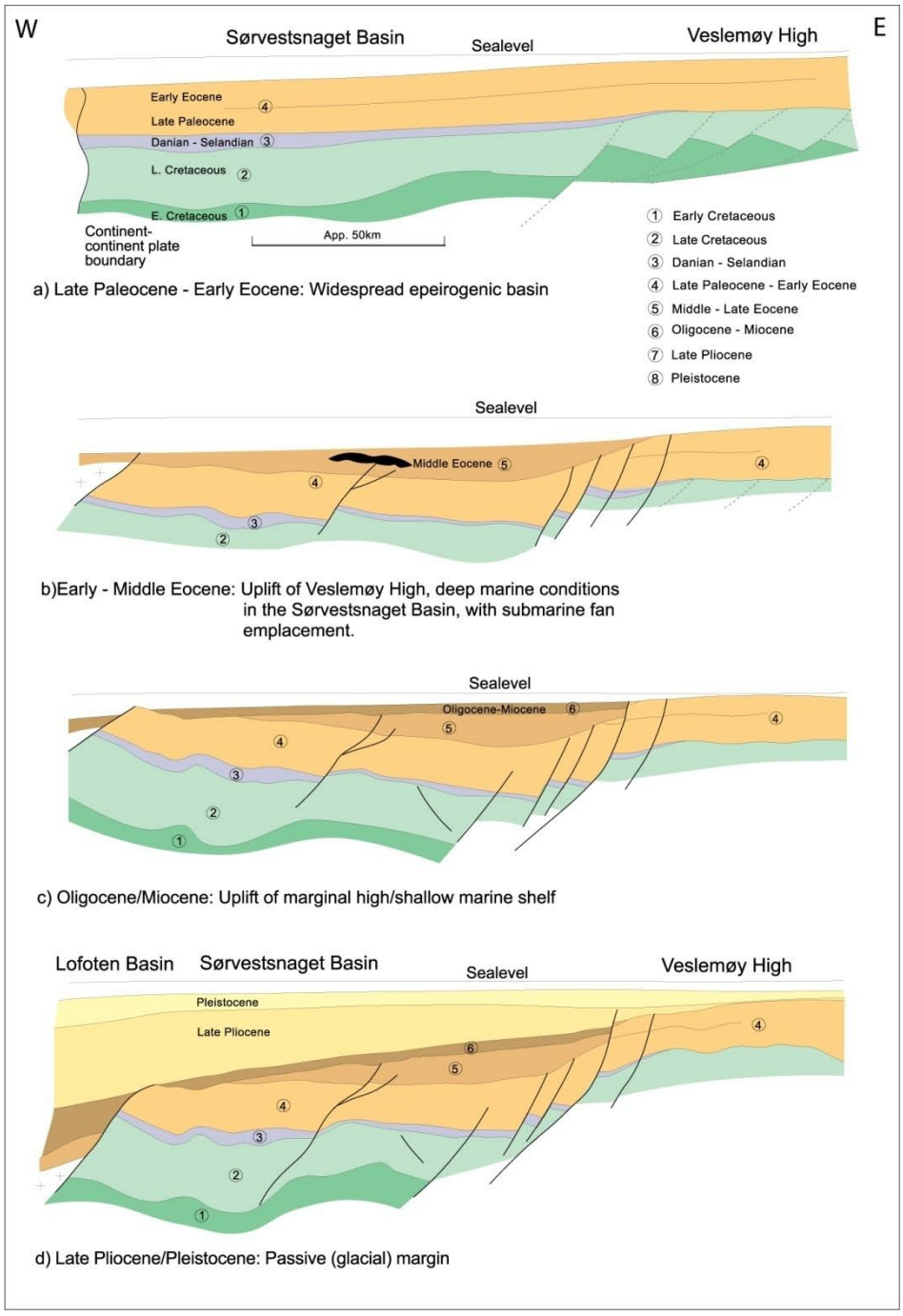

Figure 2.2. Tectonic-stratigraphic model of the Veslemøy High and bordering Sørvestsnaget Basin. From bottom to top, a-d, Late Paleocene to Pleistocene. (After Ryseth et al., 2003)

2.2 Seismic stratigraphy and lithostratigraphy

2.2.1 Seismic stratigraphy

The stratigraphy of the survey is divided into eight groups from Early Cretaceous to late Pleistocene (Figure 2.3) based on the stratigraphic division by Ryseth et al. (2003). Note that the units and reflectors of the Plio-Pleistocene sediments may have a different nomenclature depending on the literature used. In this master thesis the glacial sediments are divided into three mega sequences (GI-GIII) interpreted to represent three main phases of glaciations (Faleide et al., 1996). Seven reflectors of regional significance (R1-R7) were identified within the Plio-Pleistocene wedge, of which three are interpreted in this study. Reflector R1 corresponds to the upper regional unconformity (URU) on the shelf (Solheim and Kristoffersen, 1984). Reflector R5 corresponds to reflector 2 of Eidvin and Riis (1989). Reflector R7 corresponds to reflector 3 of Eidvin and Riis (1989). GIII corresponds to the Pleistocene succession and comprises all sediments above R1/URU. GII corresponds to the topmost part of the Plio-Pleistocene wedge and comprises all sediments between R1 and R5. GI corresponds to the lower part of the Plio-Pleistocene wedge and comprises all sediments between R5 and R7.

The Pleistocene succession has two main reflectors which are called in this thesis from bottom Intra Pleistocene 2 and Intra Pleistocene 1. Intra Pleistocene 1 corresponds to reflector bH (Ødegaard, 2005) or Intra GIIIc (Andreassen et al., 2007a), and Intra Pleistocene 2 to reflector bF (Ødegaard, 2005) or Intra GIIIa (Andreassen et al., 2007a).

The average estimated P-wave velocities of the Plio-Pleistocene sediments are for GIII: 1970 m/s; GII: 2160 m/s and GI: 2400m/s (Fiedler and Faleide, 1996).

The dataset EL0001 is located in the middle of the Veslemøy High, with strata dipping mainly towards the East (Ringvassøy-Loppa Fault Complex, Bjørnøyrenna Fault Complex and Tromsø Basin) and West (Sørvestsnaget Basin) (Figure 2.4).

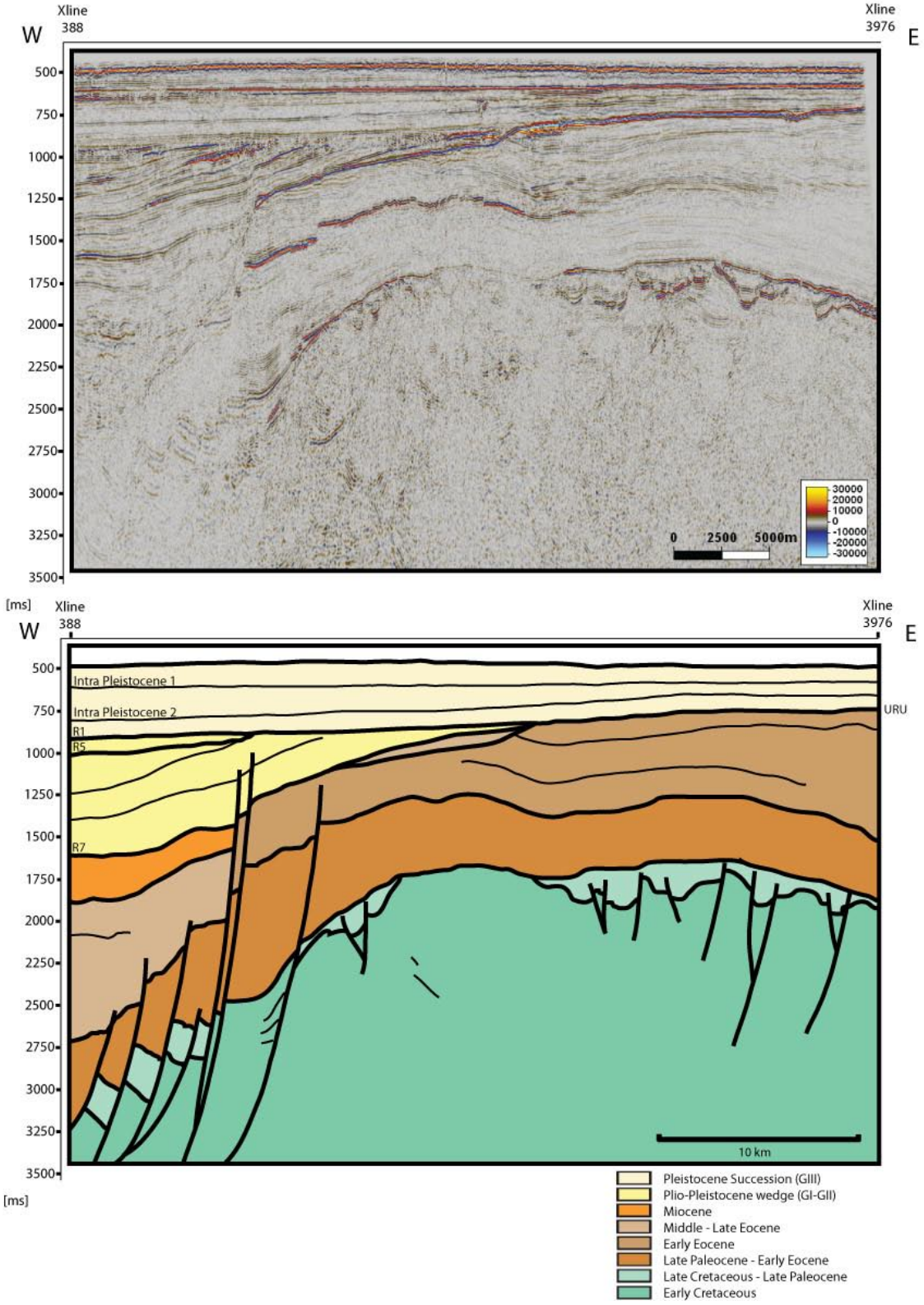

Figure 2.3. Interpretation of the stratigraphy of inline 1340 in dataset EL0001. Based on the stratigraphy established by Fiedler and Faleide (Fiedler and Faleide, 1996), Norwegian Petroleum Directorate bulletin no 6 (Gabrielsen et al., 1990) and on Ryseth et al. (2003).

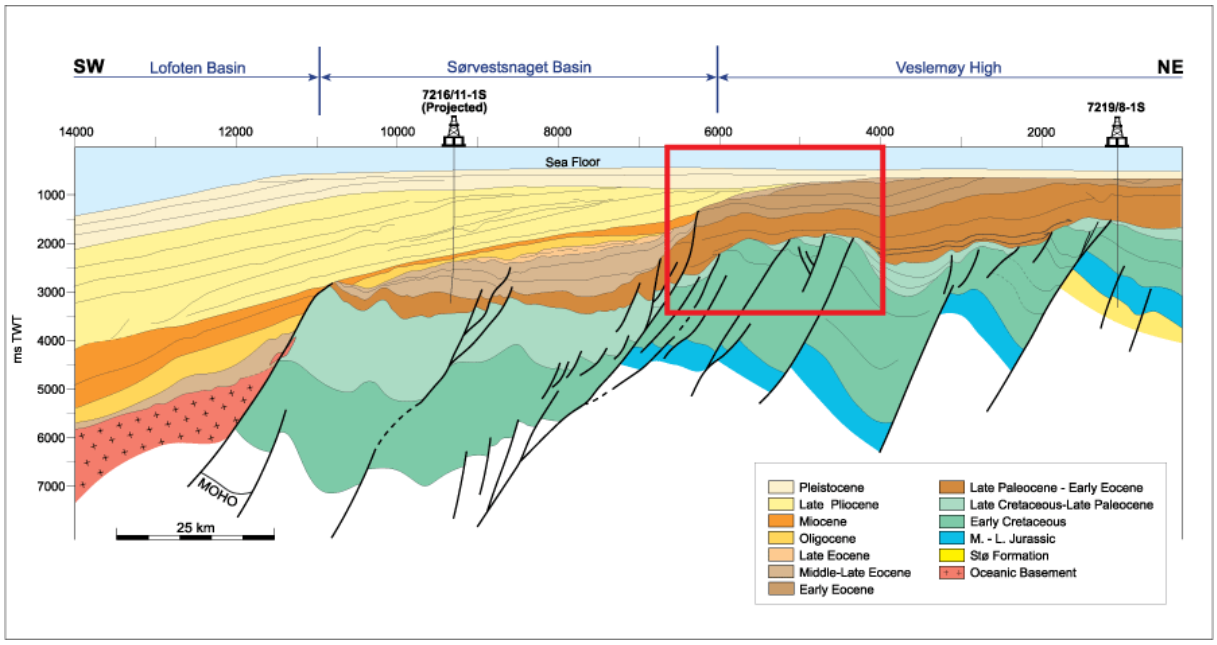

Figure 2.4. Stratigraphy of 2D line NH9702-234, approximate location of dataset EL0001 marked with a red rectangle. Locations of wells 7216/11-1S and 7219/8-1S are indicated. From Ryseth et al. (2003)

2.2.2 Lithostratigraphy

The lithostratigraphy is based on Dalland et al. (1988), Johansen et al. (1993) and Ryseth et al. (2003). As the dataset used in this thesis is cropped at 3500 ms TWT it does not contain sediments older then Cretaceous and these will therefore not be discussed in this section.

Cretaceous

The Lower Cretaceous sequence is 1-3 km thick and extends across the entire Veslemøy High, Sørvestsnaget, Tromsø, Harstad and Bjørnøya Basins (Dalland, 1988).

The Barremian to Aptian volcanic events in the northern Barents Sea are documented as volcanic tuffs as far south as in the Hammerfest basin (Linjordet and Olsen, 1992). Uplift of the Lomonosov Ridge and prograding shallow shelf with terrestrial systems developed from the north. The basins in the south-western Barents Sea were in a distal position to these prograding delta systems and dominated by fine grained marine sediments. These are the lithologies of the Knurr and Kolje Formations (Dalland, 1988; Johansen et al., 1993). The Kolmule Formation (Barremian to Albian) contains shales and claystones with stringers of siltstones, sandstones and limestones (Dalland, 1988). In some distal locations such as the western Barents Sea basins the environment (Early Barremian) was locally favorable for the development of organic-rich shales. Tectonic uplift caused breaks in the deposition and development of condensed sequences in the southwestern Barents Sea (Brekke and Riis,

1987; Dalland, 1988) due to compressional deformation from the Maastrichtian and to the Paleocene (Faleide et al., 1993).

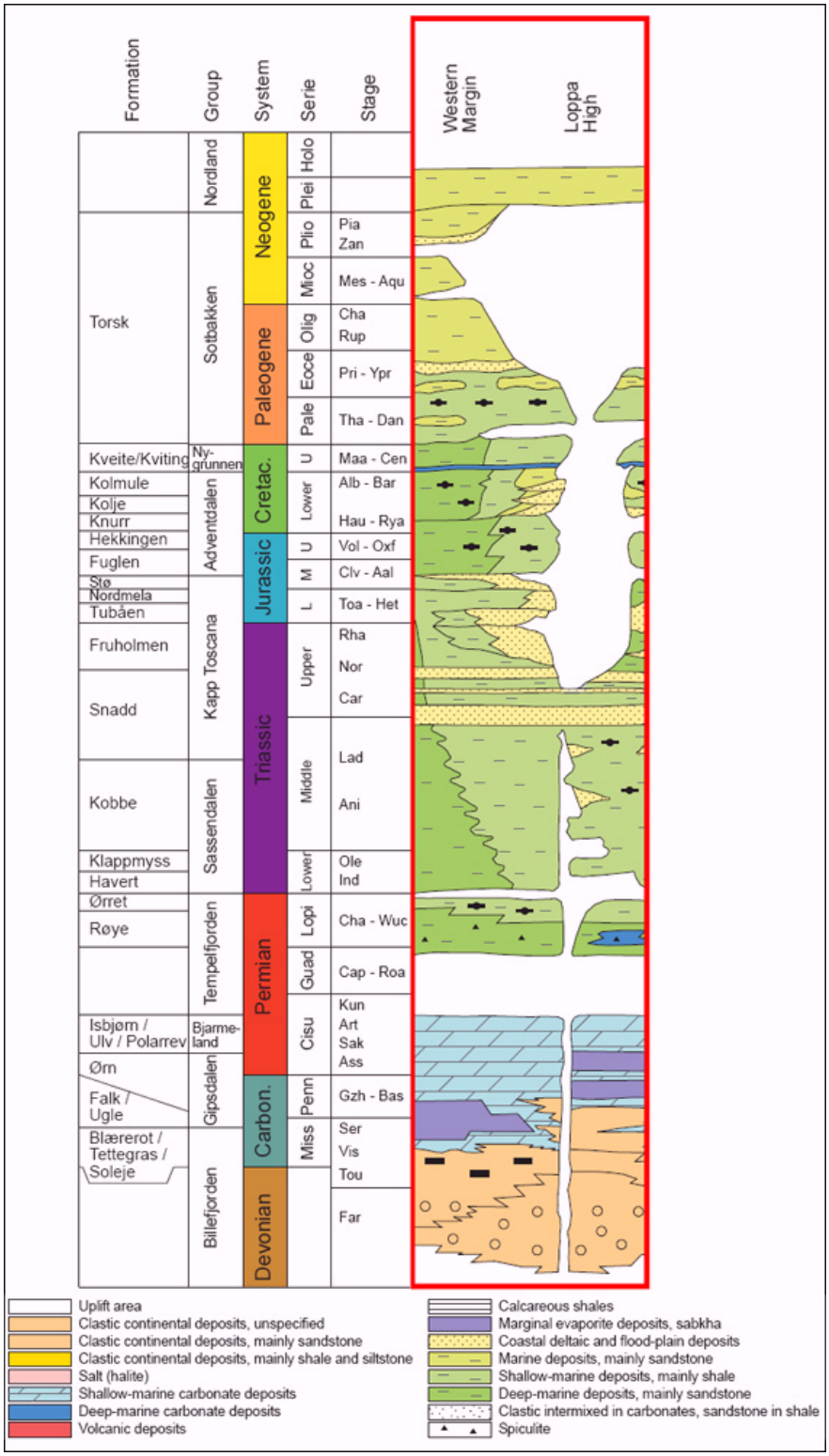

Figure 2.6. Southwestern Barents Sea: Lithostratigraphic scheme modified from Elvebakk (2008).

Tertiary

The uplift was followed by a transgression which resulted in the deposition of fine grained marine sediments that covered large parts of the western Barents Sea during the Late Paleocene and Eocene. During the Early and Mid Eocene rifting and volcanism was linked to the opening of the Norwegian Greenland Sea (Faleide, 1991; Faleide et al., 1993; Breivik et al., 1998). During the Eocene to Oligocene about 100 m of Paleogene sediments were eroded from the outer margins of the Barents Sea (Breivik et al., 1998). In the Sørvestsnaget Basin the Paleocene to Early Eocene sediments developed into dark gray laminated shales with thin dolomites, siltstones and sandstones. These formations are characteristic of deep oxygen starved basins intercalated with turbidites and gravity flows (Ryseth et al., 2003).

Concurrent with the opening of the Norwegian-Greenland Sea and associated crustal breakup the Veslemøy High was uplifted during Early to Middle Eocene. Subsequently sandstones were deposited west of Veslemøy High, in Sørvestsnaget Basin, by sediment gravity flows (Ryseth et al., 2003). East of Veslemøy High, in the Tromsø Basin, progradation of sediment deposits was at first westwards in Early Eocene, with Loppa High as a suggested source area. During Early to Mid Eocene, progradation also had a southward and an eastward component from the Veslemøy High (Knutsen et al., 1992). This Eastward and southward propagation indicates that Veslemøy High and areas north of Tromsø Basin were uplifted and eroded. During this time the subsidence of the Tromsø Basin continued and probably accelerated (Knutsen et al., 1992). During the Middle to Late Eocene there was an extensive development of salt diapirs in areas surrounding Veslemøy High.

The Upper Eocene to Miocene succession in the Sørvestsnaget Basin is dominated by highly condensated shales and mudrocks. An interval at Oligocene-Miocene is however dominated by sediments deposited in shallow marine environments.

Pleistocene

The south-western Barents Sea margin has been affected by glaciations reaching the shelf edge in many episodes during the last 1.5 Ma (Faleide et al., 1996; Andreassen et al., 2004; 2007b). The eroding ice sheets have produced a massive prograding outer shelf sequence. The Cenozoic exhumation reached an estimated erosion of up to 1000 meters (Cavanagh Andrew et al., 2006). Differences in ice thickness caused pressure oscillations in the deeper formations which may have provided a mechanism for episodic discharge of gas from petroleum systems and cycles of gas hydrate sequestration and release. The Western Margin has only

experienced limited uplift compared to the rest of the Barents Sea. The literature varies on this subject but StatoilHydro operates with numbers of 0-100 m uplift (StatoilHydro unpublished) after the glacials so exhumation will only play a minor part in fluid escape processes in Veslemøy High.

The Pliocene wedge which stretches from Veslemøy High and out into Sørvestsnaget Basin is at well location 7216/11-1S dominated by shales and mudrocks but with intervals of high porosity sandstones. Sandstone stringers and intervals are caused by turbidity and gravity flows. At the source of the flows the wedge is likely to be more sand prone, thus a higher frequency of sand intervals in the Pliocene wedge may occur in Veslemøy High compared to well location 7216/11-1S.

The transition from erosion to accumulation is marked by the Upper Regional Unconformity (URU). The URU is a result of the eroding ice-sheet and it truncates the underlying Tertiary stratigraphy resulting in an angular unconformity.

2.3 Source rocks

On a regional scale, known possible source rocks in SW Barents Sea are the Late Jurassic Hekkingen Formation, which is thick enough to generate significant quantities of hydrocarbons and extends regionally in the Barents Sea, Early Jurassic Nordmela and Tubåen Formations and Early and Mid Triassic Formations, Snadd, Kobbe, Klappmyss and Havert formations (Doré, 1995). From a more localized point of view Veslemøy High is the stratigraphic high to which hydrocarbons may migrate in from surrounding basins. Migration may take place laterally in carrier beds or directly from below. Likely sources of fluids will be addressed in the discussion.

3 DATA AND METHODS

The database consists of the 905 km^2 3D seismic survey EL0001, a 195 km long 2D seismic line (NH9702-234) that ties the 2 wells 7216/11-1S and 7219/8-1S to EL0001 (See Figure 2.1), and the 2D line (EL0001-0003) that ties the well 7219/9-1 to the 3D survey. In addition, the 2D surveys NPD-BJSY-84, NPD-TR-82-OD102, NPD-TR-82-OD106, NPD-TR-82-OD109, IKUB84 and NH8403 were used for quality control on well correlations and for mapping the Early Eocene high amplitude anomaly east of the EL0001 3D survey.

3.1 Well data

Wells have been used in order to understand the lithology and depositional environment in the area thus understanding potential reservoirs and migration paths. However, no wells are located within the 3D survey EL0001. Three wells are located within the vicinity of the 3D survey and are tied to the 3D survey using the 2D lines. The wells used are 7216/11-1S (25.5 km west of EL0001), 7219/8-1S (32.5 km NE of EL0001) and 7219/9-1 (49.5 km NE of EL0001) (See locations in Figure 2.1).

Thermal gradients are calculated from bottom hole temperatures and maximum true vertical depths of the three wells. They are at: 7219/8-1S: 37,5°C/1000 m; 7219/9-1: 33,8°C/1000 m and at 7216/11-1S: 30,5°C/1000 m. The average geothermal gradient observed in the Barents Sea region is around 30°C/km (Laberg et al., 1998).

3.1.1 Acoustic velocities from wells

Table 3.1. Table displaying approximate acoustic P-wave velocities at formation tops calculated from sonic logs. Depths in true vertical depth (TVD).

Formation tops	Acoustic velocities from wells					
	Well 7216/11-1S		Well 7219/8-1S		Well 7219/9-1	
	Depth [m TVD]	Velocity [m/s]	Depth [m TVD]	Velocity [m/s]	Depth [m TVD]	Velocity [m/s]
Top Nordland	385.0	-	393.0	-	379.0	-
Top Torsk	2370	3020	554.0	2030	483.0	1900
Top Kolmule	-	-	1545.0	2380	1467.5	2650
Top Kolje	-	-	2080.0	3020	-	-
Top Knurr	-	-	2493.5	3500	1835.5	3010

3.1.2 Well 7216/11-1S

The well is located in Sørvestsnaget Basin, 25.5 km west of EL0001 (Figure 2.1). It was drilled in year 2000 by Norsk Hydro to test three target horizons in the Paleogene Lower Torsk Formation. The well was spudded in water depths of 361 mMSL and drilled in a deviated well path to 4215 mMSL (3709 mMSL TVD). The well was dry and terminated in sediments of Danian age (Figure 3.1). However it proved a total of 30 m gross reservoir sequence of excellent quality turbidite sandstone at the Late Paleocene level.

No hydrocarbon shows were observed while drilling the well, only a thin gas bearing sand was observed from density/neutron log at 1988 mMSL.

The completely fine-grained nature of the Paleocene -Lower Eocene succession is indicative of deposition in a generally low-energy marine environment. Microfaunal evidence is indicative of a poorly oxygenated deep marine shelf or bathyal environment (Ryseth et al., 2003)

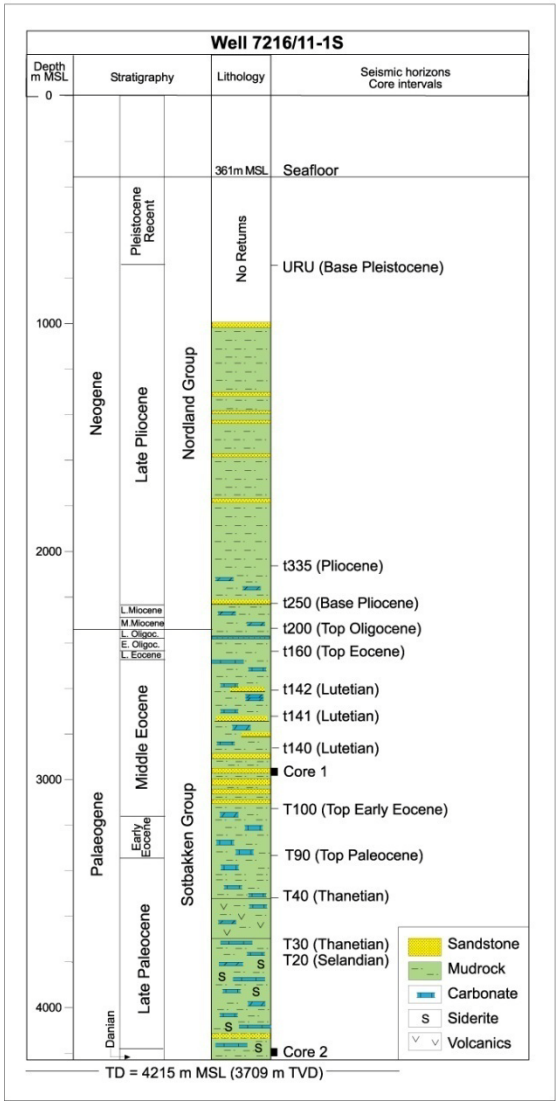

Figure 3.1 Stratigraphic and lithological summary of well 7216/11-1S, Sørvestsnaget Basin. Depths are measured depths (MD) not true vertical depth (TVD). The well terminates in strata of Early Paleocene (Danian) age. From Ryseth et al. (2003).
A thin injected sand layer cuts through the primary lamination at 2970,6 m. Biostratigraphic data indicates Middle Eocene had a deep, oxygen-depleted marine depositional environment and data indicates the sandstone is gravity deposited in a submarine fan/channel environment (Ryseth et al., 2003). Large scale soft sediment deformation including diapirism is also inferred following the deposition of the sandy submarine fan on soft water-saturated clayey sediments.
The Middle - Upper Miocene succession consists of silty mudrocks, scattered fine-grained sandstones and dolomite-cemented stringers. The Oligocene - Miocene succession was probably deposited in a shallow marine environment. The Plio-Pleistocene wedge consists of grey clays and claystones with minor beds of fine- to very coarse sand, and a glacio-marine depositional environment can be inferred from micropaleontological data (Ryseth et al., 2003)

3.1.3 Well 7219/8-1S

The well drilled in 1992 by Saga Petroleum is located in the Bjørnøya Sør area east of the Veslemøy High (Figure 2.1). The primary purpose of the well was to test the middle Jurassic Stø Formation. And the secondary objective was to test possible sandstone in Late Jurassic Hekkingen Formation. The third aim was to test possible sandstone at Early Cretaceous level. The well was spudded in water depths of 345 mMSL and drilled in a deviated well path to 4587 mMSL (4380 mMSL TVD). The well was drilled 91 m into the Early-Middle Jurassic Stø Formation.

Down to Base Cretaceous at 3319 mMSL TVD, the well penetrated mainly claystones. Traces of hydrocarbon shows were seen in some silty parts of the Cretaceous from 2325 to 2346 mMSL TVD and from 2508 to 2561 mMSL TVD.

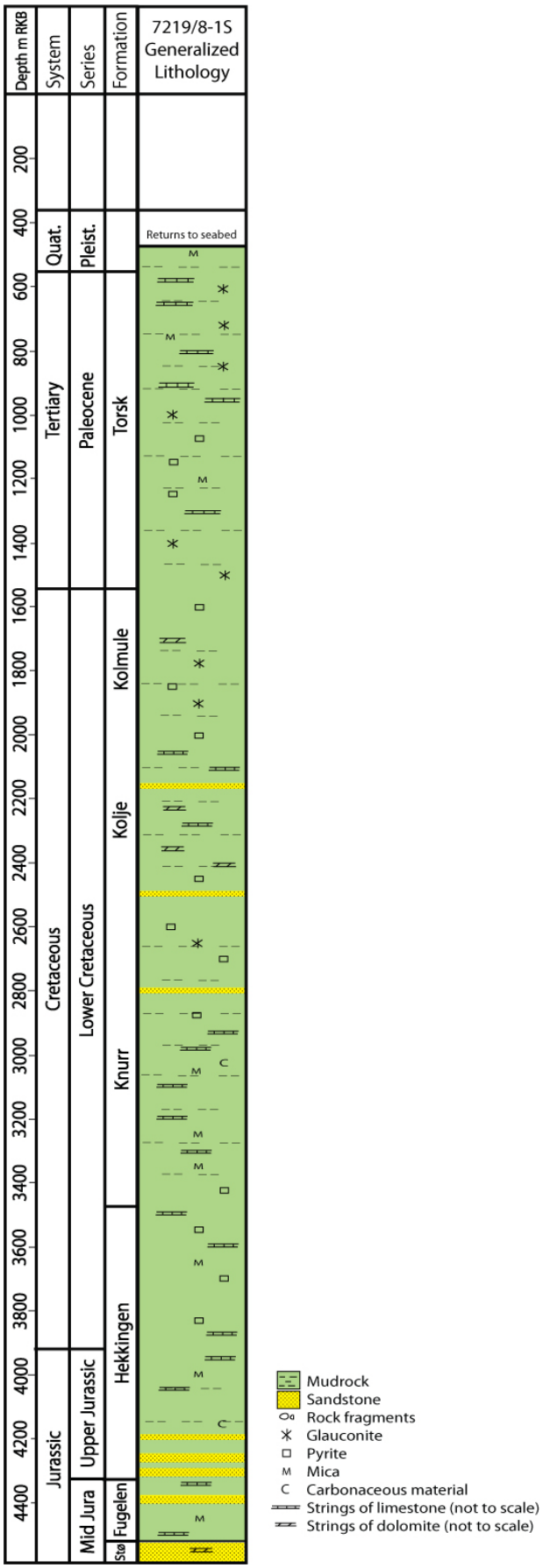

Figure 3.2 Generalized lithology of well 7219/8-1S. Modified from completion log (NPD, 2009). Organic geochemical screening analyses show consistently high TOC over the Early Cretaceous to Late Jurassic interval, 2815 to 3740 MD RKB (typically 2-3.8%). The maturity is quite advanced (%Ro typically 0.9-1.5) and it increases with depth as the hydrogen index decreases from about 120 to about 50 mg/g HC. The source potential was probably reduced due to thermal maturation. A 200 m (112 m gas + 88 m oil) residual paleo-hydrocarbon column was identified in the well (Knutsen et al., 2000).

3.1.4 Well 7219/9-1

The well is located in the Bjørnøya Sør area between the Veslemøy High and the Polheim Sub-platform. The Cenozoic strata contain mainly mudrock with a few stringers of sand and silt.

Top reservoir Stø formation was encountered from 1950.5 m to 2062 m with 99 m net sand of 17.8% average porosity. The reservoirs in Nordmela (2062 m to 2205.5 m) and Tubåen (2205.5 to 2305 m) formations were water-bearing with possible residual oil.

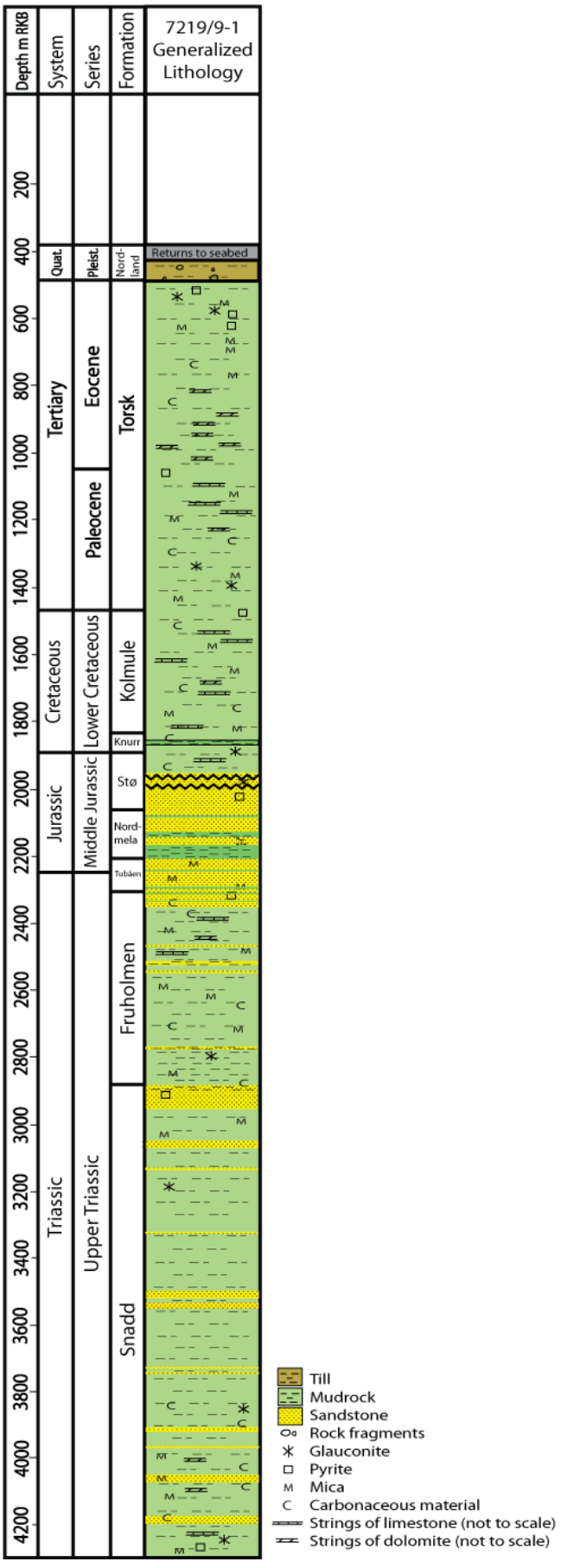

Figure 3.3. Schematic lithology and age of the Cenozoic strata in well 7219/9-1. Modified from Knutsen et al. (1992). Nordmela formation was penetrated from 2062 m to 2205.5 m with 59.5 m net sand with 16.5% average porosity. Tubåen Formation was penetrated from 2205.5 to 2305 m and it had 64.5 m net sand with 17.3% porosity.

3.2 3D seismic survey EL0001

The 3D survey EL0001 was collected for TotalFinaElf during 2001. It was processed by CGG Norway at their Oslo processing centre.

Table 3.2. Information about the survey; EL0001 3D.

Information about the survey; EL0001 3D	
Geodetic datum	ED50
Spheroid	Internat.
Projection	UTM 34N
First sample	4 ms
Last sample	8000 ms
Sample interval	4 ms
Distance between inlines	12.5 m
Distance between crosslines	12.5 m
Bin size	12.5x12.5 m
Inline direction	92.854 Degrees
Crossline direction	2.854 Degrees
Polarity	Minimum phase (as recorded)

3.2.1 Artefacts

A range of artefacts has to be considered during seismic interpretation (Bulat, 2005). Identification of artefacts is important to distinguish them from actual data. The following documents obvious artefacts that are present in the 3D seismic survey EL0001.

3.2.1.1 Acquisition footprint

The acquisition footprint generates artefacts along the direction of inlines in the data. On the interpreted seafloor reflection in 3D seismic survey EL0001 (Figure 3.4) it resembles elongated ridges (aligned approximately 93/273°) running parallel to the inlines (aligned 92.854°). These artefacts may arise from a faulty acquisition geometry of the streamers and guns (Marfurt et al., 1998). Other possible explanations are towing depth differences of the streamers or guns that cause differences in two-way travel times. Though processing is designed to eliminate noise and correct for systematic errors like tides some errors will always pass uncorrected through the processing. These artefacts are very subtle and do not significantly disturb the data but may lead to misinterpretations if one is not aware of them.

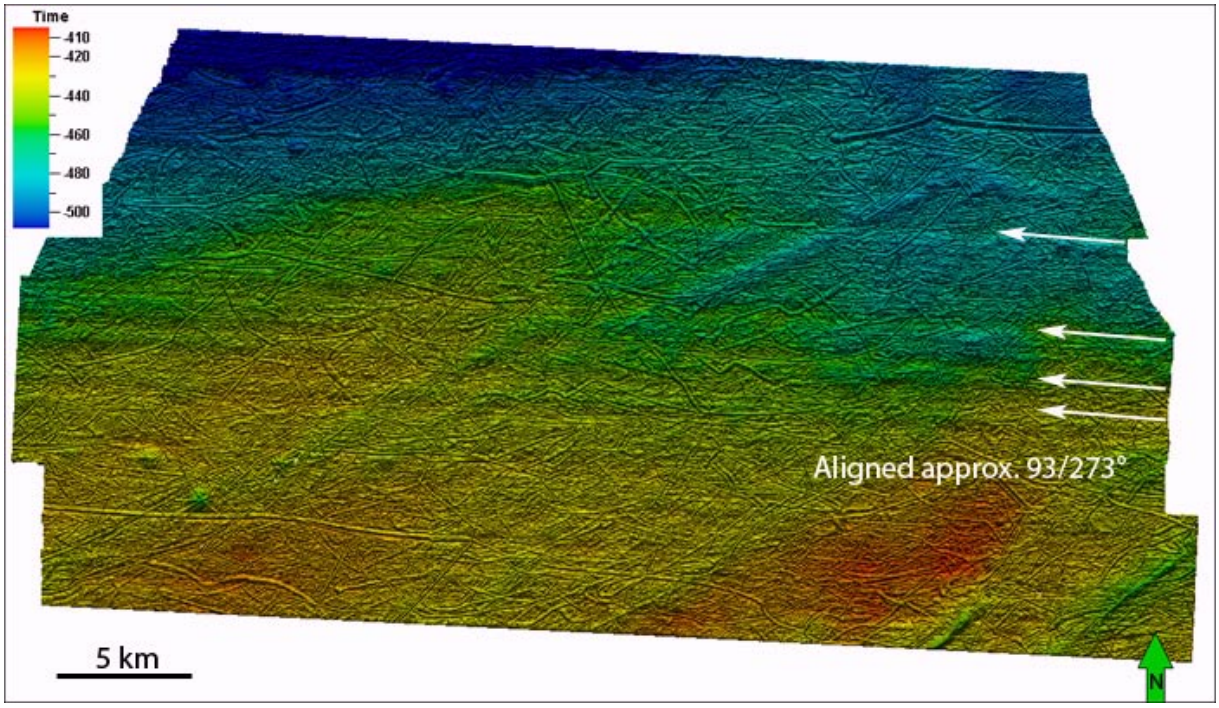

Figure 3.4. E-W trending elongate ridge-features indicated by white arrows are a result of the acquisition footprint. The seafloor horizon is enlightened by a light source a few degrees above the horizon from south.

3.2.1.2 Error with static corrections

Due to an error with static corrections certain traces aligned in four SW-NE trending lines are moved down approximately 30-100 ms. These artefacts appear in the seismic data cube and therefore in the figures of the thesis. The traces in question are easy to recognize as they are aligned in lines SW-NE (48/228°). The artefacts appearance on a seismic intersection will be completely vertical and only affects the traces in question. These artefacts probably appeared due to problems in the seismic acquisition or processing and haven't been removed. Any removal had to be done manually on each inline, and would therefore be very time consuming.

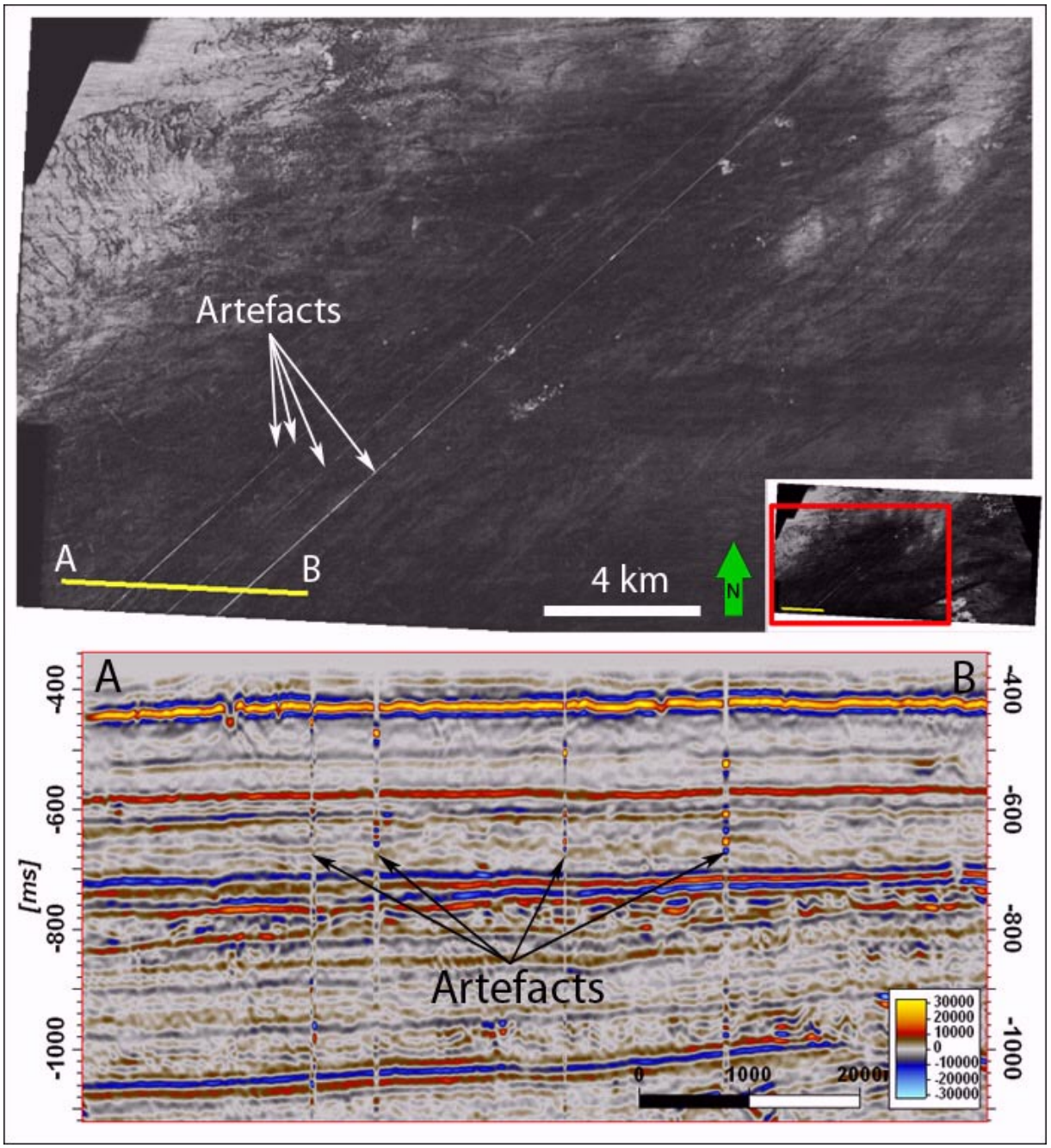

Figure 3.5. Four SW-NE aligned lines with static correction errors are present in the dataset displayed on a RMS amplitude timeslice and a seismic section.

3.2.2 Vertical and horizontal resolution

In order to calculate vertical resolution the dominant wavelength has to be considered, which is wave velocity (v) divided by dominant frequency (f):

Wavelength (λ): $\lambda = \frac{v}{f}$ (Hz) (Equation 3.1)

Seismic wave velocities for a given lithology generally increase with depth and the dominant frequency decreases with depth due to the attenuation of higher frequencies (Brown, 1999). Therefore seismic resolution is generally deteriorating with increased depth.

An average velocity of 2500 m/s is assumed for these calculations (compare with Table 3.1). The Pliocene sediments may be less consolidated and have lower velocities and therefore higher resolution. The dominant frequency of the top 2000 ms TWT (Quaternary and Tertiary strata) in EL0001 is estimated in Landmarks seismic processing program Promax to be 26 Hz and the effective bandwidth to 62 Hz (3-65 Hz).

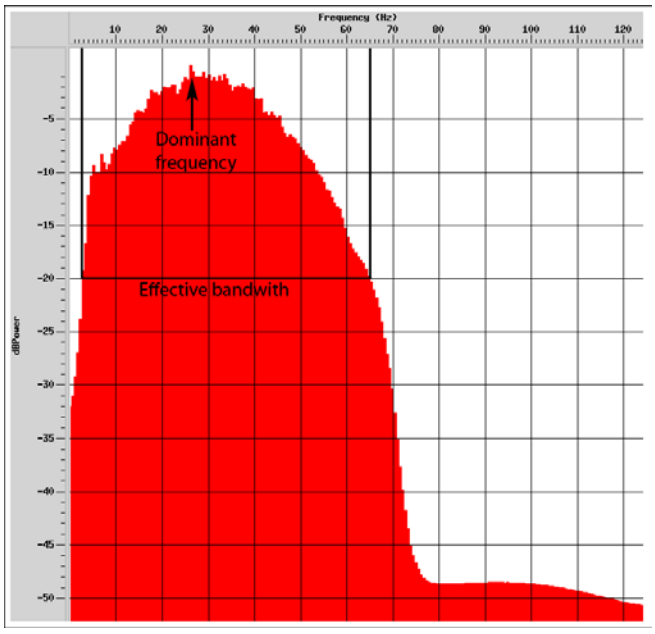

Figure 3.6. Frequency spectrum of top 2000 ms TWT of a representative inline (818) with dominant frequency and effective bandwidth indicated.

The threshold distance for distinguishing between two reflectors is generally ¼ λ. This is known as the ¼ λ rule (Yilmaz, 1987). However thin gas-filled sand stringers with a thickness down to 1/20-1/30 λ can be detected if they constitute a strong enough acoustic impedance contrast. The vertical resolution according to the ¼ λ rule and assumed velocities (2500m/s) and frequencies (26 Hz) will be:

Vertical resolution: $$\frac{1v}{4f} = \frac{2500m/s}{4*26Hz} = 24m$$ (Equation 3.2)

The lateral resolution refers to the minimum horizontal distance between two reflecting points needed to have in order to be recognized as two separate points. The pre-migration lateral resolution is given by the size of the Fresnel zone. The Fresnel zone is the area which the wave front reaches within ¼ λ. This is dependent upon frequency, velocity and also the distance down to the reflector. It is described below using TWT (t).

Fresnel zone radius: $$r_F = \frac{v}{2}\sqrt{\frac{t}{f}}$$ (Equation 3.3)

$$r_F = \frac{2500m/s}{2}\sqrt{\frac{1.5s}{26Hz}} = 360.3m$$

3D migration will allow reducing the Fresnel zone to a diameter of ¼ λ. Therefore the horizontal resolution equals the vertical resolution, but poor data quality may reduce the horizontal resolution (to ⅓ or ½ λ).

3.3 Interpretation and visualization tools

Schlumbergers program Petrel 2008.1 was used as the primary interpretation and visualization tool using a Windows 64 bit workstation.

3.3.1 Interpretation of 3D seismic reflectors

Horizon interpreting in Petrel was performed using four basic methods: (1) manual interpretation, where the interpretation is interpolated linearly between picked points; (2) guided autotracking where the program will find the best route along a reflection between two picked points; (3) seeded 2D autotracking, where points will be tracked along a reflection until it comes to a discontinuity and does not fulfill the constraints specified in the autotracking parameters; (4) seeded 3D autotracking, where points will be tracked outwards from a picked point in all directions to get a 3D view of a distinct reflection. In order to get a better quality control a combination of 2D seeded autotracking, guided autotracking and manual interpretation was utilized. A method called Paintbrush tracking was also utilized in a 2D top view window. It is similar to Seeded 3D autotracking but confined to a square with a predefined size.

3.3.2 Seismic attributes

Seismic attributes were calculated for volumes around or in between surfaces along faults and entire data volumes. Noteworthy, many attributes produce very similar results and their redundancy was therefore discussed (Barnes, 2007). Therefore, only a limited selection of available attributes has been used in this thesis for the interpretation of the 3D survey EL0001.

RMS Amplitude is the square root of the sum of the squared amplitudes, divided by the number of samples. RMS maps geologic features which are isolated from background features by amplitude response. It is an excellent indicator for accumulations of hydrocarbon. Mathematically, it is given as:

$$\sqrt{\frac{\sum_i^n amp^2}{k}} \qquad \text{(Equation 3.4)}$$

Envelope, or reflection strength, is defined as the total energy of the seismic trace, or the modulus of the seismic trace;

$$\sqrt{f^2(t) + g^2(t)} \qquad \text{(Equation 3.5)}$$

In which f(t) is the original seismic trace, the real part and g(t) is the imaginary part. It can be used to detect bright spots, major lithological changes and sequence boundaries.

Variance is Schlumbergers patented method of isolating discontinuities in the horizontal continuity of amplitudes. It is most often used to isolate faults in the data but may also be useful for bringing out stratigraphic features. Other methods of isolating faults and producing similar results are patented by other companies and are known as Coherency (Bahorich and Farmer, 1995) or Semblance/Discontinuity (Marfurt, 1998, 1999). The normalized variance algorithm is computed as:

$$\sigma_t^2 = \frac{\sum_{j=t-L/2}^{j=t+L/2} \left(w_{j-t} \sum_{i=1}^{l} (x_{ij} \bar{x}_j)^2 \right)}{\sum_{j=t-L/2}^{j=t+L/2} \left(w_{j-t} \sum_{i=1}^{l} (x_{ij})^2 \right)} \qquad \text{(Equation 3.6)}$$

where x_{ij} is the sample value at horizontal position, i, and vertical sample, j, and w_{j-t} is the vertical smoothing term over a window of length, L.

Dominant frequency is defined as the square root of the sum of the squares of the instantaneous frequency and instantaneous bandwidth. Mathematically, it is given as:

$$\omega_{RMS} = \sqrt{\omega_B^2 + \omega_c^2} \qquad \text{(Equation 3.7)}$$

It can be used to identify low frequency shadows, for example in pipes and chimneys.

Cosine of instantaneous phase, or normalized amplitude, is the cosine of the instantaneous phase angle $\varphi(t) = \tan^{-1}(g(t)/f(t))$.

$$Cos(\tan^{-1}(g(t)/f(t))) \qquad \text{(Equation 3.8)}$$

This operation scales the data from 1 to -1 and it can improve reflector continuity and enhance faults and stratigraphic boundaries. Cosine of phase is often used to help guide interpretation in poorly resolved areas.

Ant tracking is a patented attribute from Schlumberger which helps to identify faults, fractures and other linear features (Pedersen et al., 2002). A typical workflow for generating an ant track attribute cube will contain 4 steps. First the seismic volume needs to be smoothed in order to remove spatial noise and higher frequency events. Second, structural smoothing with dip guide and edge enhancement is used to retain significant discontinuities. Third, an edge detection method such as variance or chaos attribute will be applied. A second pass of smoothing is then performed using the variance or chaos cube as input. This smoothing is performed without dip guide and edge enhancement to perform a 3D Gaussian smoothing. It improves spatial continuity and reduces spatial noise. The fourth step is to produce the ant tracking cube. It is recommended to perform parameter testing on a small cropped cube containing a typical feature. Ant tracking can be run on the whole cube when the parameters which best display geological target features. Ant tracking was used to recognize and map fault structures in the survey.

3.3.3 Visualization of data

Data can be visualized in different ways. Surfaces can be displayed in 2D and 3D using a variety of color-scales and lighting directions, highlighting geological features of the data. Attributes can be displayed on seismic sections, time-slices, random intersections, surfaces and as volume renders where different values of the data can be made transparent. Volume extractions are useful to visualize the 3D extent of a feature. It creates envelopes around

specific amplitudes and generates a series of triangular surfaces forming a closed body of the amplitude anomaly.

3.4 Mapping fluid flow expressions

3.4.1 Sub-seabed focused fluid flow expressions

Based on the method described by Løseth et al (2008) for observing and describing seismic anomalies, eight parameters were collected to determine distorted reflections defining vertical zones. These parameters were root, top, vertical extent, width, area, shape, associated amplitude anomaly and finally anomalous pattern and additional information. In addition to their inline and crossline location were used.

Root and top describes at which level the zone has its origin and termination and the vertical extent is the distance in between these two. The width is measured from edge to edge of the distortion of the reflections, this gives an idea of the width of the feature. The actual pipe-feature may be much smaller because it can be surrounded by acoustic masking. The area is calculated as a simple ellipse (longest radius*shortest radius*π). The associated amplitude anomalies are described using a set of terms described in Table 3.3 and anomalous pattern terms described in Table 3.4. These parameters were used to determine vertical fluid flow expressions.

Table 3.3. Descriptive amplitude anomaly terms. From Løseth et al (2008).

Term	Definition
Brights, bright spot or high amplitude anomaly	Local increase in positive or negative amplitude along a reflection for any reason.
Dim spot (or dim zone)	Local decrease in positive or negative amplitude along a reflection or in a zone for any reason.
V-shaped bright	High amplitude V-shaped reflection in vertical section that is discordant to reflections from depositional surfaces. Seldom more that 2–3 km wide.
Flat spot	Relatively flat seismic reflection with an angle to the stratigraphic reflections.
Phase reversal	Phase shift of 180° along a continuous reflection, so that a peak becomes a trough and vice versa.
Reduced continuity	Local reduction of continuity of a seismic event.
Increased continuity	Local increase of continuity of a seismic event.
Reduced frequency	Local decrease of frequency.
Bottom simulating reflectors (BSR)	High amplitude reflection that often is parallel to seabed.

Table 3.4. Terms describing anomalous patterns on seismic data. From Løseth et al. (2008).

Term	Definition
Vertical wipe-out zone	The area on a seismic section where the reflections from the stratigraphic layers are deteriorated so the primary reflections either are absent or very weak.
Vertical dim zone	The area on a seismic section where the reflections from the stratigraphic layers are visible but have lower continuity and amplitude than in adjacent areas.
Vertical high amplitude or bright zone	The area on a seismic section where several high amplitude reflection anomalies occur that naturally can be grouped together.
Discontinuity zone	The area on a seismic section where the reflections from the stratigraphic layers are more discontinuous than in adjacent areas.
Chaotic reflection zone	The area on a seismic section where the reflection pattern is chaotic compared to adjacent areas.
Local depression features	Negative real down-bending or sag of a seismic reflection. The underlying reflections can be truncated, be parallel to the described structure or they can have any type of reflection pattern (e.g., chaotic).
Mounds	Positive structure of any shape rising above the normal top of a reflection. The reflection pattern below the mound can be of any type.
Push down	Apparent down-bending produced by a local, shallower low-velocity region.
Pull up	Apparent uplift produced by a local, shallower high-velocity region.

3.4.2 Seafloor fluid flow expressions

A total of six parameters, in addition to inline and crossline location, were collected for the pockmark-like depressions on the seafloor. The parameters were length of longest axis, length of the shortest axis, area, azimuth of longest axis, depth of depression from the surrounding rim and water depth to bottom of depression.

The longest axis was determined from visual inspection of the interpreted upper zero crossing of the seafloor reflection and the area was, as with the vertical zones of distorted reflections, calculated as a simple ellipse (longest radius*shortest radius*π). The measurements of the azimuth of the longest axis contain uncertainties due to the sub-circular appearance of the depressions. The depression depths were calculated using a speed of sound in water of 1480 m/s.

The dense distribution of ploughmarks makes recognizing pockmarks a difficult task. Ploughmarks are typically 100–300 m wide, with a relief of 3–10 m (Andreassen et al., 2008). Normal pockmarks are 10-700 m wide and up to 45 m deep, but giant pockmarks may reach

more than a kilometer in diameter (Hovland et al., 2002). By enlarging the grid-size of the data when converting the interpreted seafloor to a surface it is possible to smooth smaller features (ploughmarks and small pockmarks) and make larger depressions more distinguishable.

4 RESULTS

The fluid flow systems of the Veslemøy High area are interpreted predominantly from key seismic horizons and units, and the analysis of attribute cubes, slices and attribute maps. It allowed identifying features indicative for the fluid flow system in the area. The features are mainly based on high amplitude anomalies, polarity and velocity effects in seismic data, vertical zones of distorted reflections, and faults and unconformities. In addition, slides and debris flow deposits, channels and glacigenic erosional features have been recognized on the basis of their particular seismic facies (Bünz et al., 2003; Berndt, 2005; Andreassen et al., 2007b; Cartwright et al., 2007).

As the task of this thesis is to map fluid migration the results and discussion is arranged in a logical manner following fluid migration pathways. Veslemøy High is a Cretaceous high with the locality of the EL0001 3D seismic survey on top. This provides a natural division of the study area into a western and an eastern section (Figure 4.1). In the following, I shall first present amplitude anomalies from bottom (old) to top (young) in the eastern section and thereafter in the western section of the study area.

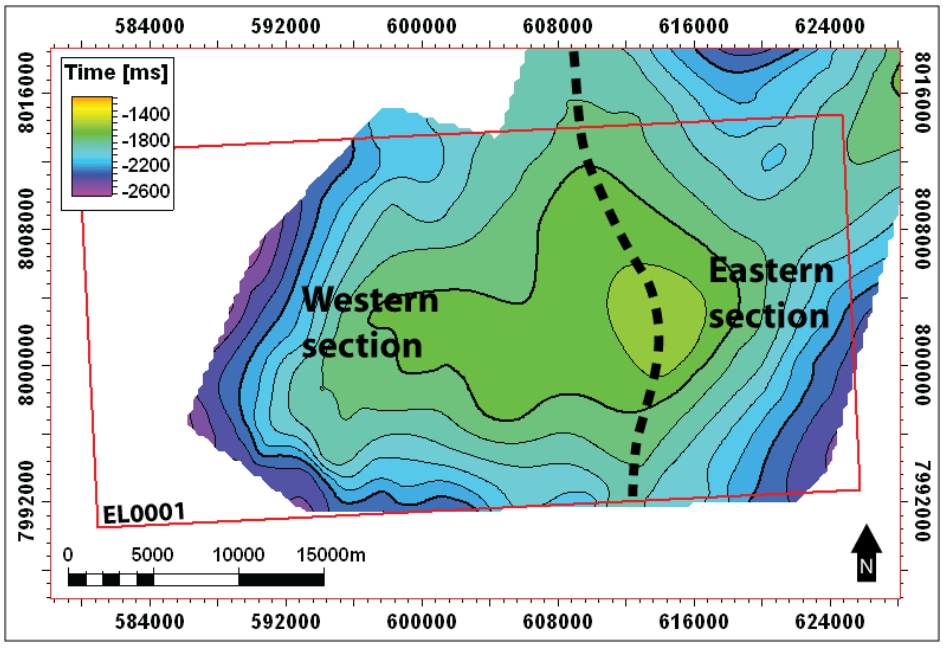

Figure 4.1. EL0001 3D seismic survey (red rectangle) displayed upon the Top Late Cretaceous/Late Paleocene reflector. A natural division of fluid migration into the study area, into a western and an eastern section, is provided by the apex of the Cretaceous high.

Large N-S trending normal faults with throws up to 500 ms extend trough the Cretaceous succession, fault-planes dipping towards west (Figure 2.3). In the western half of the survey these normal faults extend throughout the entire Tertiary package seen in Figure 4.2 and

partly into the Plio-Pleistocene. In the eastern section of the survey the faults are not as obvious within the Tertiary succession.

The mapped amplitude anomalies are mapped as they resemble indications of fluid accumulations as previously described in the literature (Laberg and Andreassen, 1996; Heggland, 1997, 1998; Fleischer et al., 2001; Mienert et al., 2005; Andreassen et al., 2007a; Hustoft et al., 2007; Løseth et al., 2008; Crutchley et al., in press).

4.1 Lateral high-amplitude anomalies (1-3) in sediments of Cretaceous and Paleogene (Paleocene-Eocene) age (eastern section)

The Cretaceous succession shows reflections only in its topmost section. No coherent reflections are visible below the Top Early Cretaceous reflector. At the top Late Cretaceous-Late Paleocene and top Early Cretaceous (see stratigraphy Figure 2.3) a continuous reflection with high amplitude prevails in all but the westernmost area of the survey (Figure 4.3b).

The Tertiary succession consists of sub-parallel reflections of varying amplitude and continuity that are offset by small faults in the east and large normal faults in the west (figure 4.1). Reflections of the Early Eocene succession have higher amplitude and continuity then lower reflections.

High amplitude reflectors also mark the top Early Cretaceous and the top Late Cretaceous/Late Paleocene in the eastern section of the survey.

Lower Tertiary sediments show several strong amplitude anomalies in the SE area of the 3D survey**;** these are named amplitude anomalies 1, 2 and 3 (Figure 4.3 and Figure 4.4).

Amplitude anomalies 1 and 2 (Figure 4.3) cover a total area of ~9 km2 in the southeastern section of the survey. The seismic anomalies occur within Late Paleocene to Early Eocene sediments in the lower part of the Tertiary succession. Both anomalies feature distinct top and bottom reflections.

The exact locations, depths, areal extent and other information of the anomalies can be found in Table 4.1.

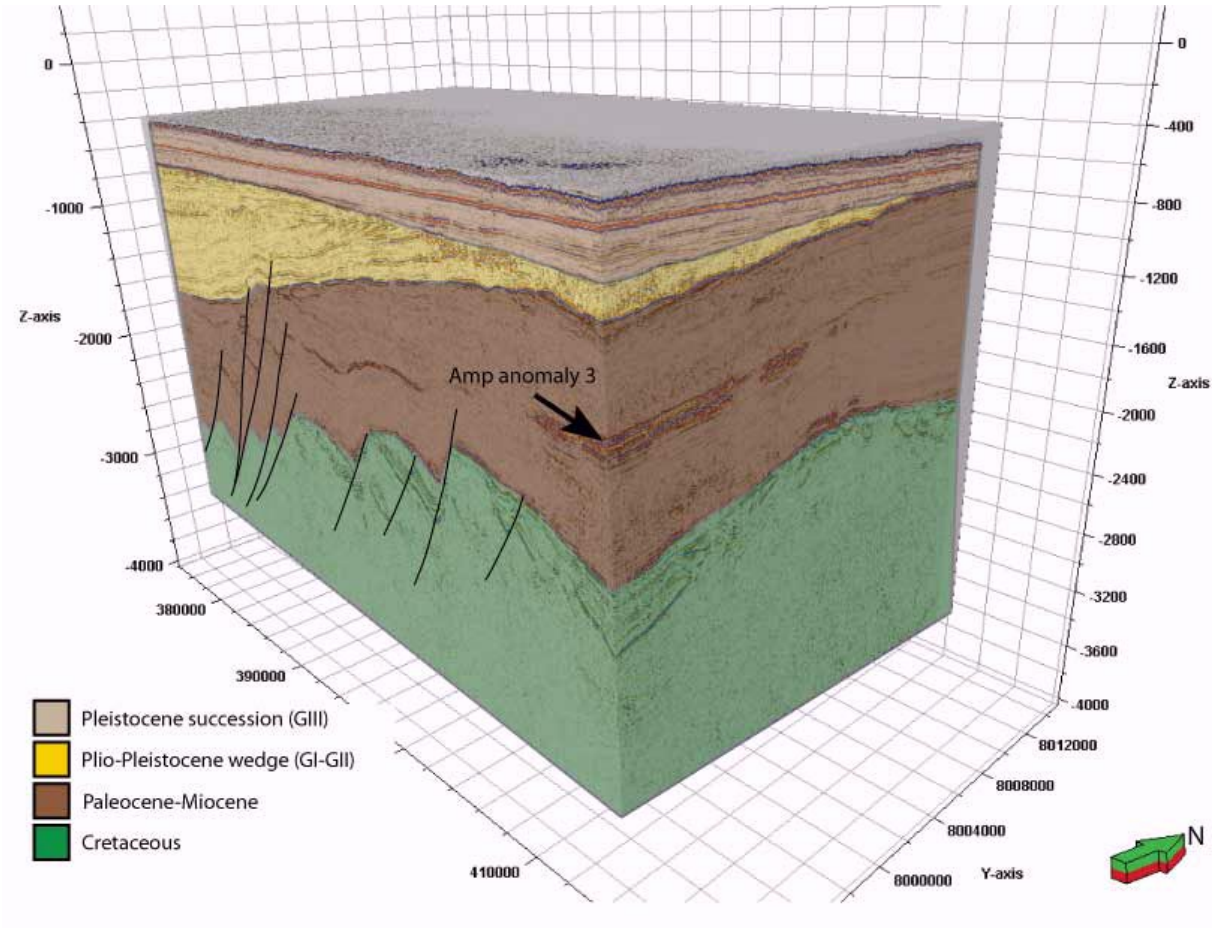

Figure 4.2. 3D image of the EL0001 survey (44 km by 21.5 km) seen from southeast with the Cretaceous, Tertiary (Paleocene-Miocene), Plio-Pleistocene wedge (GI-GII) and the Pleistocene succession (GIII) indicated. Amplitude anomaly 3 is indicated with an arrow, amplitude anomalies 1 and 2 are located within the cube and cannot be identified in this figure. Large NS trending, west-facing faults indicated with black lines.

Amplitude anomaly 1 is located in the SE part of the survey in Late Paleocene to Early Eocene sediments. The extent of the anomaly is 4.6 km SSW-NNE and up to 930 m WNW-ESE covering an area of 2.5 km^2. Top and bottom reflections are clearly distinguishable and the reflections join at the margin creating closed lobe shape. The high amplitudes show a negative polarity at the top and a positive polarity at the bottom reflections compared to the seafloor reflector. The inside of the interval shows chaotic reflections. It has a maximum vertical thickness of 105 ms TWT or 136.5 m (using a velocity of 2600 m/s). Beneath the bottom of the anomaly there is a 150 ms thick zone of acoustic masking that extends to the Top Late Cretaceous-Late Paleocene reflector (Figure 4.3b), this reflector shows a pull-down effect. Amplitude anomaly 1 connects to a large anomaly at Intra Pleistocene I (Amplitude anomaly 14, discussed below) (Figure 4.3a) via a vertical fluid flow pathway (feature 3, discussed in section 4.3).

Amplitude anomaly 2 is located east of anomaly 1 in the same interval. It features two main bodies with a thinner section connecting them (Figure 4.3a). The extent of the whole anomaly is 4.2 km E-W and up to 2.2 km N-S covering an area of 6.4 km^2. The appearance of this anomaly is very similar to anomaly 1 in that the top and bottom reflections join. It is slightly thinner then amplitude anomaly 1 with a maximum vertical thickness of 75 ms TWT calculated to 97.5 m using a velocity of 2600 m/s. A zone of acoustic masking exists also underneath anomaly 2. It extends down 200 ms to Top Late Cretaceous-Late Paleocene, whose reflection is locally also very strong and displays a pull-down effect beneath some areas of anomaly 2.

Figure 4.3 shows amplitude anomalies 1 and 2 that display a significant correlation with structural highs, faults and potential vertical fluid migration zones. The anomalies appear to be located at the apex of a structural high and are partly bounded by faults.

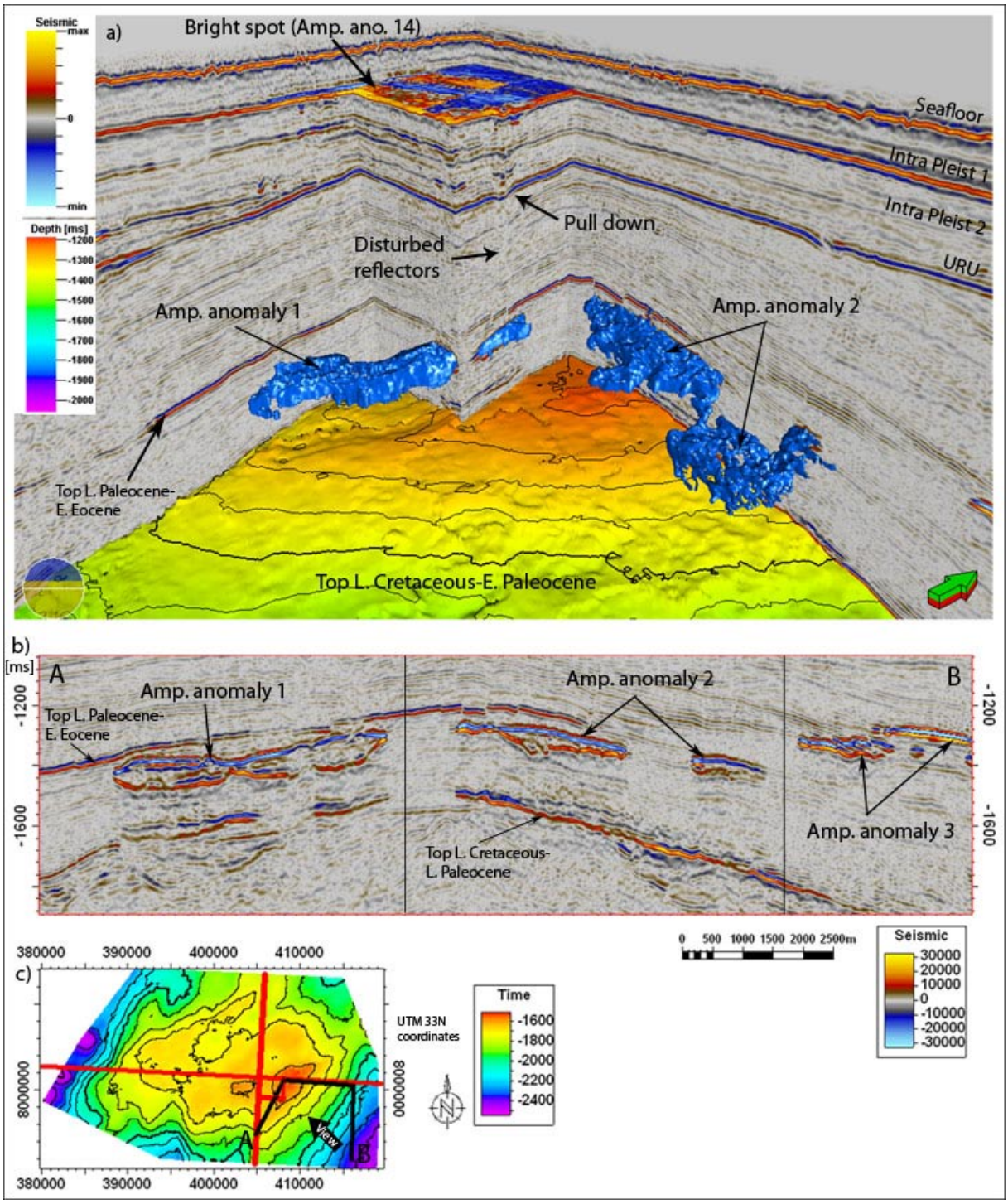

Figure 4.3 a) Image shows volume extractions of amplitude anomalies 1 and 2 (blue) displayed along with seismic (indicated as red lines in the map (c)). A vertical fluid migration pathway (vertical fluid flow feature 3) can be identified originating from the highest point of amplitude anomaly 1 and terminating in a bright spot (amplitude anomaly 14, discussed later) at Intra Pleistocene 1 level, along the path of this fluid pathway the URU reflection displays pull-down. b) Seismic section from A to B (black line in the map (c)) displaying the amplitude anomalies with negative polarity top reflections and positive polarity bottom reflections. The zone of masking underneath can also be easily identified. Also notice the high amplitudes of the reflection under the anomalies, the Top Late Paleocene/Late Cretaceous reflector. c) Map of location displaying the Top L. Cretaceous-L. Paleocene horizon. Red lines indicate seismic displayed in figure a). Black line indicates seismic displayed in figure b). The arrow indicates point of view in figure a).

Amplitude anomaly 3 (Figure 4.4) marks the upper part of a large fan-like structure that is extending beyond the 3D survey, therefore it is mapped using 2D seismic data. It is located in sediments of Early Eocene age and is by far the largest anomaly in the study area. It extends 54 km E-W and 36 km N-S covering a total area of 790 km^2. The amplitude anomaly marks an interval that displays a strong negative top reflection. A positive reflection can be observed beneath the negative top reflection in some of the seismic sections (Figure 4.4a). The distance between these reflections in Figure 4.4a is on average 90 ms TWT, which corresponds to a distance of 110 m using a velocity of 2500 m/s. In the 2D seismic line shown in Figure 4.4a it appears as if the lower reflection crosscuts other reflections in the lowermost section of the amplitude anomaly creating what may resemble a flat-spot. The distance from the top negative reflection to the lower positive reflection varies. The vertical TWT varies from 112 ms in the center section to less than 80 ms to the north and south (Figure 4.4b). It is not likely that the lower reflection is a multiple (for example a peg-leg multiple) from the top reflection as a multiple from the top reflection would be located at a more constant distance from the top reflection. It may be the bottom reflection of the anomaly or just a positive impedance contrast of normally compacted sediments below the anomaly.

Overlying reflections are arranged in an oblique progradational pattern down-lapping onto amplitude anomaly 3. Underlying reflections display varying high and low amplitudes in a largely chaotic pattern. The zone of acoustic masking beneath the anomaly is extensive, stretching 1000 ms TWT down below the anomaly. This makes identifying a possible bottom reflection difficult.

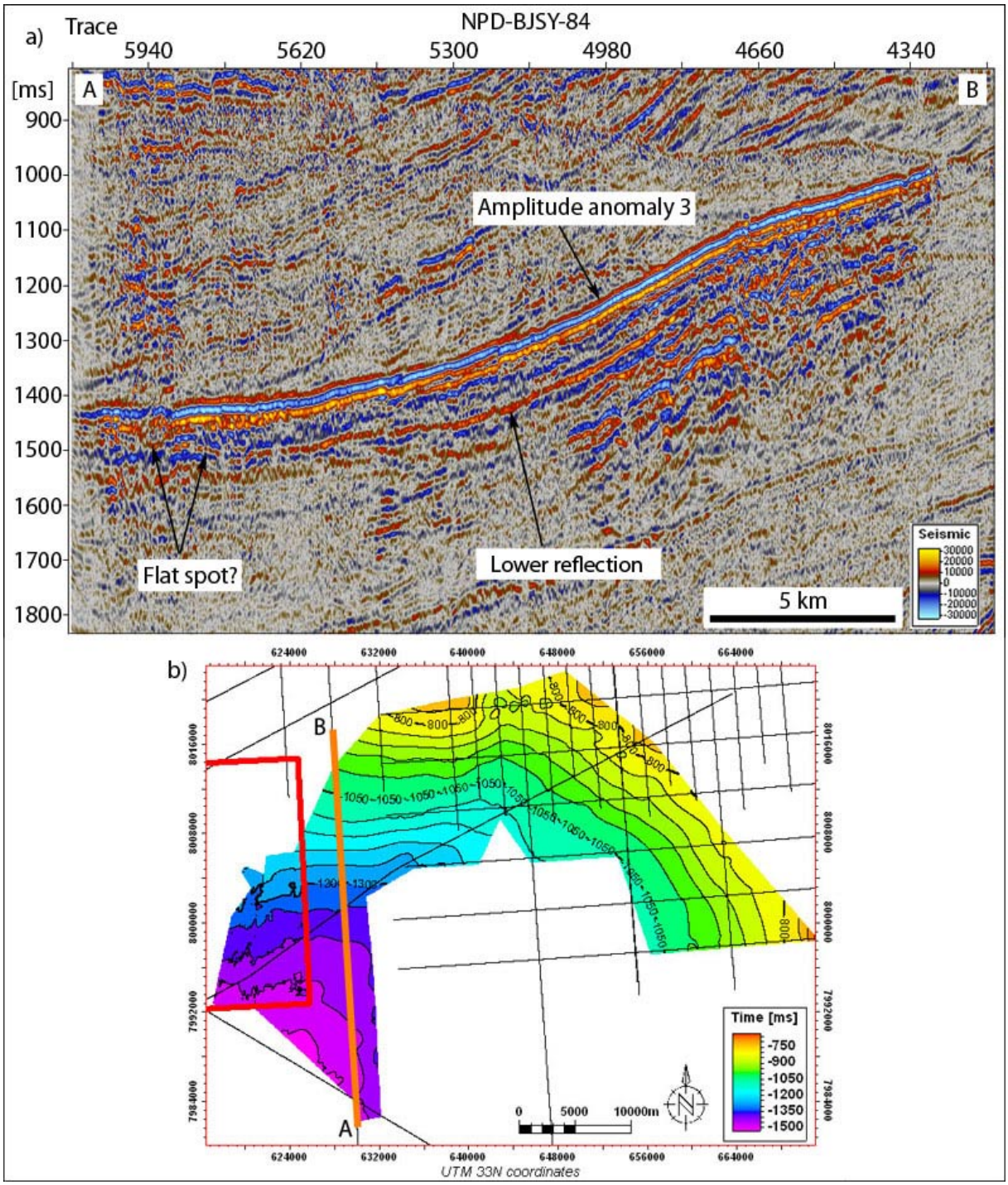

Figure 4.4. a) Amplitude anomaly 3 indicated in 2D line 184500-84 from the survey NPD-BJSY-84. A lower reflection and a possible flat spot indicated. Location indicated in figure b).
b) The extent of Amplitude anomaly 3 displayed in timescale with contour interval 50 m. The anomaly reaches partly into the 3D survey (red rectangle), outside the 3D survey it is mapped using a grid of 2D seismic lines (black lines). Intersection displayed in figure a) is marked with an orange line.

4.2 Lateral high-amplitude anomalies (4-9) in sediments of Neogene age (Plio-Pleistocene wedge (GI-GII) and the Pleistocene succession (GIII)) (western section)

High amplitude anomalies in the western section predominantly occur in Plio-Pleistocene wedge (GI-GII) and the Pleistocene succession (GIII) above it (see location of units in Figure 4.5). The Plio-Pleistocene wedge consists of oblique progradational reflections.

The Plio-Pleistocene wedge contains a large number of amplitude anomalies. They concentrate in the western section of the survey. The mapped amplitude anomalies resemble indications of fluid accumulations as previously described in the literature (Laberg and Andreassen, 1996; Heggland, 1997, 1998; Fleischer et al., 2001; Mienert et al., 2005; Andreassen et al., 2007a; Hustoft et al., 2007; Løseth et al., 2008; Crutchley et al., in press). The reflections display varying high and low amplitudes that occur vertically with generally high continuity (Figure 4.6). The Plio-Pleistocene wedge has abundant high amplitude anomalies indicating the presence of gas and fluid migration pathways, it also contains many anomalies resembling features created by interference effects, mass movement deposits, channels, rafted sediment blocks (e.g. Andreassen et al., 2007b) and other features related to the glaciomarine depositional environment. The lowermost unit within the Plio-Pleistocene wedge, GI, has been interpreted as shelf margin deltaic facies in the Sørvestsnaget Basin (Andreassen et al., 2007a) and has similar seismic appearance in Veslemøy High. GII is, similar to in the Sørvestsnaget Basin (Andreassen et al., 2007a), interpreted to be slope facies with common occurrence of sediment blocks.

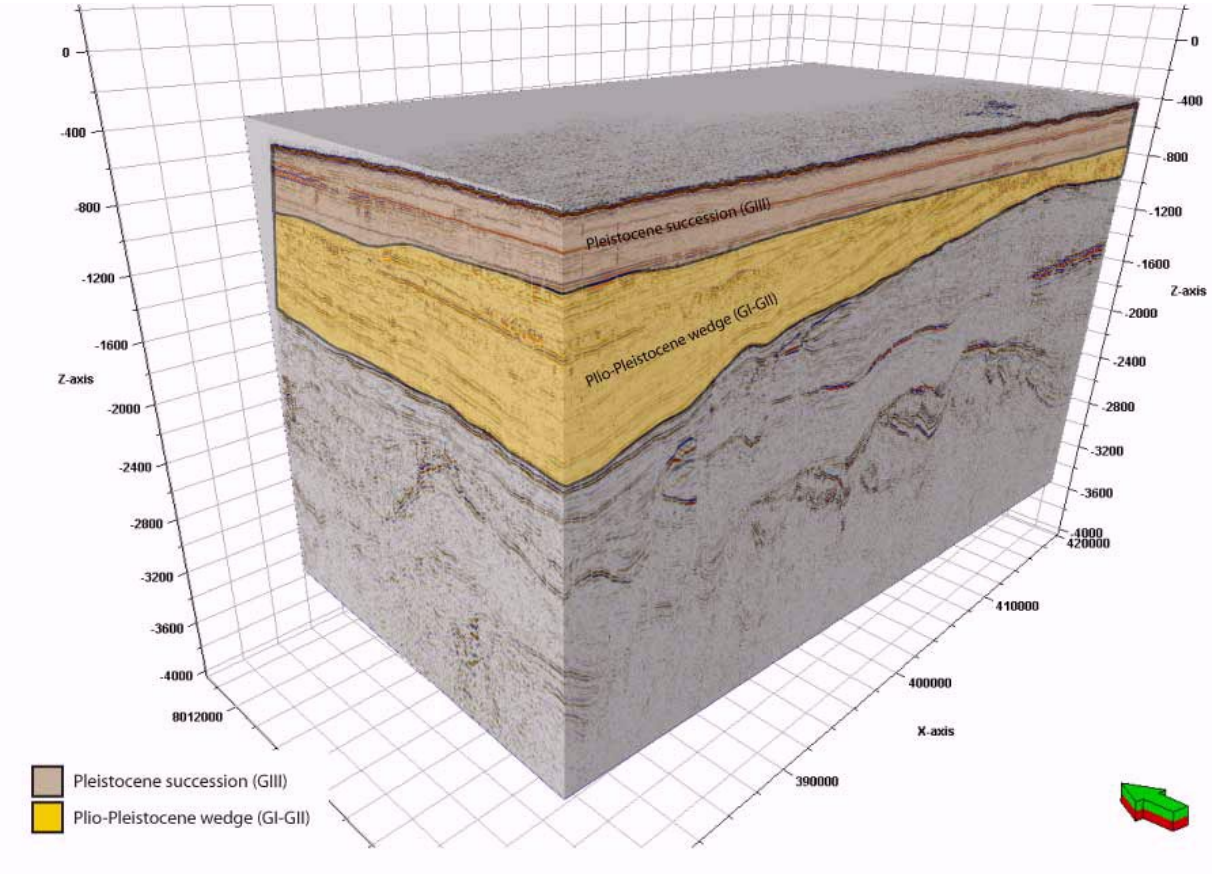

Figure 4.5. 3D image of the EL0001 survey seen from southwest with the Plio-Pleistocene wedge (GI-GII) and the Pleistocene succession (GIII) indicated in yellow and beige respectively. The Plio-Pleistocene wedge is 582-961 ms thick in the west and extends 17.5 km into the dataset in the northern section and throughout the entire dataset in the southern section. The top of the wedge, reflector R1 (ca 200-440 ka) (Faleide et al., 1996), has a depth varying from 665 ms to 927 ms. The bottom reflector of the wedge, reflector R7 (ca 2.3-2.5 Ma (Faleide et al., 1996)), has a depth varying from 786 ms to 1732 ms. The reflections have an average angle of 2.3 degrees, if a constant velocity is assumed. Slightly larger if one assumes the velocity increases with depth.

The Pleistocene succession consists of sub-horizontal parallel reflections (Figure 4.5). Two distinct reflections stand out in the succession, and they are named from top to bottom Intra Pleistocene 1 and Intra Pleistocene 2 (Figure 2.3). Except for the two main reflections the Pleistocene successions reflections have overall low continuity and amplitudes. Localized areas of disturbed reflections and bright spots are identified within the succession. Bright spots are commonly associated with these two reflections.

Due to the large number of amplitude anomalies in the Plio-Pleistocene Wedge (GI-GII) only the most distinctive and most important anomalies related to fluid migration will be described in this thesis. Inline 900 displays the typical appearance of the wedge and the amplitude anomalies (Figure 4.6). Six amplitude anomalies observed in this inline are described as examples for typical anomalies. In addition, five other amplitude anomalies located within the

Plio-Pleistocene wedge (GI-GII) are described (Figure 4.14, Figure 4.15, Figure 4.16, Figure 4.17, Figure 4.18 and Figure 4.19).

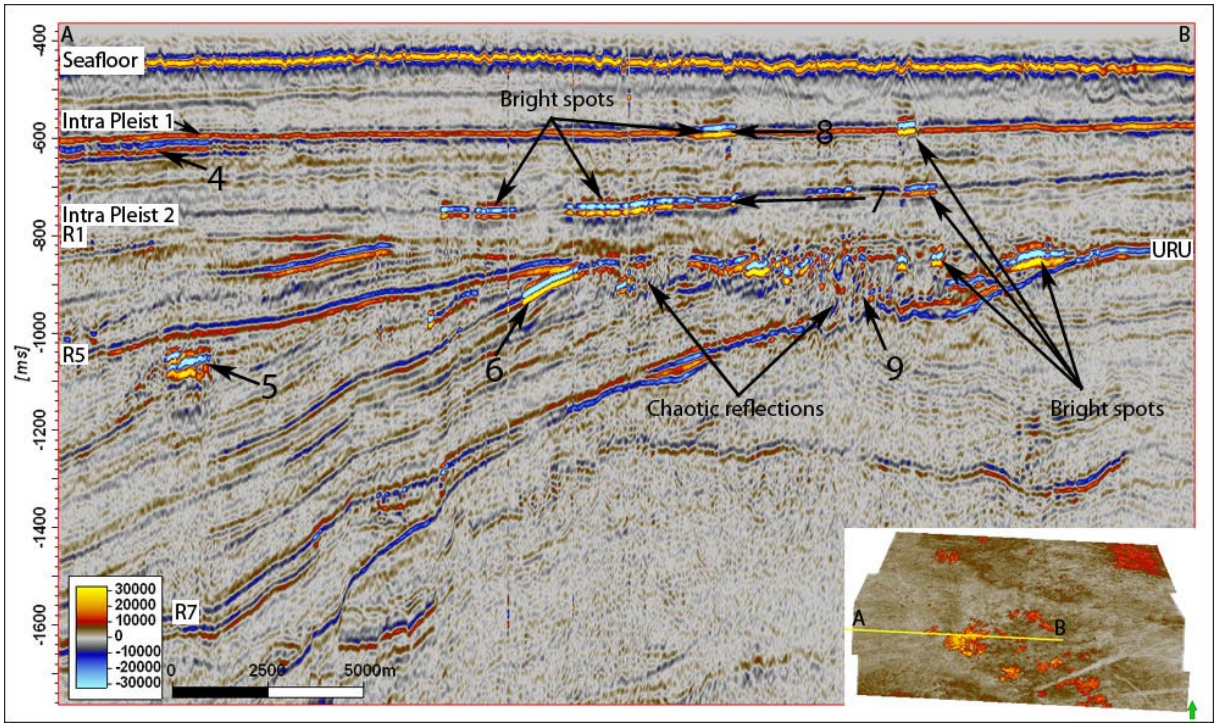

Figure 4.6. Inline 900 between crossline 460 in the west and 2630 in the east. Location of seismic intersection in inlet map. High amplitude anomalies 4-9 are marked by arrows and displayed in figures below; Anomaly 4: Figure 4.7; anomaly 5: Figure 4.8; anomaly 6: Figure 4.9; anomaly 7 and 8: Figure 4.11 and finally anomaly 9: Figure 4.13.

In inline 900 the amplitude anomalies are located mainly in the top middle to eastern section of the Plio-Pleistocene wedge (Figure 4.6). They occur underneath the toplap unconformity which constitutes the R1 reflection but bright spots are also common in the Pleistocene succession above R1.

Amplitude anomaly 4 (Figure 4.6 and Figure 4.7) is a large feature (9.5 km long (NE-SW) and 4.5 km wide (NW-SE) covering an area of 27.5 km^2). The polarity of the anomaly is unclear as several reflections interfere. It is located in the far western section of the survey at 600-645 ms TWT, within the Pleistocene succession.

When displaying the amplitude anomaly as a RMS time-slice the anomaly has the characteristic appearance of a mass movement deposit. It has a very low gradient that is difficult to measure accurately but it may be as low as 0.3 degrees.

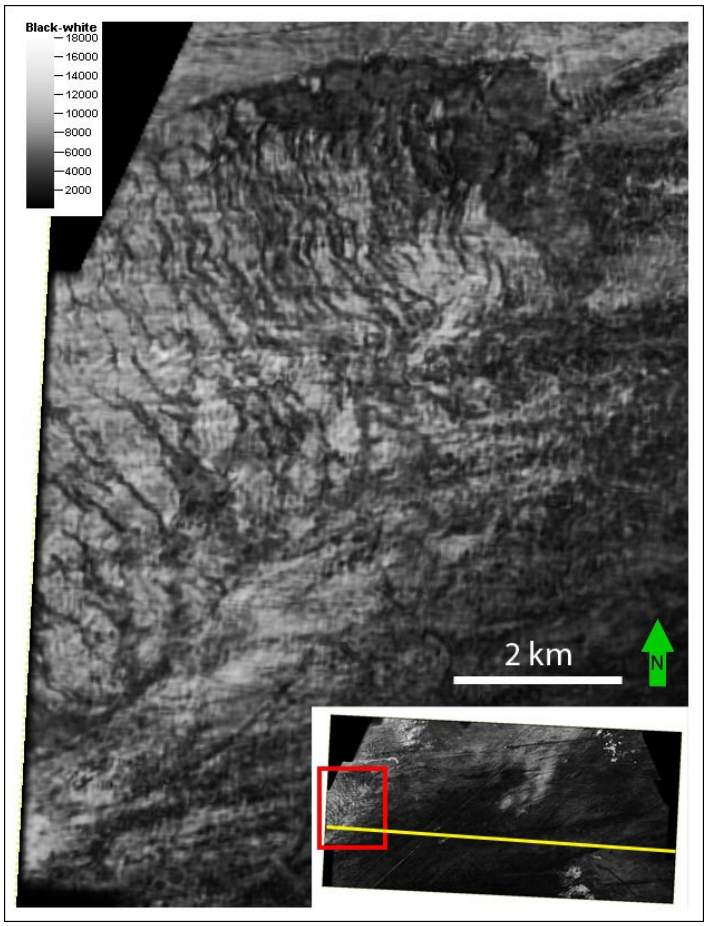

Figure 4.7. RMS amplitude time-slice at 629 ms displaying amplitude anomaly 4 in gray-scale to enhance subtle features. Inline 900 from Figure 4.6 marked in yellow.

Amplitude anomaly 5 (Figure 4.6 and Figure 4.8) is located within the Plio-Pleistocene wedge in the western part of the dataset. Its overall appearance is slightly curved following the shape of the layers. It covers an area of 4.5 km^2, and displays high amplitudes with negative polarity. The amplitude anomaly is situated close to the toplap unconformity underneath the R5 reflector (Figure 4.8b). When looked at in a RMS amplitude slice (Figure 4.8a) the anomaly displays a chaotic blocky appearance. Underneath the anomaly is a zone of acoustic masking that reaches down 500 ms TWT (Figure 4.8b). The zone of acoustic masking interrupts reflections that resemble a low frequency and possible pull-down effect.

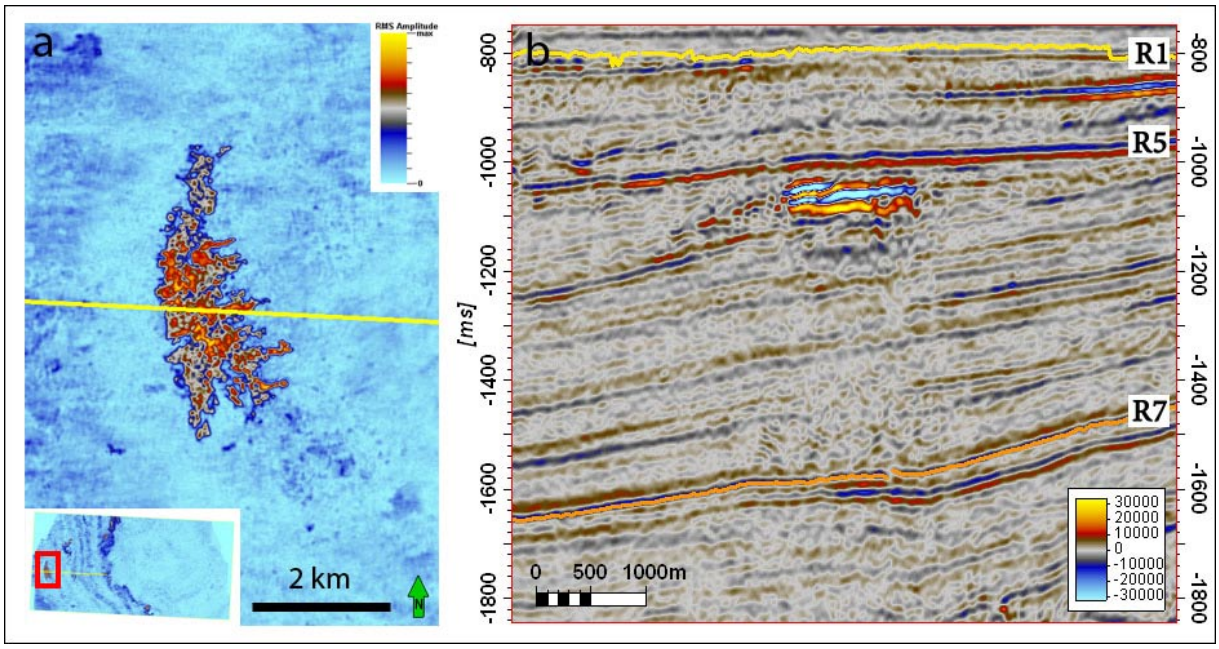

Figure 4.8. a) RMS amplitude time-slice at 1050 ms displaying amplitude anomaly 5. b) Close-up on the amplitude anomaly on inline 900. R1 (yellow), R5 and R7 (orange) indicated.

Amplitude anomaly 6 (Figure 4.6 and Figure 4.9) consists of a group of anomalies covering a total area of 26 km^2. The anomaly is subdivided into anomaly 6.1, 6.2 and 6.3. Amplitude anomalies 6.1 and 6.3 have their apexes directly beneath amplitude anomaly 7. Amplitude anomaly 6.3 has its apex beneath anomaly 11. The anomalies are connected to the above anomalies with vertical fluid migration pathways (feature 18, 19 and 24, discussed in section 4.3). The reflections display high amplitudes and negative polarity. The anomalies coincide with the toplap termination of the Plio-Pleistocene wedge (R1), underneath the Pleistocene succession (Figure 4.9b). Interesting to note, the anomalies have irregular shapes in the eastern topmost section and appear to be flat in the lower western section. The lower terminations on the bright spots are laterally at a constant two-way time. The flat spots in the western edge align with three different levels, namely ~928 ms TWT for the SW anomaly (amplitude anomaly 6.1), ~949 ms TWT for the NW anomaly (amplitude anomaly 6.2) and ~904 ms TWT for the SE anomaly (amplitude anomaly 6.3). This suggests that three non-connected compartments exists in which fluids have accumulated. The other anomalies within the amplitude anomaly 6 group are disturbed by chaotic reflections and a flat spot cannot be identified.

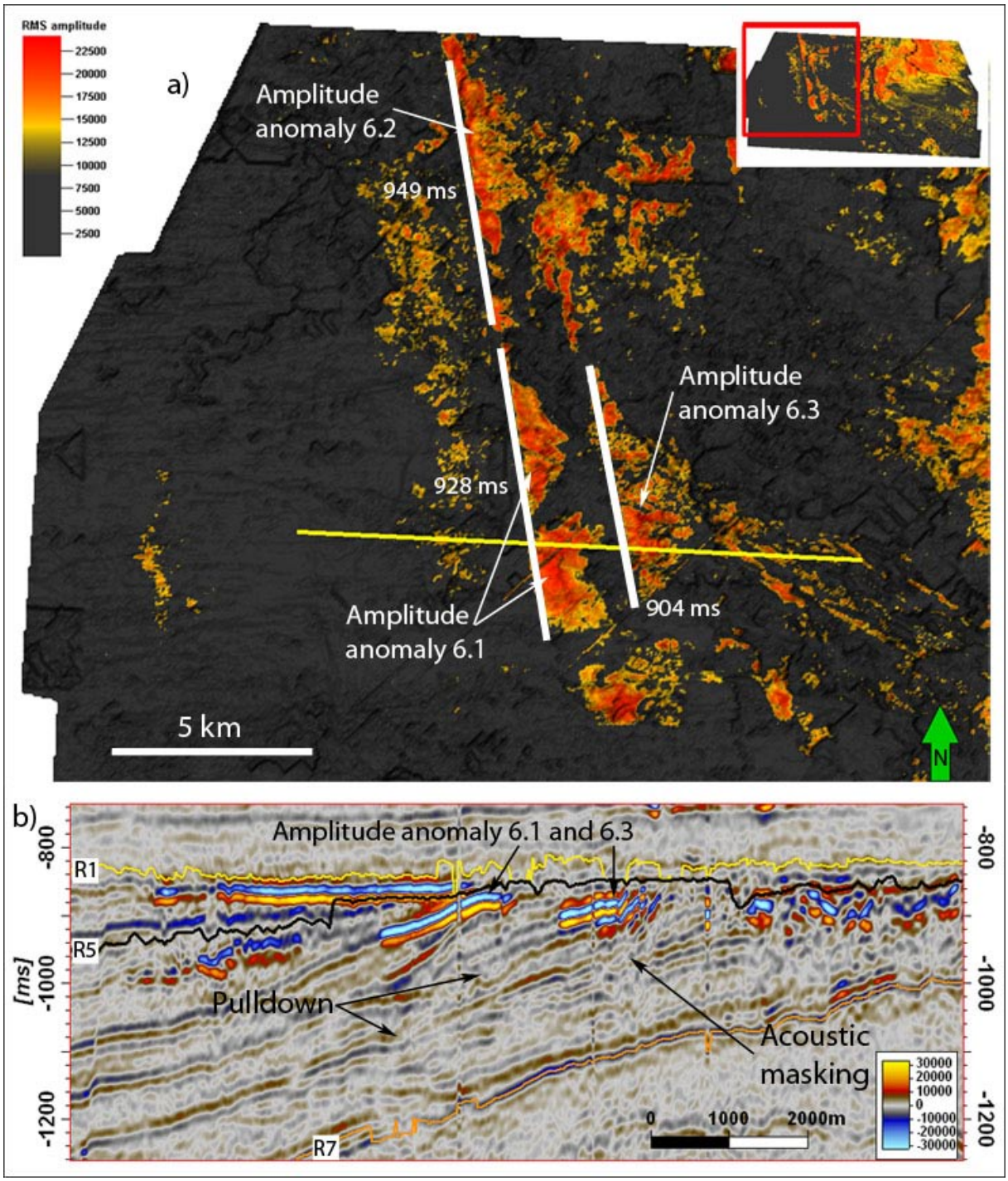

Figure 4.9. a) RMS amplitude map of the volume ±10 ms around the R5 reflection displayed upon the R5 reflection. Amplitude anomaly 6.1, 6.2 and 6.3 marked with white arrows. b) Inline 980 displaying amplitude anomalies in the truncated layers below the R1 reflection. Possible pull down can be identified underneath the westernmost anomaly and acoustic masking underneath the rightmost anomaly. R1 reflector marked in yellow, R5 in black and R7 in orange.

As the amplitude anomaly 6 is associated with a toplap unconformity the reflections may interact and give rise to tuning effects. This may be misinterpreted as high amplitude anomalies due to lithological or fluid changes.

Figure 4.10 displays a close-up of amplitude anomaly 6.1 and the above reflection. The eastern part of the anomaly shows interference of the reflection from amplitude anomaly 6.1 and the reflection above but the western part shows two separate reflections without interference. Amplitude anomaly 6 is therefore caused by either sub-seismic reflections creating positive interference or alternatively by a negative and strong, acoustic impedance contrast due to changes in the physical properties of sediments or fluid content. Reflections underneath the anomalies indicate reduced frequency, amplitude and continuity along with local pull-down effects (Figure 4.9).

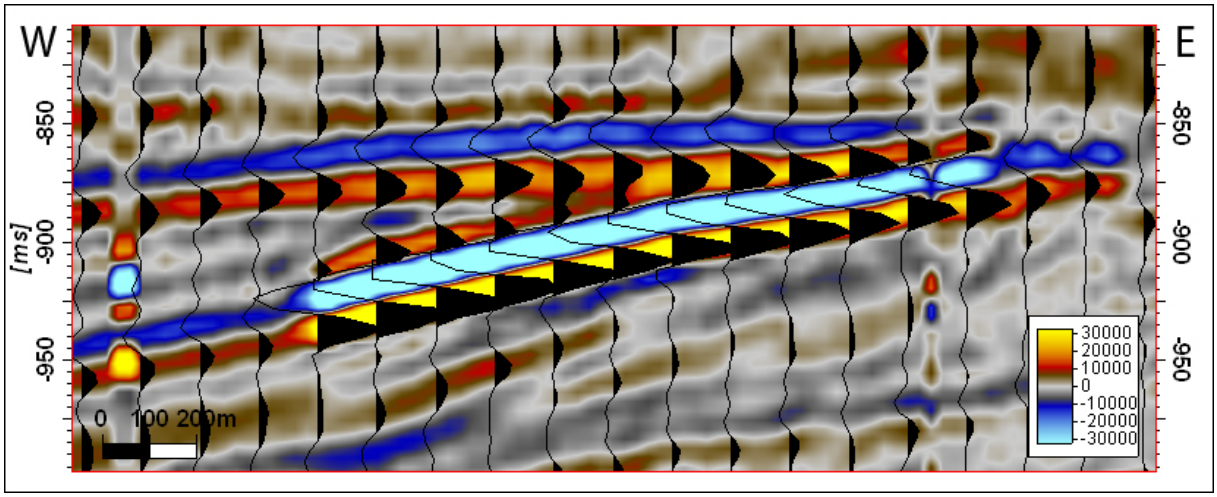

Figure 4.10. Close-up of amplitude anomaly 3 on inline 900 with wiggle traces, every 10th trace displayed. Wiggle trace peaks filled with black. The data show merging reflectors and interference towards the east.

Amplitude anomaly 7 (Figure 4.6, Figure 4.11 and Figure 4.12) is located at the Intra Pleistocene 2 reflector within the Pleistocene succession. The anomaly covers an area of 16.5 km^2. It displays a negative polarity and the reflections below show a reduced frequency (Figure 4.12) and disturbed reflections. Pull-down effects are difficult to identify due to the uneven character of the underlying reflections (Figure 4.11). The location of amplitude anomaly 7 is directly above the apex of amplitude anomaly 6.1 and it has a random cloud-like appearance not resembling other glacial sedimentary or erosional features found in the area. Anomaly 7 is interconnected to anomaly 6 below and anomaly 8 above via vertical fluid flow pathways (discussed in section 4.3).

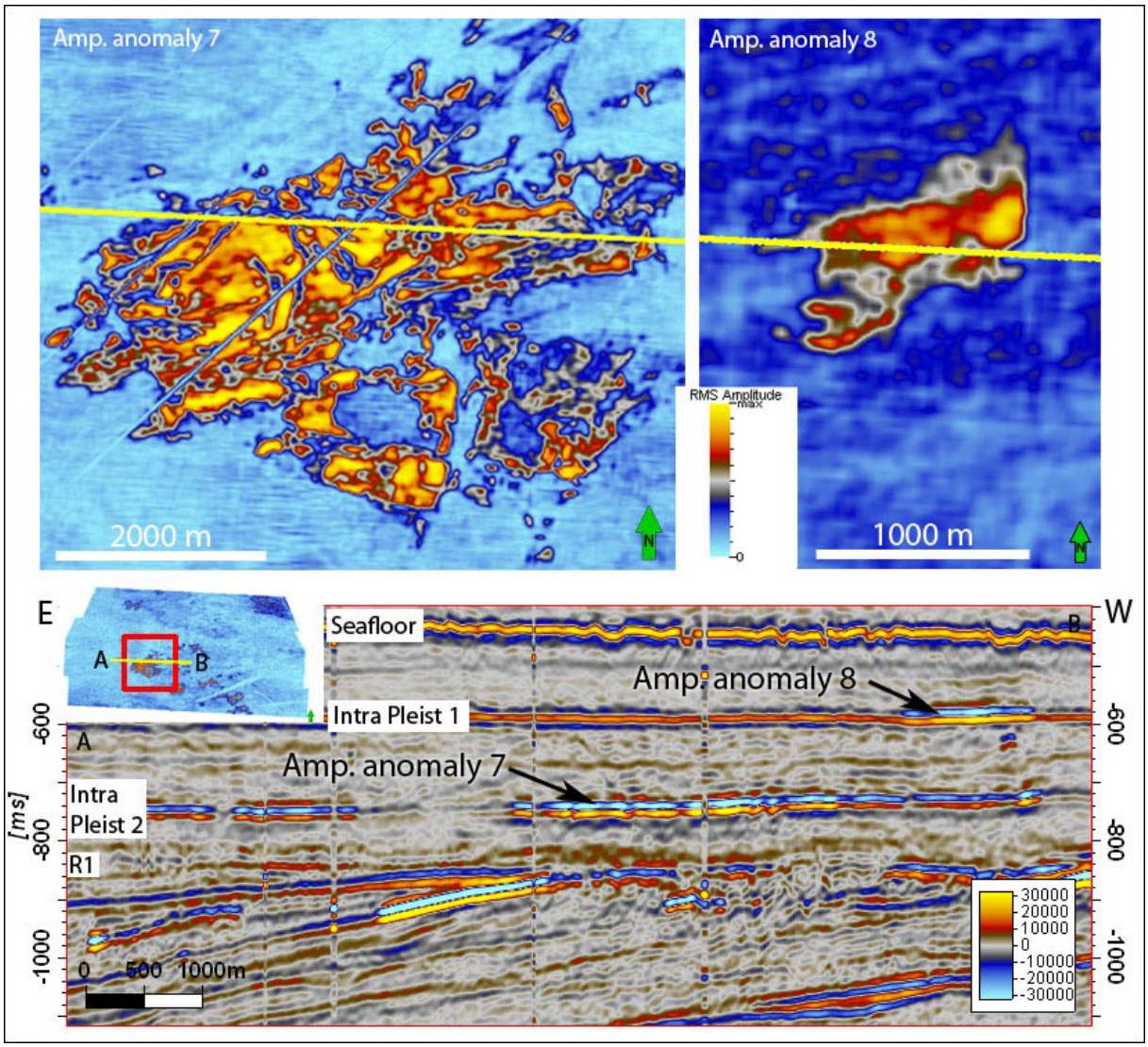

Figure 4.11. RMS amplitude time-slices of amplitude anomaly 7 (top left) and 8 (top right) and seismic section of inline 900 (bottom).

Amplitude anomaly 8 (Figure 4.11, Figure 4.12 and Figure 4.18) is situated immediately above amplitude anomaly 7, at Intra Pleistocene 1 level, and is significantly smaller. The area of the amplitude is only 0.3 km^2. The anomaly features high amplitudes and a negative polarity. Amplitude anomaly 8 may appear to be interconnected by weak vertical fluid flow pathways to anomaly 7 beneath.

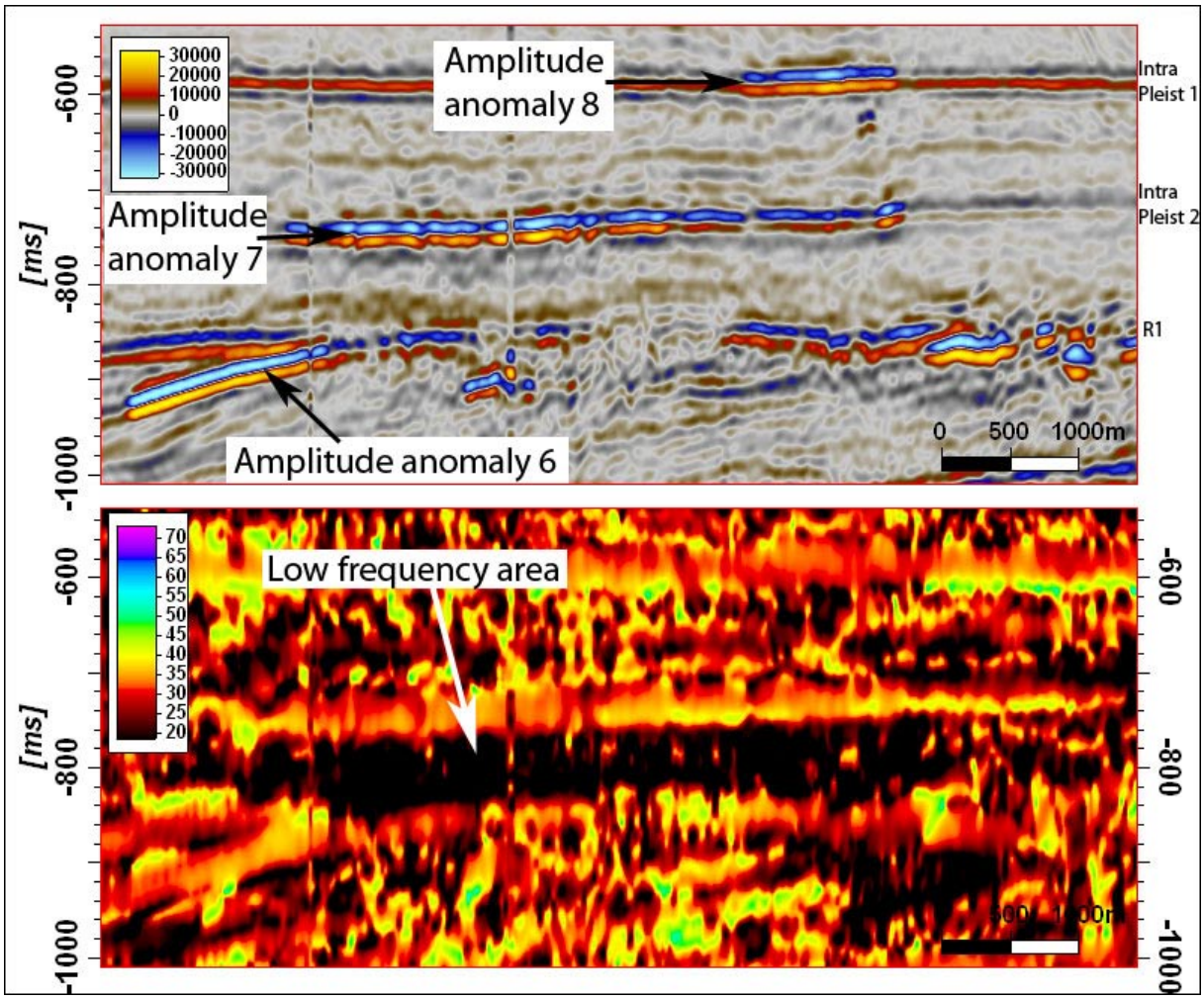

Figure 4.12. Amplitude anomalies 6, 7 and 8 displayed in; Top) Seismic inline 900, Bottom) Instantaneous frequency of inline 900 showing a distinct low frequency area beneath the large anomaly 7. Less clear low frequency areas can also be identified beneath amplitude anomaly 6 and 8.

Amplitude anomaly 9 (Figure 4.6 and Figure 4.13) is more of an area of chaotic and high amplitude reflections at the south-east section of the Plio-Pleistocene wedge, then a confined amplitude anomaly. The feature extends 15 km in a NW-SE direction and 5 km in a SW-NE direction covering a total area of 36 km^2. The high-amplitude reflections show a low continuity in a chaotic to imbricated configuration. The RMS amplitude slice displays the pattern extending NW-SE (Figure 4.13). The inclination of the paleoslope is towards NE, and contrary to the overall inclination of the reflections in the wedge. A trough with chaotic reflections exists in between the Plio-Pleistocene wedge in the SW, with its southwestwards dipping reflections, and the Early Eocene sediments succession in the NE. Many fluid flow expressions originate in the chaotic reflections of this area. The vertical fluid flow expressions extend through the Pleistocene succession and an abundance of bright spots are localized above (discussed in section 4.3). Beneath the anomaly is an area of acoustic masking (Figure 4.13).

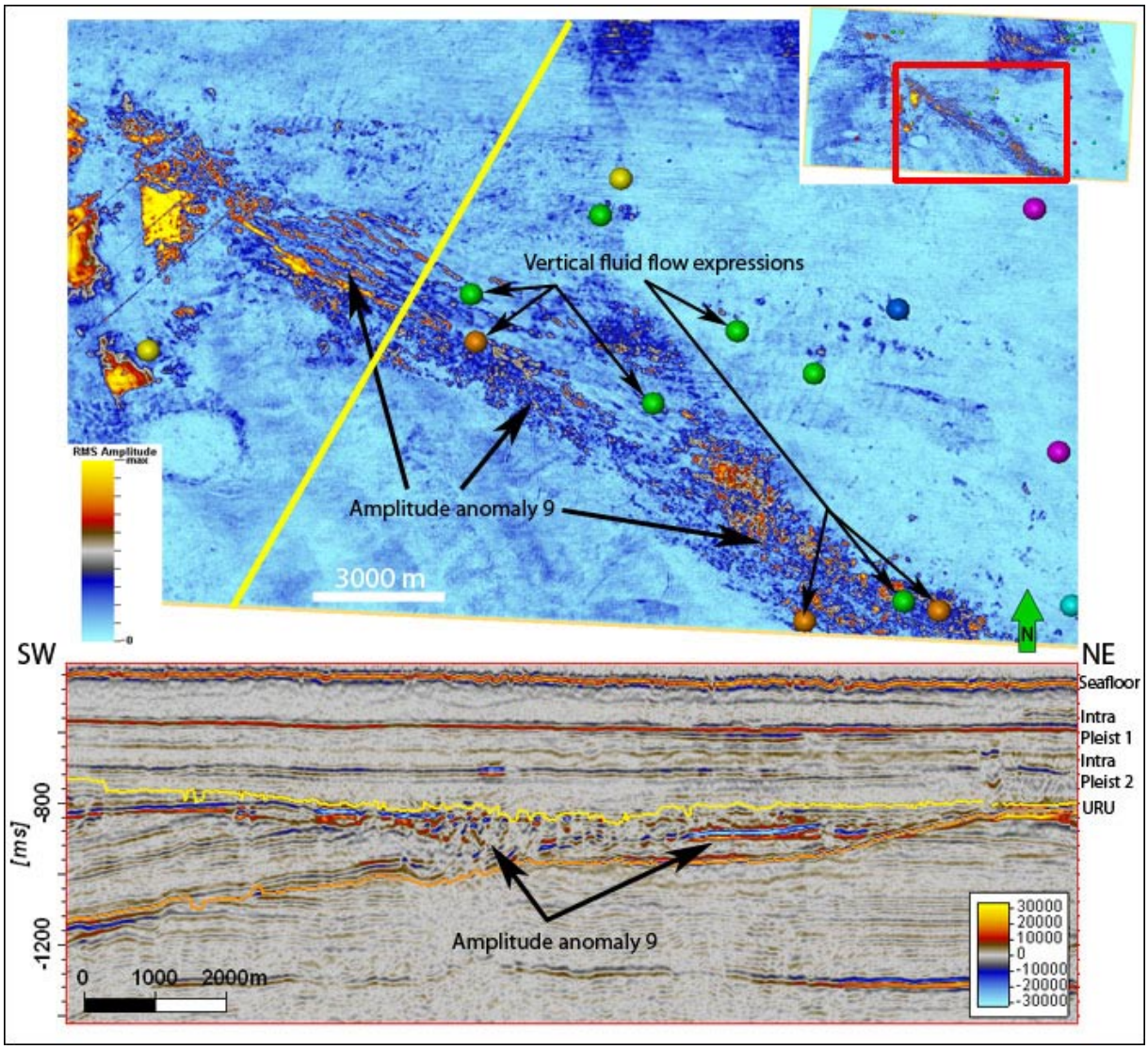

Figure 4.13. Top) RMS amplitude time-slice at 854 ms TWT in gray-scale to enhance subtle features. The location of the random seismic intersection is indicated with a yellow line. Vertical fluid flow expressions indicated with dots (colour coded according to Figure 4.21) Bottom) A seismic intersection, SW-NE of amplitude anomaly 9, R1 reflector in yellow and R7 in orange.

Amplitude anomaly 10 is located directly above R7 in the northern section of the survey (Figure 4.14)**.** It stretches 12 km NE-SW and a maximum of 3.1 km NW-SE. The reflections of the anomaly display varying amplitudes with negative amplitudes as the strongest in the main section (Figure 4.14). Reflections below the main section of the anomaly also display pull-down and somewhat lowered frequencies. The anomaly shallows towards east. Displayed in an arbitrary RMS slice (Figure 4.14) the anomaly becomes narrower in its eastern shallower part and widespread in the deeper western part. The highest amplitudes are located within the shallower and narrower part. Towards the deeper sections the anomaly splits up into a more chaotic appearance with one larger laterally meandering section.

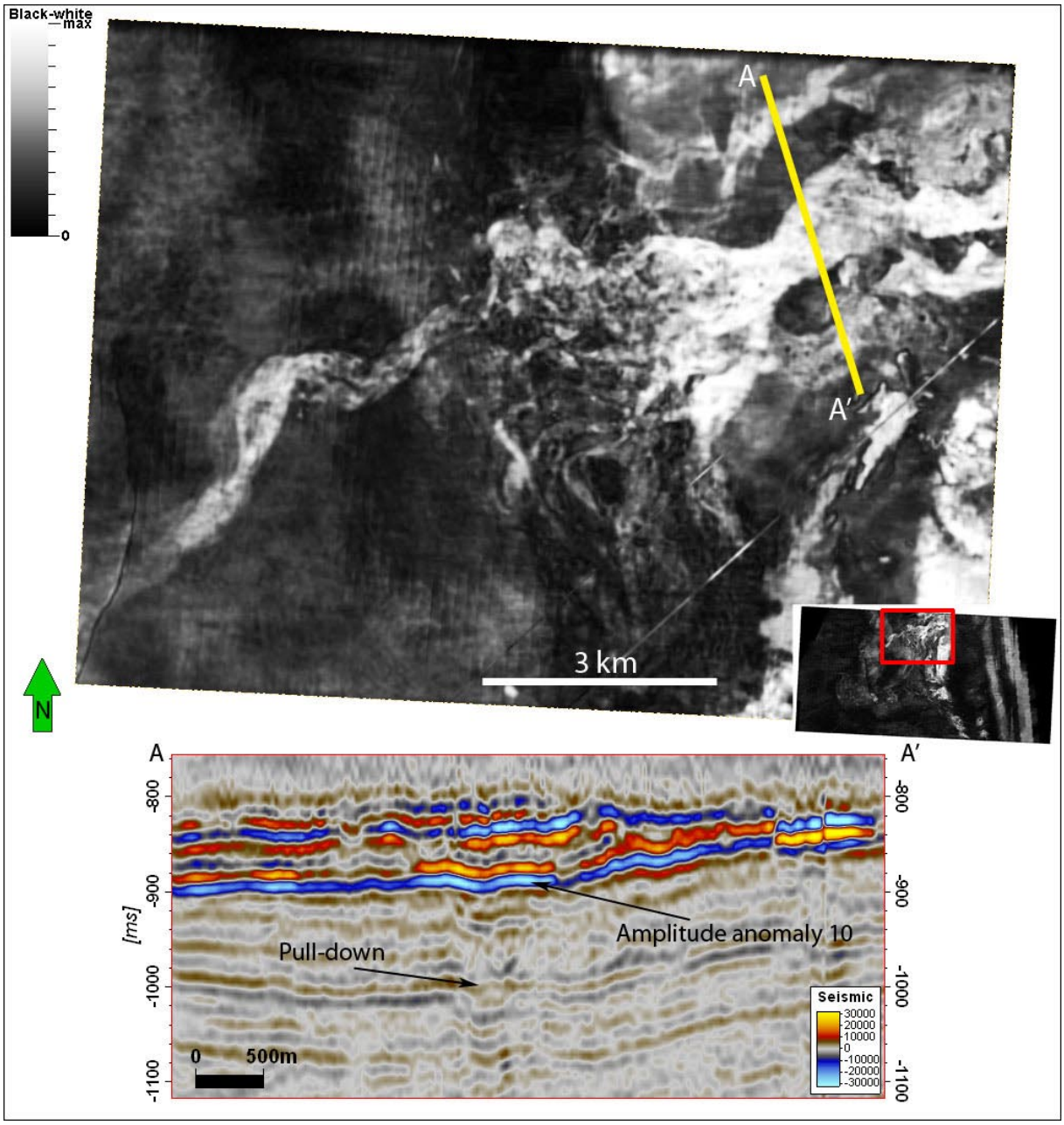

Figure 4.14. Top) Amplitude anomaly 10 displayed in an arbitrary RMS amplitude slice in gray-scale to enhance subtle features. The anomaly deepens towards west. Bottom) Seismic intersection (A-A') across the anomaly. Reflections beneath the anomaly show pull-down.

Amplitude anomalies 11, 12 and 13 concentrate along Intra Pleistocene 2 reflector (Figure 4.16), and so is amplitude anomaly 7. Accordingly they concentrate in the section of the Pleistocene succession (GIII) which is situated above the Plio-Pleistocene wedge (GI-GII).

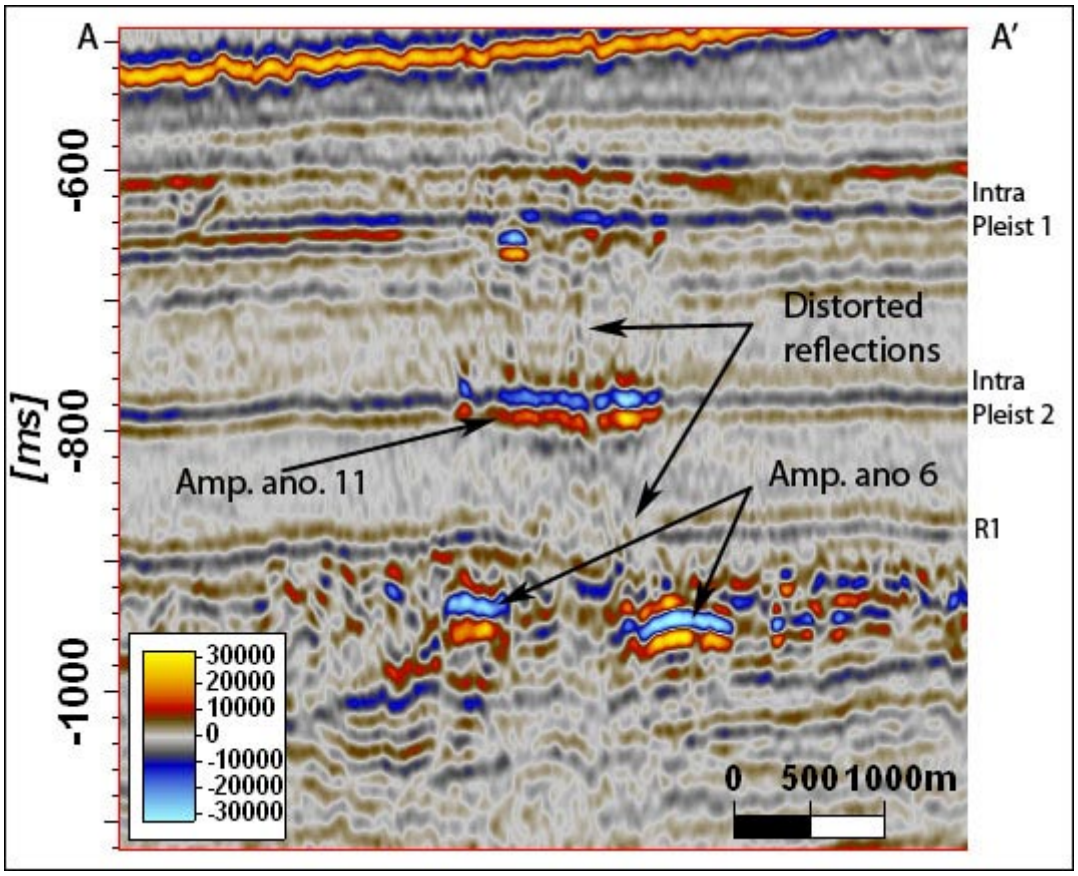

Figure 4.15 Seismic section of amplitude anomaly 11. Location of anomaly and intersection (A-A') is displayed in Figure 4.16.

Amplitude anomaly 11 (Figure 4.15 and Figure 4.16) extends within the Pleistocene succession (GIII) at 760-800 ms TWT. Anomaly 11 lies directly above the apex of amplitude anomaly 6.2 (Figure 4.15). Fluid flow pathways connect anomaly 6.2 and 11 (discussed in section 4.3). The anomaly can be followed 3.8 km east to west and 1.8 km north to south, covering an area of 4.6 km^2. It has negative polarity and stronger amplitude then the rest of the reflection. The area beneath and above the anomaly displays a reduced frequency and clear indications of upward migrating fluids (Figure 4.15).

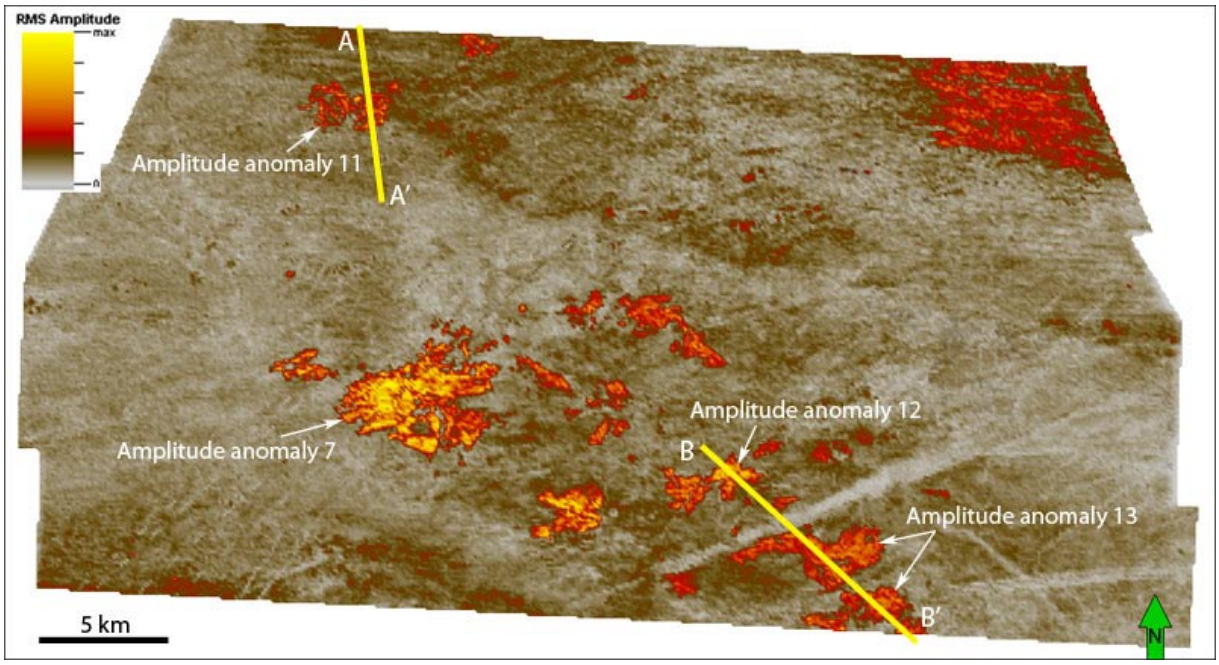

Figure 4.16. RMS amplitude map of volume ±10 ms TWT around Intra Pleistocene 2 displaying bright spots in yellow and red. Intersection A-A' is displayed in Figure 4.14 and intersection B-B' is displayed in Figure 4.17.

Amplitude anomaly 12 also occurs at the Intra Pleistocene 2 reflector (Figure 4.16 and Figure 4.17). It extends 2.9 km in NE-SW and 1.7 km in NW-SE direction covering an area of 3.5 km^2. The anomaly displays strong amplitudes of negative polarity. Amplitude anomaly 12 and 13 along with several smaller anomalies are located above anomaly 9 and are interconnected to anomaly 9 with fluid flow pathways.

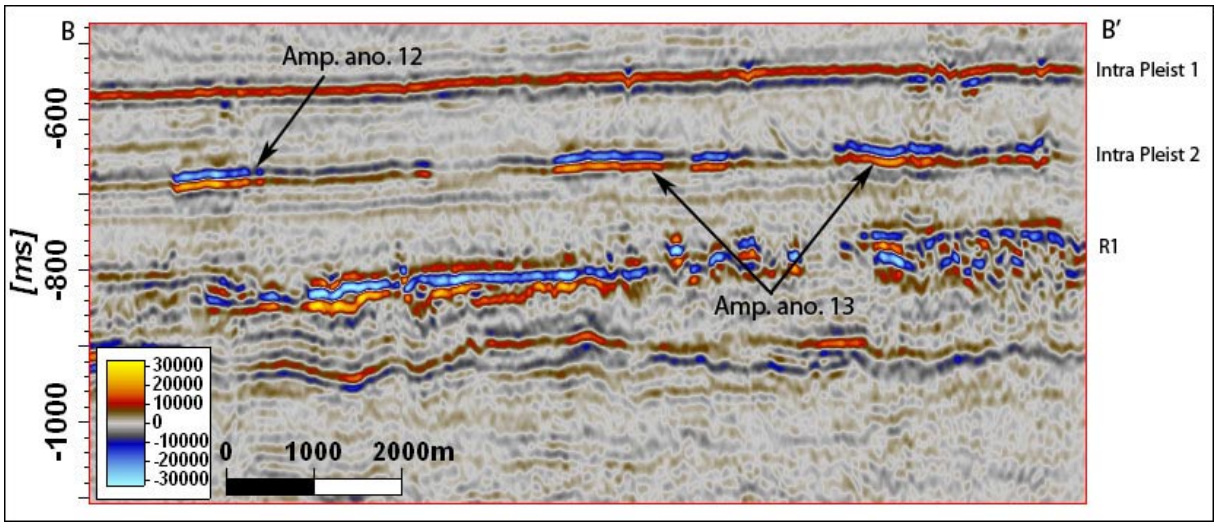

Figure 4.17. Amplitude anomaly 12 and 13 displayed in a seismic intersection. Location of intersection (B-B') and anomalies displayed in Figure 4.16.

Amplitude anomaly 13 (Figure 4.16 and Figure 4.17) is very similar to other amplitude anomalies found at the Intra Pleistocene 1 and 2 reflections. It is located in the SE corner of

the survey between inline 200-530, crossline 2550-3170 at 625-675 ms TWT (Figure 4.16). Its extent is 8 km in NW-SE and 4.5 km in NE-SW direction covering an area of 12.2 km^2. It displays strong amplitudes with an apparent negative polarity. Reflections underneath the anomaly are distorted and of lower frequency.

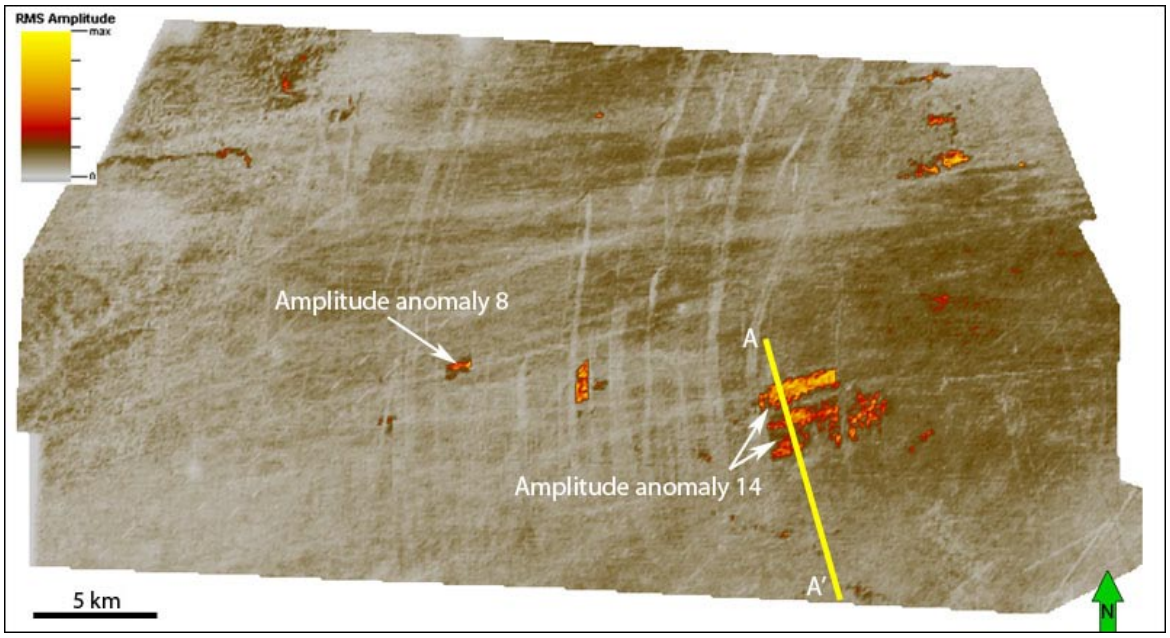

Figure 4.18. RMS amplitude map of volume ±10 ms TWT around Intra Pleistocene 1 displaying bright spots in yellow and red. Intersection A-A' is displayed in Figure 4.19.

Amplitude anomaly 14 (Figure 4.18 and Figure 4.19) occurs at the Intra Pleistocene 1 reflector and is at the same level as amplitude anomaly 8 described previously. It extends 4.9 km in E-W, 3.3 km in N-S direction and covers a total area of 8.5 km^2. Reflections beneath the anomaly display vertical zones of distorted reflections, scattered high amplitudes and low frequencies. Vertical zones of distorted reflections connect it to amplitude anomaly 1 almost 700 ms TWT further down (Figure 4.3). Amplitude anomaly 14 is connected to anomaly 1 and anomaly 9 with fluid flow pathways (section 4.3).

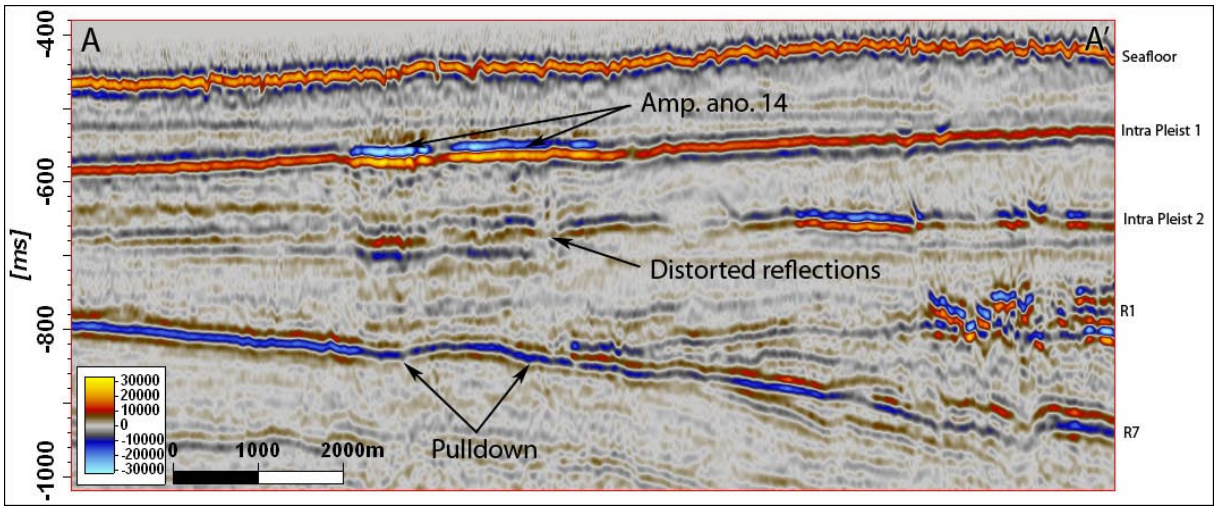

Figure 4.19. Amplitude anomaly 14 in seismic intersection. Notice possible pull-down and distorted reflections underneath the anomaly. Location of intersection and anomaly shown in Figure 4.18.

The reflection from the Intra Pleistocene 1 reflector has an overall positive polarity. Amplitude anomaly 14 is clearly much stronger then the surrounding reflection and has its highest amplitudes in the negative range. The polarity of amplitude anomaly 14 is interpreted as negative but with a stronger lower positive peak of the wavelet (Figure 4.20).

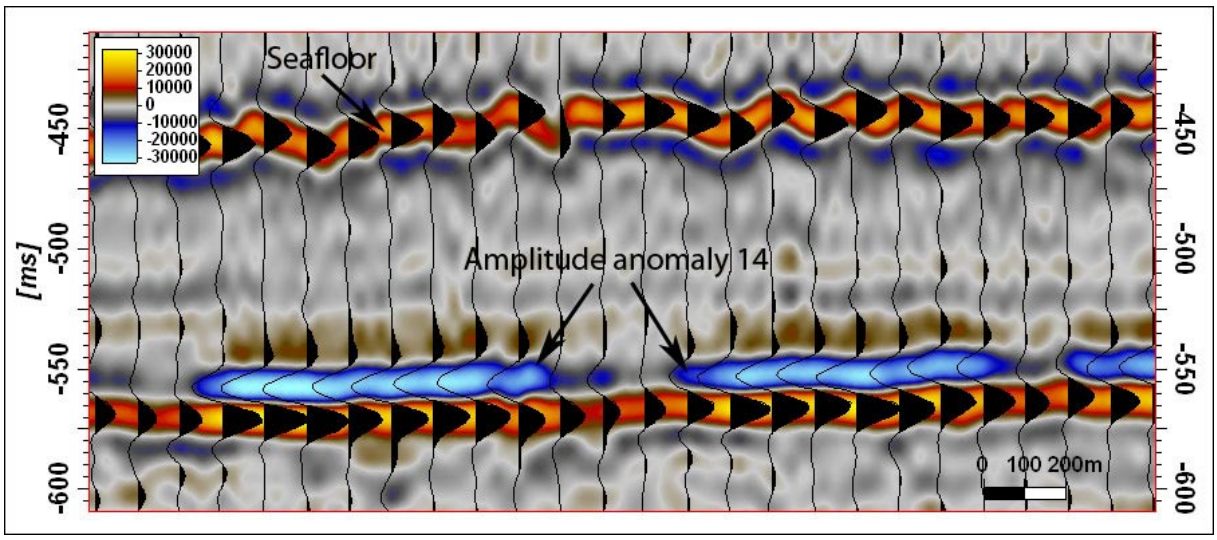

Figure 4.20. Wiggle traces shown on top of seismic of amplitude anomaly 14 and the seafloor reflection.

Table 4.1. Summary of amplitude anomalies 1 to 14.

Amp. Ano. #	Inline	Xline	Extent	Depth [ms TWT]	Area	Phase	Occurs in strata of age:
1	550-920	2865-3060	4.6 km SSW-NNE 930 m WNW-ESE	1268-1510	2.5 km^2	Negative top, positive bottom	L. Paleocene-E. Eocene
2	850-1110	3080-3470	4.2 km E-W 2.2 km N-S	1176-1486	6.4 km^2	Negative top, positive bottom	L. Paleocene-E. Eocene
3	UTM coordinate: X 617121.6 to 671271.6 and Y 7982205.3 to 8022505.3		54 km E-W 36 km N-S	625-1535	790 km^2	Negative	E. Eocene
4	680-1410	388-870	9.5 km NE-SW 4.5 km NW-SE	600-645	27.5 km^2	Unclear	Pleistocene
5	750-1100	590-780	1.9 km E-W 4.3 km N-S	1025-1110	4.5 km^2	Negative	Plio-Pleistocene
6	640-1960	1130-1650	17 km N-S 1.7 + 1.5 km E-W	867-977	26 km^2	Negative	Plio-Pleistocene
7	660-1080	1350-1850	6.1 km E-W 5.2 km N-S	710-760	16.5 km^2	Negative	Pleistocene
8	860-940	1735-1825	970 m E-W 440 m N-S	565-600	0.3 km^2	Negative	Pleistocene
9	200-1100	1500-3250	15 km NW-SE 5 km SW-NE	800-970	36 km^2	Negative (varying)	Plio-Pleistocene
10	1360-1880	1500-2360	12 km NE-SW 3.1 km NW-SE	810-1105	17.7 km^2	Negative (varying)	Plio-Pleistocene
11	1628-1795	1190-1510	3.8 km E-W 1.8 km N-S	760-800	4.6 km^2	Negative	Pleistocene
12	540-730	2330-2670	2.9 km NE-SW 1.7 km NW-SE	660-695	3.5 km^2	Negative	Pleistocene
13	200-530	2550-3170	8 km NW-SE 4.5 km NE-SW	625-675	12.2 km^2	Negative	Pleistocene
14	660-950	2720-3130	4.9 km E-W 3.3 km N-S	540-585	8.5 km^2	Negative	Pleistocene

4.3 Fluid flow expressions

Fluid flow expressions are mapped as they resemble hydrocarbon leakage pathways previously described from other areas (Heggland, 1997, 1998; Bünz et al., 2003; Berndt, 2005; Hansen et al., 2005; Ligtenberg, 2005; Gay et al., 2006; Cartwright et al., 2007).

Mapped fluid flow expressions appear in the form of vertical zones of distorted reflections **(**Figure 4.23, Figure 4.24, Figure 4.26, Figure 4.28, Figure 4.29 and Figure 4.30). Brightspots may occur at their upper terminations and scattered along the vertical extent of the feature. Beneath acoustic masking and chaotic reflections appear to be characteristic acoustic phenomena. Focused fluid flow expressions are generally much smaller in extent (m^2) then the high amplitude anomalies (km^2).

Focused fluid flow expressions were divided into 7 groups. The divisions depend on probable level of origination and level of termination. The 7 groups have been color-coded from purple to red (Figure 4.21). Examples are given for these fluid flow expressions and will be described in this chapter. The remainder can be found in the appendix.

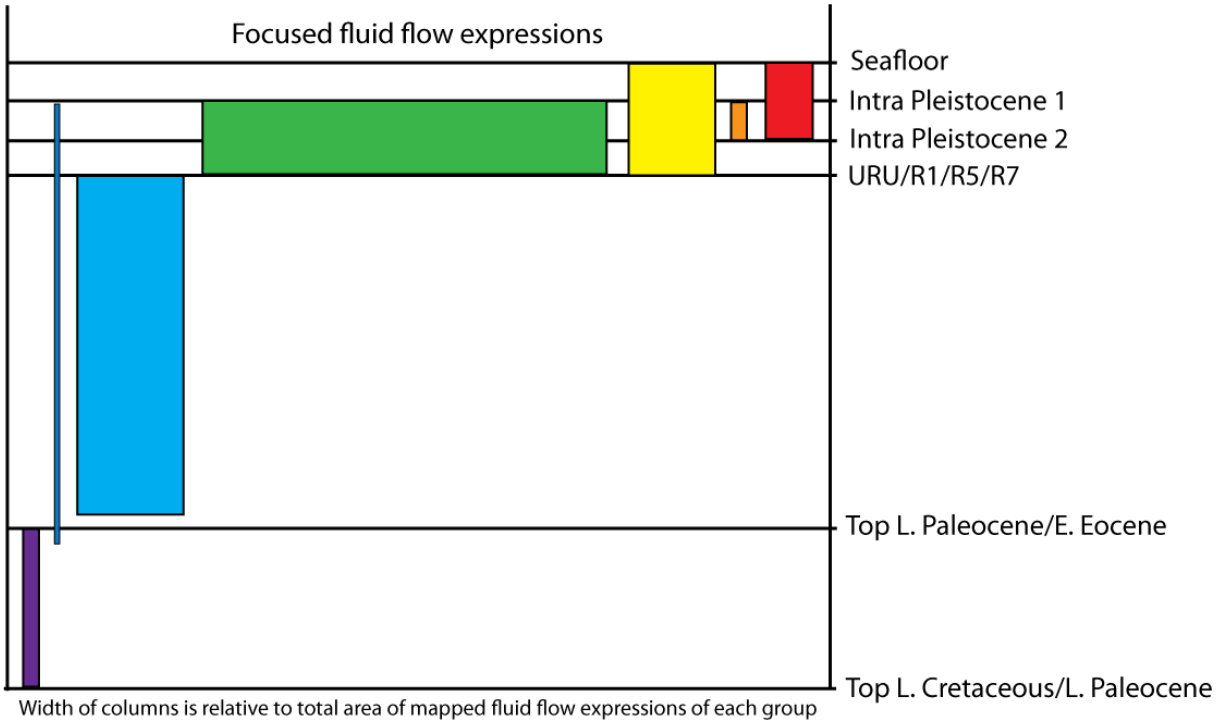

Figure 4.21. The vertical zones fluid flow expressions have been divided into 7 groups and the groups have been color-coded (left to right: purple, dark blue, light blue, green, yellow, orange and red). The width of the columns is relative to total area of mapped fluid flow expressions of each group.

Spatial distributions of focused fluid flow expressions do not appear to be random. Deeper features (purple, dark blue and light blue) concentrate in the SE section of the survey above amplitude anomaly 1, 2 and 3 and high amplitudes of the top Early Cretaceous and top Late

Cretaceous-Late Paleocene reflectors. Shallower features (green, yellow, orange and red) are distributed within or above firstly sediments of the Plio-Pleistocene wedge (GI-GII), and secondly in the NE section of the survey (Figure 4.22).

Focused fluid flow expressions presented in the results chapter are 1-6, 11-12, 15, 20, 22, 24-26 and 30. See also appendix.

Feature #	Width Inline [m]	Width Xline [m]	Area [m2]	Vertical extent [ms TWT]
1	120	300	28274,3	290
2	750	200	117809,7	275
3	200	300	47123,9	710
4	200	400	62831,9	600
5	250	300	58904,9	310
6	100	400	31415,9	610
7	350	700	192422,5	525
8	800	1000	628318,5	560
9	600	500	235619,4	210
10	490	250	96211,3	235
11	430	250	84430,3	260
12	290	200	45553,1	310
13	240	350	65973,4	260
14	150	200	23561,9	235
15	660	430	222896,0	130
16	230	200	36128,3	110
17	1900	900	1343030,9	105
18	200	700	109955,7	230
19	150	1000	117809,7	270
20	1100	450	388772,1	120
21	550	2000	863938,0	110
22	350	180	49480,1	120
23	400	100	31415,9	100
24	450	300	106028,8	280
25	250	300	58904,9	380
26	1000	800	628318,5	340
27	250	200	39269,9	110
28	300	200	47123,9	110
29	150	500	58904,9	120
30	850	650	433932,5	280
Total			6254361,2	

Table 4.2. Compilation of focused fluid flow expressions, referred to as feature 1-30, along with areal extent calculated as a simple ellipse.

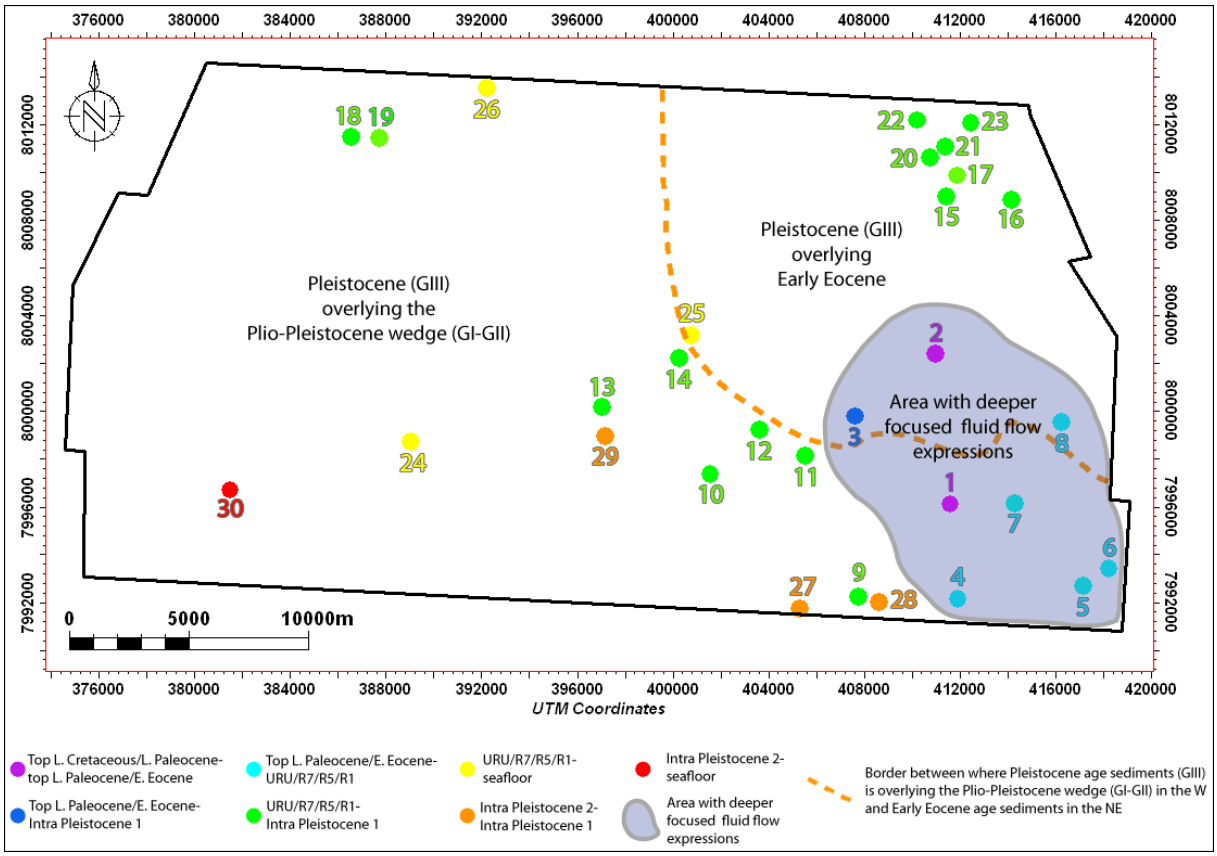

Figure 4.22. Overview of locations of fluid flow expressions (features 1 to 30). Black outline is the border of the 3D survey EL0001. The dashed orange line marks the approximate boundary between where the Plio-Pleistocene succession (GIII) is overlying the Plio-Pleistocene wedge in the SW and the Early Eocene sediments in the NE. Notice that all fluid flow expressions originating at levels below the URU to R7 is located in the SE corner of the survey.

4.3.1 Top Late Cretaceous/Late Paleocene to Top Late Paleocene/E. Eocene (Purple)

Two focused fluid flow expressions originate at the deeper section. *Feature 1* (Figure 4.23) has a small area and a vertical extent of 290 ms TWT. It resembles a pipe-shaped vertical high amplitude zone featuring stacked bright spots aligned along a NNE-SSW trending fault plane (Figure 4.23). The throw of the fault is only 20-25 ms but it can be traced from Top Late Cretaceous/Late Paleocene to Early Eocene age. Therefore, the vertical extent reaches 800 ms TWT. The fault originates directly above a large west dipping normal fault within Cretaceous sediments.

Feature 2 has a four times larger area than feature 1 and a vertical extent of 275 ms TWT. The feature has an irregular cloud-shape and its reflections display reduced continuity and frequency. Stacked bright spots occur along its edges. The root of the feature coincides with a Cretaceous normal fault and onlap reflections within the Late Cretaceous/Late Paleocene succession. The feature terminates at Amplitude anomaly 2 (Figure 4.23).

4.3.2 Top Late Paleocene/E. Eocene to Intra Pleistocene 1 (Dark blue)

Feature 3 (Figure 4.3 and location in Figure 4.25) is pipe-shaped and has a vertical extent of 710 ms TWT and a small area (Table 4.2). It originates at the apex of amplitude anomaly 1 and it terminates at the large amplitude anomaly 14 (8.5 km^2) at Intra Pleistocene 1. The feature is associated with a NNE-SSW trending fault with approximately 15 ms throw (Figure 4.3). Reflections display a vertical dim zone below the URU and stacked bright spots above the URU reflector. A pull-down of reflections characterizes the entire vertical extent, but with weaker effect in the deeper part and stronger effect in the shallower part.

4.3.3 Top Late Paleocene/E. Eocene to URU/R7/R5/R1 (Light blue)

Five focused fluid flow expressions originate from amplitude anomaly 3. Figure 4.24 displays their locations in a RMS amplitude map and a seismic section.

Feature 4 has a vertical extent of 600 ms TWT between amplitude anomaly 3 in Early Eocene sediments and the R7 reflector at bottom Plio-Pleistocene. The feature follows a fault with a small throw. Flags are visible along the fault as well as larger high amplitude anomalies. *Feature 5* shows a vertical extent of 310 ms TWT, from amplitude anomaly 3 in Early Eocene sediments to approximately R7. A minor throw exist that suggest a fault below the seismic resolution. Amplitude anomalies show stacked bright spots in variable intensity and variable extent.

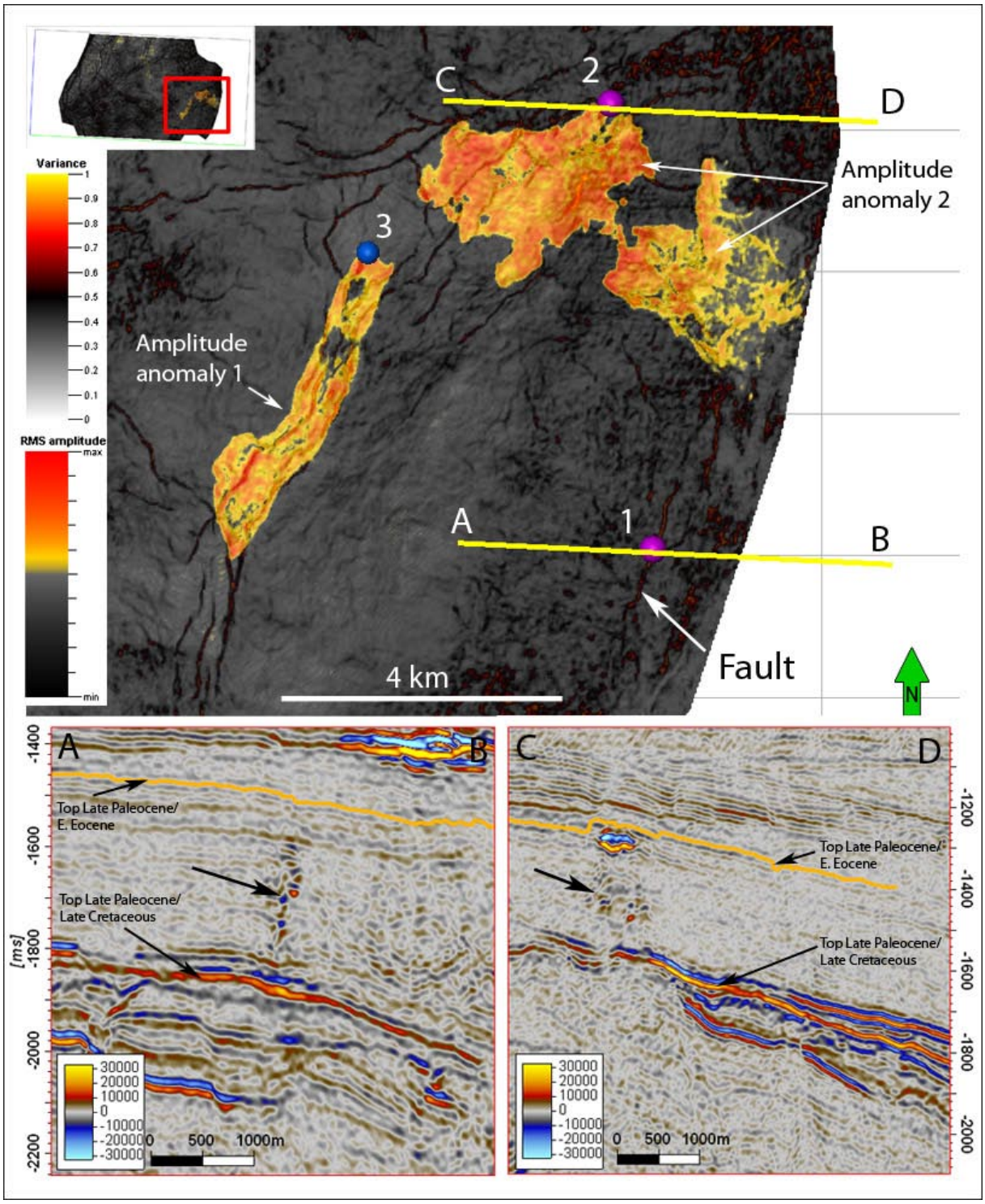

Figure 4.23. Top displays a RMS amplitude map (0-+50 ms TWT from Top Late Paleocene/E. Eocene horizon, orange in seismic intersections) and a variance map with 70% transparency (± 5ms from Top Late Paleocene/E. Eocene horizon) displayed on the Top Late Paleocene/E. Eocene horizon. Yellow lines mark the two seismic sections and dots mark the location of the focused fluid flow features 1, 2 and 3. Notice the high amplitudes of the reflection these vertical disturbances originate from, the Top Late Paleocene/Late Cretaceous reflector.

Feature 6 extends 610 ms TWT from the Early Eocene amplitude anomaly 3 to the R7 reflector. The vertical fluid flow expression is associated with a N-S trending fault that shows

approximately 20 ms throw. Associated amplitude anomalies are predominantly flags on the sides of the fault. The acoustic masking zone is very small. The underlying reflection, which is amplitude anomaly 3, displays a pull-down.

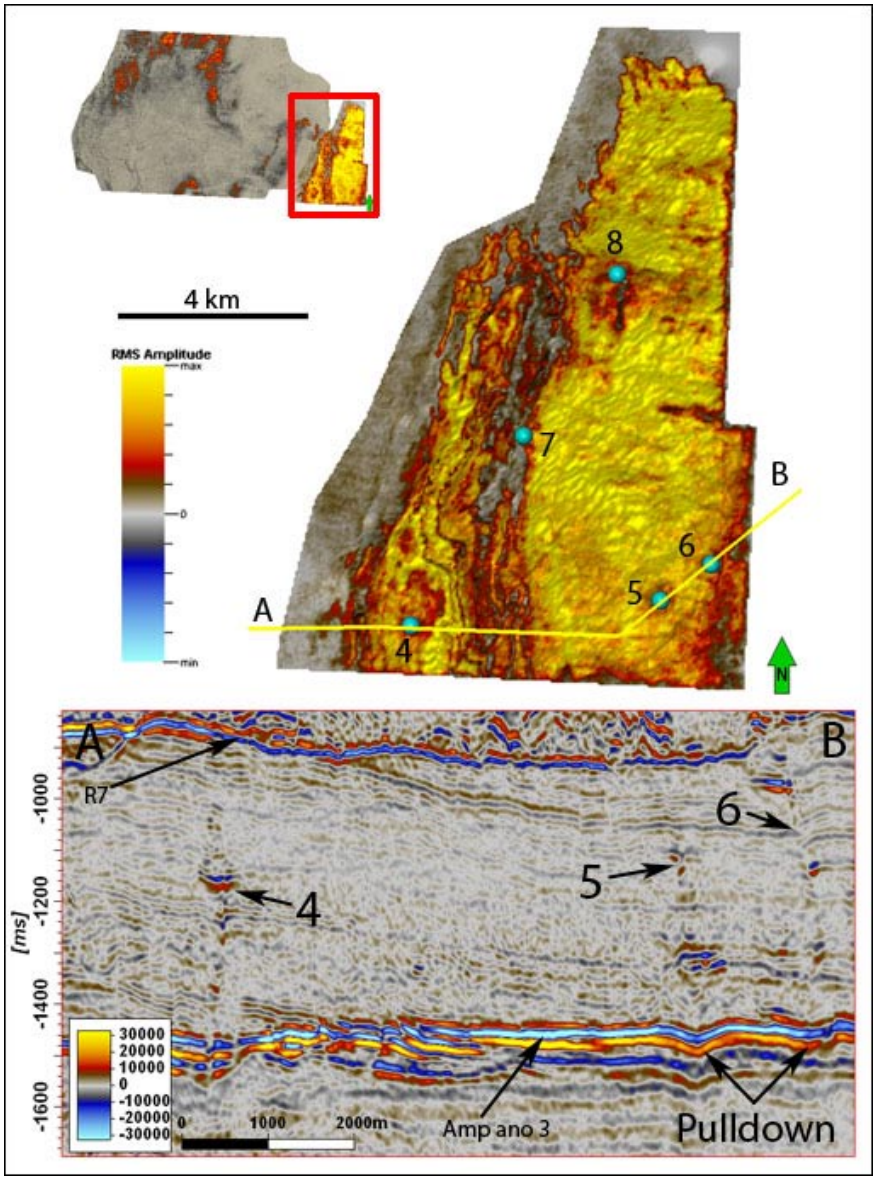

Figure 4.24. Top displays RMS amplitude map of amplitude anomaly 3 with 5 vertical zones of distorted reflections indicated with light blue dots. Bottom is a seismic section from A-B displaying feature 4, 5 and 6 with vertical zones of high amplitude anomalies.

Figure 4.25 and Figure 4.27 show the spatial distribution of the mapped fluid flow expressions in Plio-Pleistocene sediments (GI-GIII). The distribution indicates a not randomly and localized concentration of features over the Plio-Pleistocene wedge at the NE corner. At this area the URU shoals and coincides with the Intra Pleistocene 2 reflection.

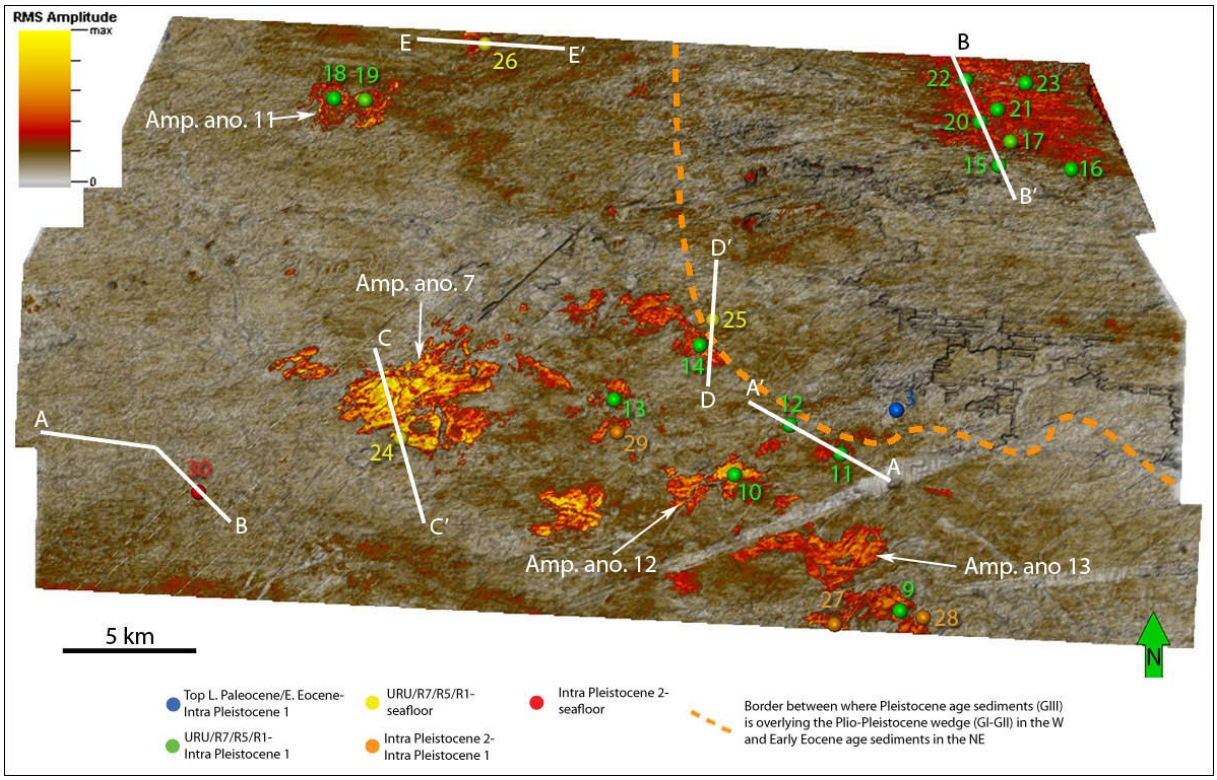

Figure 4.25. Top RMS amplitude map of volume ±10 ms TWT around Intra Pleistocene 2 showing bright spots in yellow and red colors and vertical fluid flow expressions as green, yellow, orange and red dots depending on which vertical extent they have. Six sections; A-A' (Figure 4.26), B-B' (Figure 4.26), C-C' (Figure 4.28), D-D' (Figure 4.29), E-E' (Figure 4.30) and A-B (Figure 4.32), are indicated. The dashed orange line marks the approximate boundary between where the Plio-Pleistocene succession (GIII) is overlying the Plio-Pleistocene wedge (GI-GII) in the SW and the Early Eocene sediments in the NE.

4.3.4 Between URU (URU/R1/R5/R7) and Intra Pleistocene 1 (Green)

A total of 15 features have been mapped at this level. The distribution of fluid flow expressions, who originate, terminate or pass through the reflectors, display a close relationship with the locations of bright spots located at Intra Pleistocene 2 reflector (Figure 4.25 and Figure 4.27). 86% (19 out of 22) of the vertical zones of distorted reflections pass directly through bright spots at the level of Intra Pleistocene 2 reflector. The relationship is less clear at Intra Pleistocene 1 level where 59% (13 out of 22) of the vertical zones are located in the immediate vicinity or within a bright spot. Six seismic intersections (represented by white lines in Figure 4.25 and Figure 4.27) provide a representative selection of vertical fluid migration pathways. Two of seismic intersections show vertical zones of disturbed reflections from the URU/R1/R5/R7 to Intra Pleistocene 1 interval (green dots).

Seismic intersection A-A' (Figure 4.26) displays two vertical fluid flow expressions, features 11 and 12. *Feature 11* has a vertical extent of 260 ms TWT. The shape shows an irregular column. *Feature 12* has a vertical extent of 310 ms and has the shape of an irregular column.

Features 11 and 12 are quite similar; both originate at R1/URU and terminate at Intra Pleistocene 1. Both are associated with a large bright spot at Intra Pleistocene 1 Level (Figure 4.27). Feature 11 is also associated with a bright spot at Intra Pleistocene 2 level. Both features (11 and 12) display reflections of decreased continuity, frequency and amplitude, and also display pull-down effects of reflections.

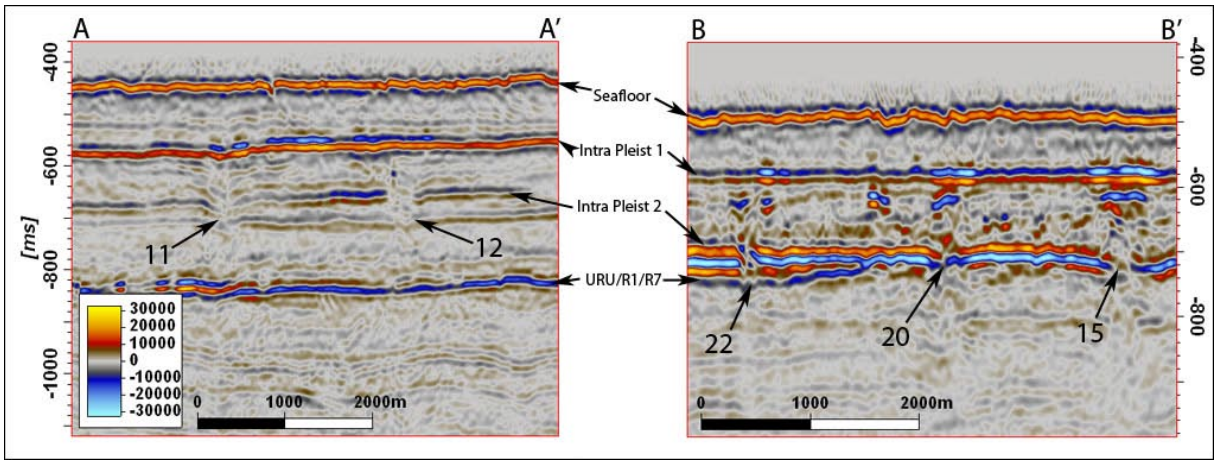

Figure 4.26. Seismic sections A-A' (left) and B-B' (right) as seen in Figure 4.25 and Figure 4.27 display feature 11 and 12, and 15, 20 and 22 respectively. Locations of seismic intersections is shown in Figure 4.25 and Figure 4.27.

Feature 15, 20 and 22 (located in the NE corner of the survey) occur in an area with frequent distortions of reflections. Only the most distinct features were chosen and sizes were determined. The URU is at its shallowest in the survey and it coincides with the Intra Pleistocene 2 reflector. The interference between the URU and the Intra Pleistocene 2 causes a bright spot in the NE corner of the survey (Figure 4.25).

Feature 15 has a vertical extent of 130 ms TWT, and an irregular shape. It is a large feature (area of 222900 m^2) and it is associated with bright spots both at the URU and the Intra Pleistocene 1 reflection (Figure 4.26). A vertical high amplitude low continuity zone with pull-down effects and a weakened URU reflection marks feature 15.

Feature 20 extends 120 ms from the URU to Intra Pleistocene 1. It is also a large feature covering an area of 388700 m^2 and it shows an irregular shape. Feature 20 is associated with bright spots at Intra Pleistocene 1 and URU/Intra Pleistocene 2. A dim spot on the URU reflection occurs directly beneath the feature. The feature exhibits stacked bright spots in a low frequency zone.

Feature 22 has a vertical extent of 120 ms from URU/Intra Pleistocene 2 to Intra Pleistocene 1. It has irregular column shape. Bright spots appear at both URU/Intra Pleistocene 2 and Intra Pleistocene 1 and the feature exhibits stacked bright spots and a random pattern.

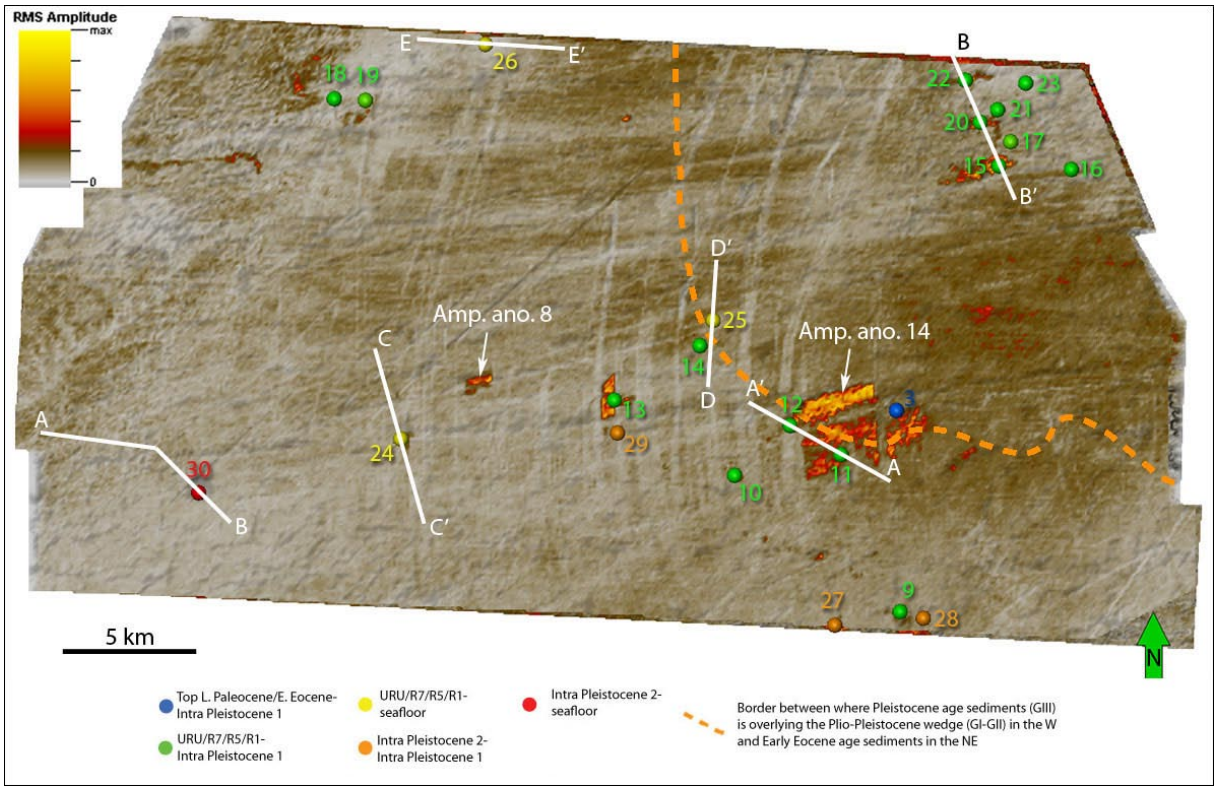

Figure 4.27. RMS amplitude map of volume ± 10 ms around Intra Pleistocene 1 reflector displaying bright spots in yellow and red colors and vertical fluid flow expressions as green, yellow, orange and red dots depending on which vertical extent they have. Six sections; A-A' (Figure 4.26), B-B' (Figure 4.26), C-C' (Figure 4.28), D-D' (Figure 4.29), E-E' (Figure 4.30) and A-B (Figure 4.32), are indicated. The dashed orange line marks the approximate boundary between where the Plio-Pleistocene succession (GIII) is overlying the Plio-Pleistocene wedge (GI-GII) in the SW and the Early Eocene sediments in the NE.

4.3.5 URU/R1/R5/R7 to Seafloor (Yellow)

Three features (24, 25 and 26) that extend from URU/R1/R5/R7 to the seafloor were determined and mapped in detail (Feature 24, seismic section C-C' (Figure 4.28); Feature 25, seismic section D-D' and Feature 26, seismic section E-E').

Feature 24 has its root at reflector R5 and a total vertical extent of 280 ms. Its root is at a mass movement deposit and the top Plio-Pleistocene wedge toplap unconformity. It is associated with amplitude anomaly 6 at R1 level, amplitude anomaly 7 at Intra Pleistocene 2 and amplitude anomaly 8 at Intra Pleistocene 1. The feature exhibits a vertical low continuity, low frequency zone with pull-down effect of reflections.

The base of *Feature 25* is difficult to determine due to acoustic masking but the shallowest level appears to be the URU. The feature extends 380 ms from URU to the seafloor and it has the shape of a pipe. A negative polarity marks the bright spot at the URU. Its root is located in the vicinity of the eastwards termination of Plio-Pleistocene wedge. This pipe feature is the one with a classical appearance if compared to previously described pipes (e.g. Hustoft et al., 2007), as a vertical wipeout zone. However it is not associated with a morphological

expression of a pockmark, given the seismic resolution, on the seafloor. On the other hand, very weak amplitudes mark a circular shape in a RMS amplitude map of the seafloor. The location of the feature's termination appears to be unaffected by large seafloor ploughmarks.

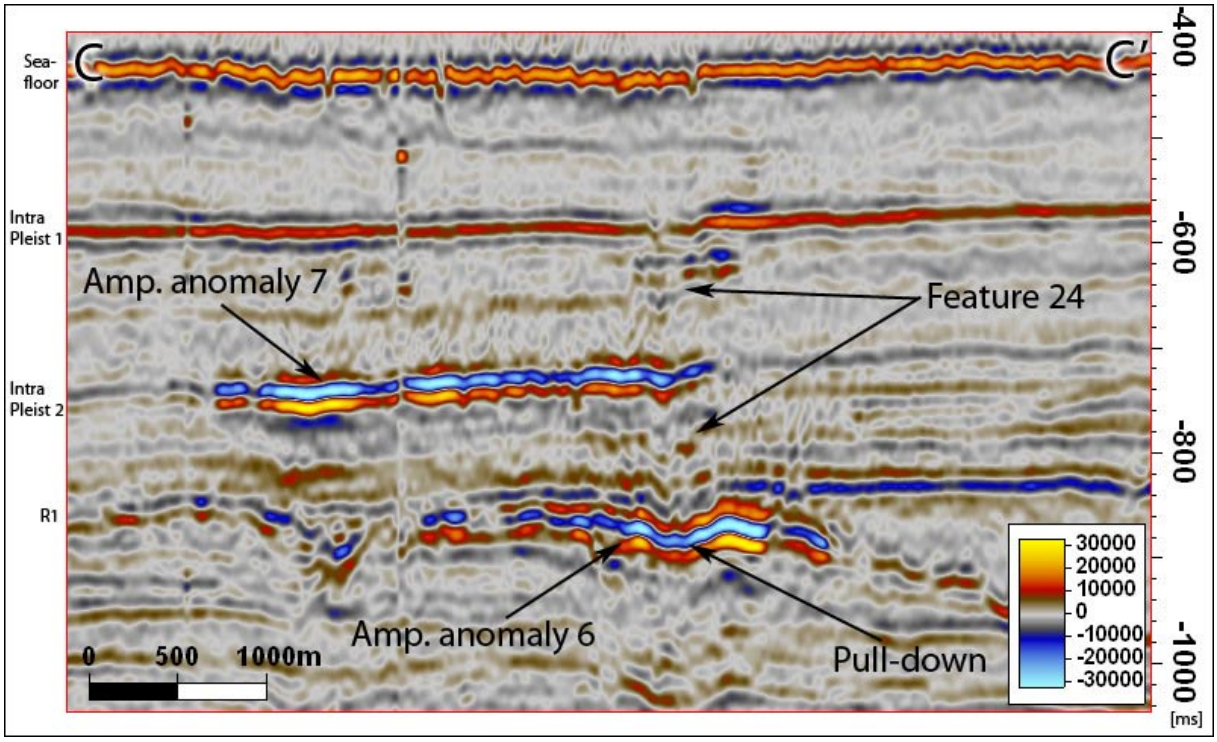

Figure 4.28. Seismic section C-C' displaying feature 24 with associated pull-down at amplitude anomaly 3 and slight pull-down at amplitude anomaly 4. Location of seismic intersection is shown in Figure 4.25 and Figure 4.27.

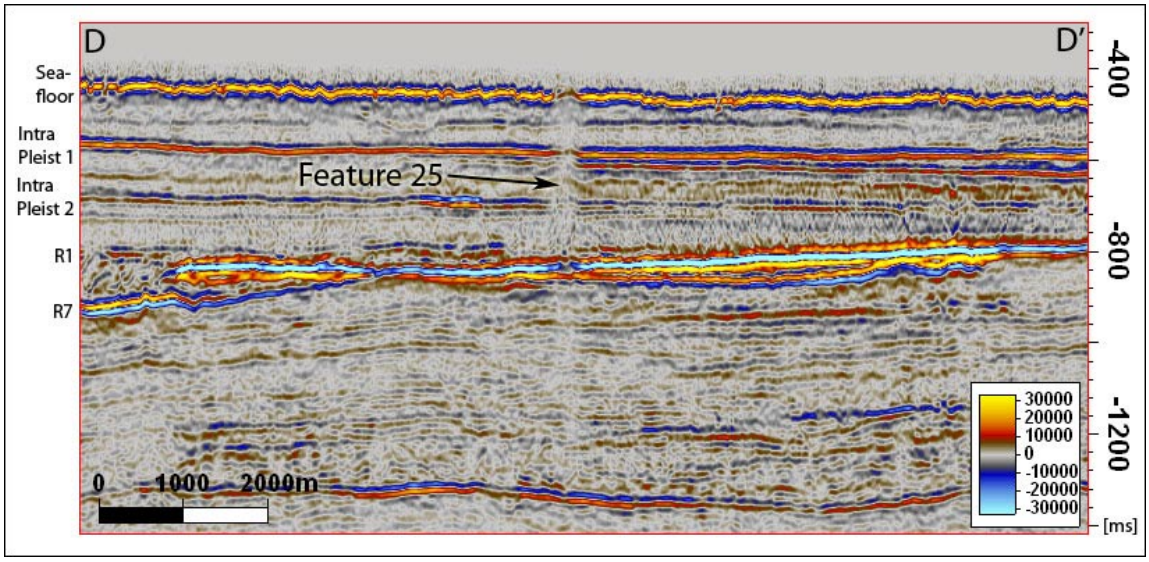

Figure 4.29. Seismic section D-D' displaying feature 25 is associated with a large bright spot at the R1/URU reflection. Reflections within the feature display low amplitudes and slight pull-up. Location of seismic intersection is shown in Figure 4.25 and Figure 4.27.

Feature 26 has a vertical extent of 340 ms from reflector R1 to the seafloor. It is a very large feature, covering an area of 628300 m^2. It is likely to be even larger as it is at the edge of the survey. The shape shows an irregular chimney associated with stacked bright spots that occur mainly on the western side of the feature. The root of the feature appears to be at mass movement deposits and at the R1 reflector. All bright spots display a negative polarity and a circular low amplitude area directly above the feature on the seafloor.

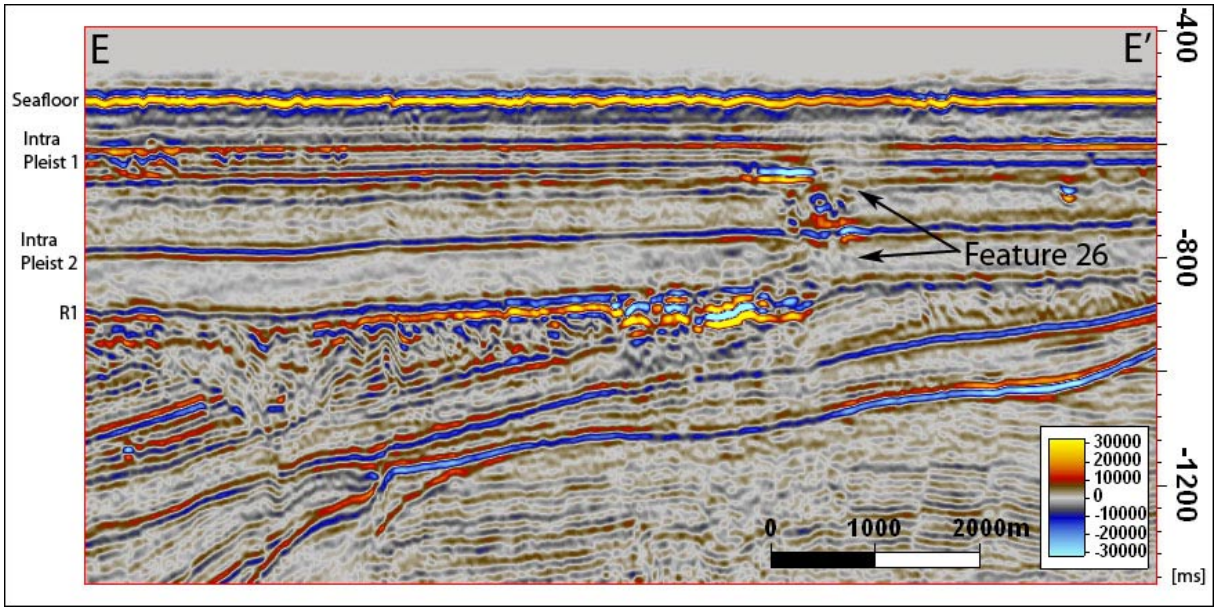

Figure 4.30. Seismic section E-E' displaying feature 26 with associated bright spots at R1, Intra Pleistocene 2 and stacked bright spots west of the low amplitude zone. Location of seismic intersection is shown in Figure 4.25 and Figure 4.27.

Feature 30 (Figure 4.32) extends 280 ms TWT from the R1 reflector to the seafloor. It is also a very large feature (area of 433900 m^2) and the shape of a chimney that becomes wider towards shallower depths. It is associated with a dim zone and a large pockmark at the seafloor. Reflections within the dim zone display pull-down effects, either as an acoustic effect or an actual structural deformation.

4.4 Circular and sub-circular seafloor depressions

The seafloor of the Barents Sea is heavily shaped by glacial erosion which in turn is exemplified by numerous ploughmarks (e.g. Andreassen et al., 2008). The dense distribution of ploughmarks makes recognizing pockmarks a difficult task. Ploughmarks are typically 100–300 m wide, with a relief of 3–10 m (Andreassen et al., 2008). Normal pockmarks are 10-700 m wide and up to 45 m deep, but giant pockmarks may reach more than a kilometer in diameter (Hovland et al., 2002).

A total of 22 depressions were identified that represent possible pockmarks (Figure 4.31, Table 4.3). The depressions show large diameters, the smallest depression being 460x420 m and the largest 1050x970 m in size. They are approximately 4 m to 23 m deep. A number of pockmarks are most likely too small to be identified on the seismic data. The spatial distribution of pockmarks appears to be random but a slight emphasis on the western section of the survey cannot be ruled out. Here we found a concentration of 2/3 of the pockmarks.

Table 4.3. Depressions (n=22) identified as possible pockmarks

Depression No.	Inline	Cross-line	Longest axis	Shortest axis	Area [km3]	Azimuth of longest axis	Depth of depression [ms TWT]	Depth of depression [m] (1480m/s)	Depth to bottom of depression [ms TWT]	Depth to bottom of depression [m] (1480m/s)
1	536	968	1050	950	0,783	55	31	22,9	457	338,2
2	646	568	850	700	0,467	110	12	8,9	437	323,4
3	654	1208	1000	850	0,668	65	12	8,9	444	328,6
4	662	808	1050	970	0,800	85	19	14,1	438	324,1
5	686	2618	590	540	0,250	55	5	3,7	435	321,9
6	690	1538	740	640	0,372	55	10	7,4	438	324,1
7	850	1818	640	540	0,271	60	10	7,4	441	326,3
8	858	2578	870	670	0,458	160	7	5,2	446	330,0
9	1046	3602	670	650	0,342	45	10	7,4	450	333,0
10	1050	2378	670	580	0,305	130	8	5,9	456	337,4
11	1066	498	760	680	0,406	40	9	6,7	459	339,7
12	1182	1868	580	540	0,246	50	11	8,1	448	331,5
13	1250	618	460	420	0,152	55	10	7,4	470	347,8
14	1258	1508	690	510	0,276	45	9	6,7	457	338,2
15	1258	1658	660	480	0,249	20	11	8,1	452	334,5
16	1430	3420	560	540	0,238	43	8	5,9	476	352,2
17	1446	3544	580	460	0,210	90	10	7,4	487	360,4
18	1498	1578	520	560	0,229	20	11	8,1	463	342,6
19	1598	3348	930	900	0,657	50	13	9,6	491	363,3
20	1622	1208	980	940	0,724	145	13	9,6	502	371,5
21	1810	818	710	570	0,318	100	7	5,2	520	384,8
22	1862	2458	810	750	0,477	90	16	11,8	597	441,8

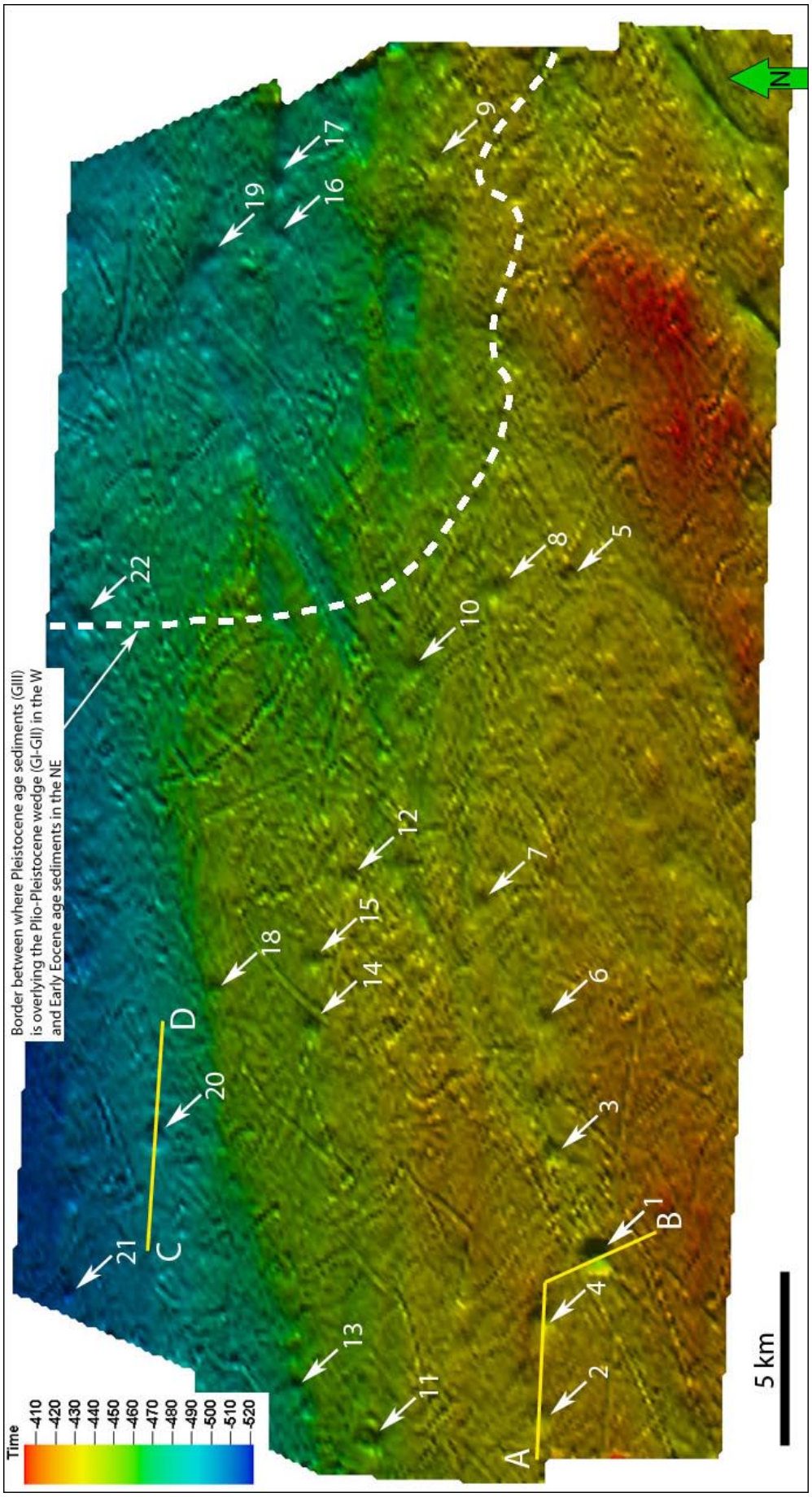

Figure 4.31. Twenty two circular and sub-circular depressions on the seafloor. Surface map results from interpretation of upper zero crossing of the seafloor reflection (low resolution 120x120 grid, 20x vertical exaggeration). The dashed white line marks the approximate boundary between where the Plio-Pleistocene succession (GIII) is overlying the Plio-Pleistocene wedge (GI-GII) in the SW and the Early Eocene sediments in the NE.

Two seismic intersections show examples of distinct pockmarks (Figure 4.31, Figure 4.32 and Figure 4.33). Seismic intersection A-B (Figure 4.32) marks *Depression 1* has a slightly ellipsoid shape with a length of 1050 m and a width of 950 m. The area of the depression is 0.78 km^2 and the depth 23 m. *Depression 2* has a longest axis of 850 m and a shortest axis of 700 m. The area of the depression is 0.47 km^2 and the depth 9 m. *Depression 4* has a longest axis of 1050 m and a shortest axis of 970 m. The area is 0.80 km^2 and the depth 14 m. All three depressions are slightly ellipsoid and display weaker amplitudes and lack of high frequency. Beneath Depression 1 the reflections are disturbed down to 750 ms TWT. Reflections within depression 1 may resemble sediment infill.

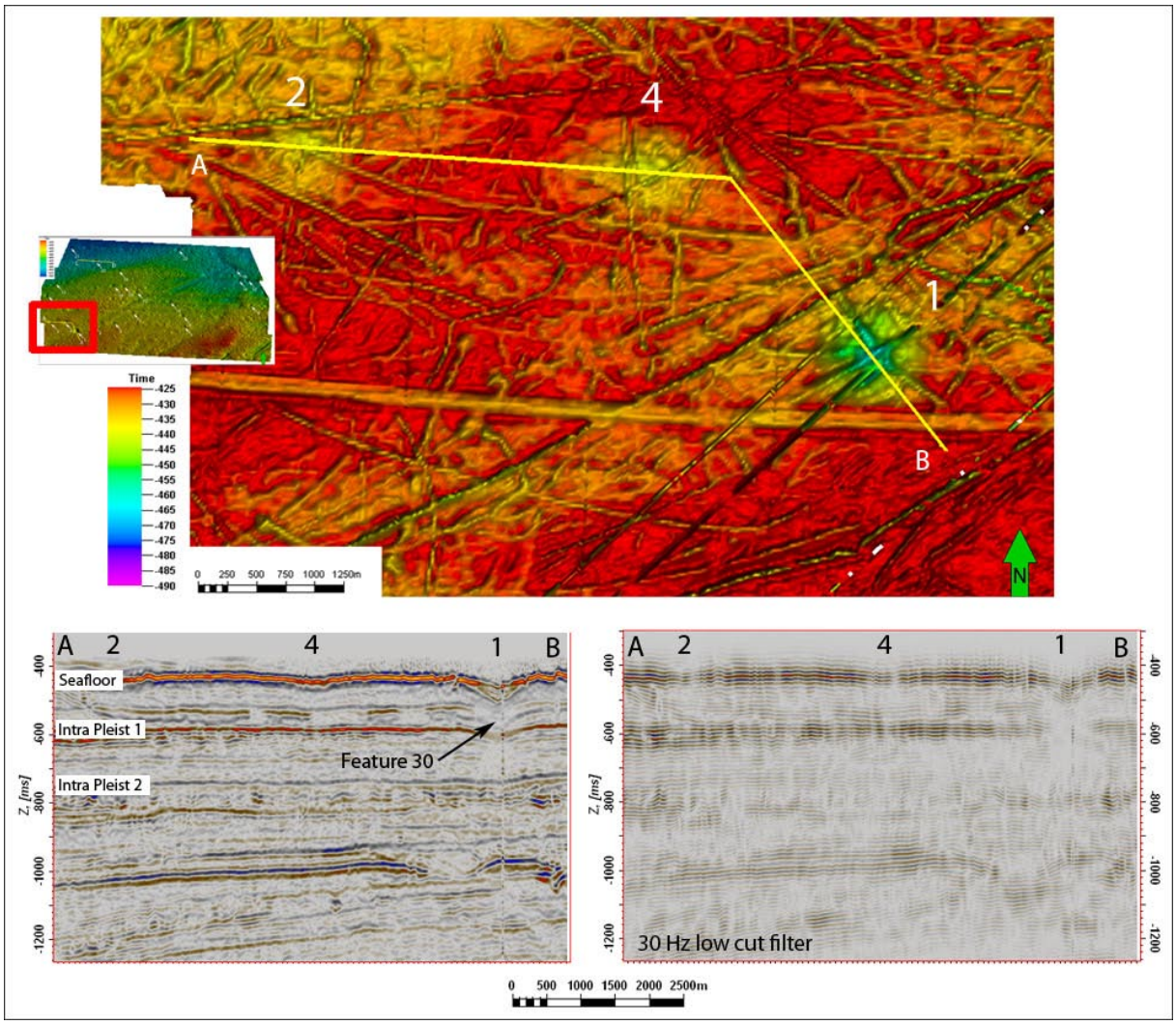

Figure 4.32. Depressions 1, 2 and 4, all three depressions display weaker amplitudes and lack of high frequency seismic energy. Note appearance of reflections underneath depression 1.

Seismic intersection C-D displays *depression 20*. It is 980x940 m in size, 13 m deep and covers an area of approximately 0.72 km^2. Beneath depression 20 several bright spots occur

that are clearly related to mass movement deposits associated with Amplitude anomaly 6. In between the amplitude anomaly and the pockmark reflections are distorted.

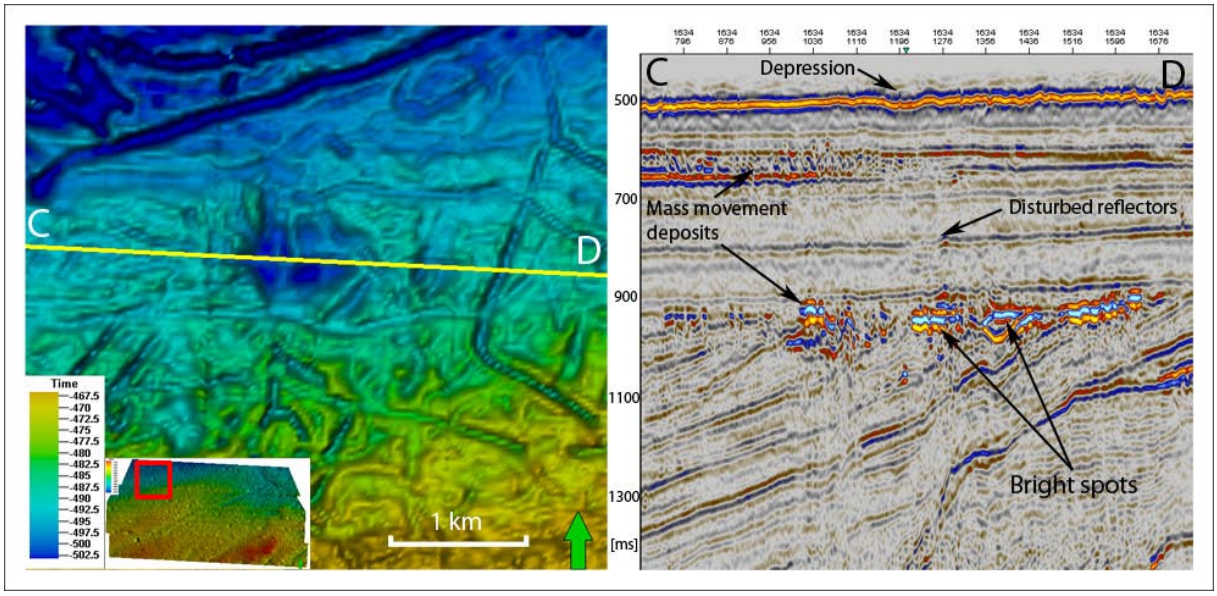

Figure 4.33. Depression 20 in the NW corner of the survey, it may appear to be associated with underlying bright spots and disturbed reflections.

5 DISCUSSION

The results chapter presented the most significant high amplitude anomalies and indicators of focused fluid flow expressions within the EL0001 survey. The discussion will now focus on deciphering the larger scale fluid migration system in Veslemøy High related to hydrocarbons. An attempt will be made to estimate fluid flow through the mapped pathways of the fluid migration system.

It will be shown that it is likely that fluids migrate into the Veslemøy High, along dipping layers, from deeper structures in the west and east, primarily from Sørvestsnaget Basin in the west and Tromsø Basin in the east.

5.1 Amplitude anomalies

The amplitude anomalies are subdivided into five categories that are presented in Table 5.1.

Table 5.1. Amplitude anomaly categories

Category	Description	Amplitude anomalies
1	Large amplitude anomaly lobes in Late Paleocene to Early Eocene sediments	1 and 2
2	Fan system	3
3	Mass movement deposits	4, 5 and 9
4	Fluid accumulations beneath and within glacial sediments	6, 7, 8, 11, 12, 13 and 14
5	Channels	10

5.1.1 Category 1 - Large amplitude anomaly lobes in Late Paleocene to Early Eocene sediments

Two very distinct amplitude anomalies (1 and 2) are located within Late Paleocene to Early Eocene sediments beneath the Top Late Paleocene to Early Eocene reflector (Figure 4.3). Nearby wells show sediments of Late Paleocene to Early Eocene age that consist of mainly fine grained marine sediments intercalated with thin siltstone and sandstone layers. While the top of the anomaly displays negative amplitudes the bottom of the anomaly displays positive amplitudes. The negative amplitudes may be indicative of a lower acoustic velocity if compared to the surrounding sediments. The area around Veslemøy High show magmatic intrusions and salt diapirs (Saettem et al., 1994; Faleide et al., 1996; Breivik et al., 1998). Both salt and magmatic intrusions have very high P-wave velocities, typically 4500-5500 m/s for salt and 4500-6000 m/s for magmatic rocks. The high acoustic velocities would result in

positive polarities compared to the seafloor reflections, which is not expressed by anomaly 1 and 2. The observed negative amplitudes appear to be bounded by faults and localized in a structural high, this indicates that they were formed after the faulting occurred thus making it less likely that it is primary sedimentary structures. Possible explanations for the very high negative amplitudes and low velocity anomalies can be gas accumulations within sediments or sand injectites with gas accumulations.

Sand injectites has been found within the Middle Eocene fan in Sørvestsnaget Basin (Ryseth et al., 2003) and may provide an explanation for the anomalies in Veslemøy High as well. A high porosity sand intrusion can have a low enough velocity to produce a negative acoustic impedance contrast (Avseth et al., 2005). However, anomaly 1 and 2 have such high amplitudes compared to surrounding reflectors that it appears unlikely that sand without gas can be the cause of it. In contrast, both high porosity sand and gas can produce very low acoustic impedance and a negative reflection coefficient, and thus a phase reversal (if compared to the seafloor reflection).

Amplitude anomaly 3 suggests a sediment fan that may consist of mass movement and channel deposits that include sand layers (discussed in section 5.1.2). Amplitude anomaly 1 and 2 are located at a deeper level (Late Paleocene to Early Eocene) than amplitude anomaly 3 (Early Eocene). If amplitude anomaly 1 and 2 are related to remobilized sands from anomaly 3 the processes would have been downward (see relative locations in Figure 4.3), which is an unlikely scenario. The source of the remobilized sands may be beneath amplitude anomaly 3, this is difficult to evaluate due to acoustic masking from amplitude anomaly 3. Amplitude anomaly 3 will be explained under Category 2 (section 5.1.2)

Overpressure within sand bodies may slow down diagenetic processes and allow sands within otherwise lithified sediments to remain unlithified (Fertl, 1976; Avseth et al., 2005). Sands may become fluidized for example due to seismicity induced liquefaction, application of tectonic stresses, excess pore fluid pressure and the influx of an over pressured fluid from deeper basins (Jolly and Lonergan, 2002). In this case the high permeability of the sandstones and the low permeabilities of overlying shales may enable high pressure to form within the sandstone that is interconnected with deeper basins in the east (Tromsø Basin). The sand may have injected as a sill, along strata until it stops against a fault or retains pressure equilibrium. However, lack of vertical injection along faults and the lack of seismic resemblance to many previously documented sand injectites (Jolly and Lonergan, 2002; Duranti and Hurst, 2004; Huuse et al., 2004) contradicts this theory.

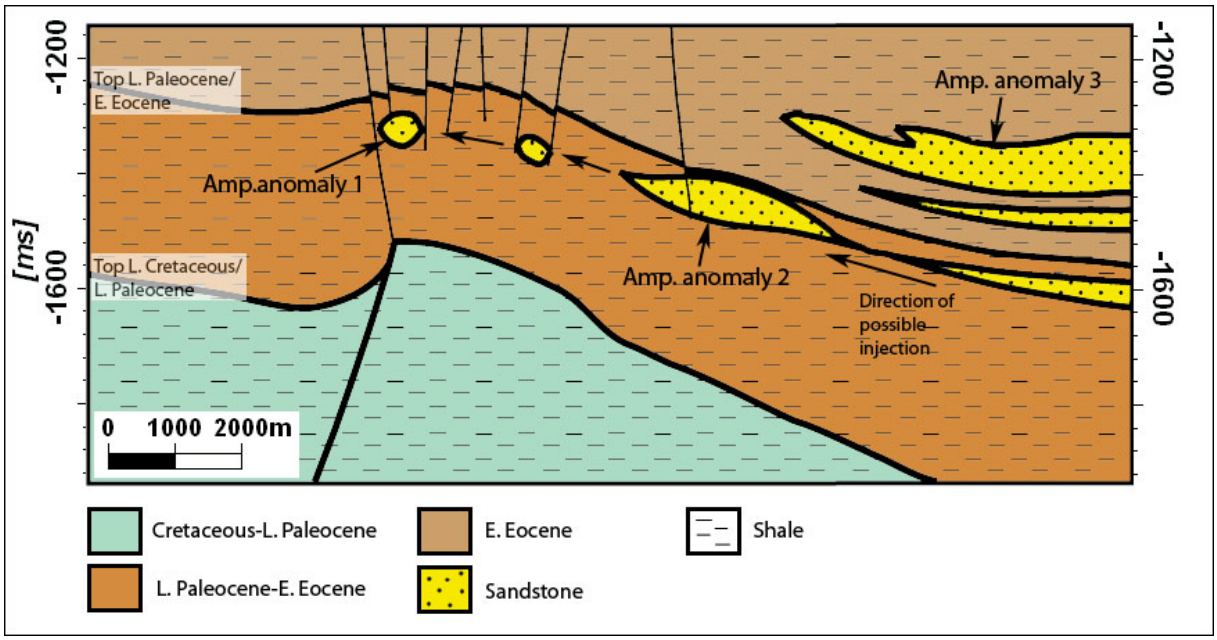

Figure 5.1. Sketch of possible sand injection interpretation of amplitude anomaly 1 and 2. Anomaly 1 and 2 may consist of sands remobilized from sands beneath anomaly 3. Direction of possible injection is indicated. Sketch made from inline 896.

Gas accumulations within sediments provide the most obvious explanation for the high amplitude anomalies. It implies that gas accumulates within shales or within silt/sandstones. Microfracturing of shales, either by tectonic activity or by over-pressurized fluids may create porosity and permeability in addition to intergranular porosity and permeability, a secondary porosity (Magara, 1986). Fluids can migrate and accumulate within the secondary porosity of shales. Due to the lack of well data in the area it cannot be ruled out that the sediments consists of higher porosity sediments (for example sand or silt) with enough pore volume and permeability to become reservoirs. Supporting this theory are observations that geophysically inferred gas accumulates at crests and apexes of structures. They appear to be bounded by impermeable faults (Figure 4.23).

5.1.2 Category 2 – Fan system

Amplitude anomaly 3 is interpreted as an Early to Mid Eocene fan formed as the Veslemøy High was uplifted and eroded concurrent with the opening of the Norwegian-Greenland Sea and associated crustal breakup (Knutsen et al., 1992). An analogue is found in Sørvestsnaget Basin, a 135 m thick sandy Middle Eocene interval suggested to be emplaced by gravity-driven deposition in a submarine fan/channel environment (Ryseth et al., 2003). East of Veslemøy High, in the Tromsø Basin, progradation of sediment deposits was at first westwards in Early Eocene, with Loppa High as a suggested source area. During Early to Mid

Eocene, progradation also had a southward and an eastward component from the Veslemøy High (Knutsen et al., 1992) which is the suggested sediment source for the fan buildup.

However, the answer to the question what causes the high amplitude reflection which constitutes amplitude anomaly 3 still remains. It has previously been suggested that it relates to a tuff/ash layer (Faleide et al., 1988). Knutsen et al. (1992) argues against this theory with three main arguments:

1. The sharp termination of the reflector towards the south is uncharacteristic of a tuff-layer which would more closely resemble a blanket on existing topography.
2. The only other tuffeous material in the area does not show a similar high amplitude seismic response (Knutsen and Vorren, 1991).
3. The closest known Tertiary volcanic activity occurred in the Vestbakken Volcanic Province (Faleide et al., 1988). This would suggest that the tuff was deposited as a long-transported, widespread ash layer and therefore be too thin (~10 cm) to produce a seismic reflection of this amplitude.

Instead Knutsen et al. (1992) suggests three other possible explanations:

A. A diagenetic transition. It has been suggested that the transition originates from opal CT to Quartz transition.
B. Gas along a lithostratigraphic boundary.
C. A condensed section.

Knutsen et al. (1992) finally concluded that a likely explanation is a combination of A and C; a diagenetic transition along a condensed surface. They argue that high biogenic activity and low clastic input led to high concentrations of silica-rich sediments along the condensed surface. However, they did not provide any arguments against the gas theory.

I would like to argue for the gas theory where gas migrates along a lithostratigraphic boundary. In this case, gas accumulates within sandstones that are related to a submarine fan/channel environment. A trap may occur that is referred to as a lateral depositional pinch-out trap (Allan et al., 2006). The argument against a condensed section is that the location occurs proximal to the slope of Veslemøy High, which was uplifted during the Early-Mid Eocene. The uplift should have increased the sediment input and not decreased it. Therefore, conditions to develop a condensed section are unfavorable. In contrast, the given arguments for gas accumulations within an Early-Mid Eocene Fan complex are:

1. A sandy section, interpreted as a submarine fan was found in Sørvestsnaget Basin, west of Veslemøy High. This fan, an "excellent reservoir" (Ryseth et al., 2003), is

water-bearing (Ryseth et al., 2003) and lacking the characteristic strong negative amplitude of amplitude anomaly 3. Amplitude anomaly 3 differs in amplitude polarity from the water-bearing sandstone in Sørvestsnaget Basin.

2. The strong negative amplitude anomaly 3 suggest a gas-filled sandstone. A positive amplitude would be expected from a diagenetic Opal CT to quartz transition zone.
3. 2D seismic lines show a positive reflection below the top negative reflection (Figure 4.4). The positive lower reflection appears to be a bottom reflection that creates a flat spot, which in turn suggests a possible gas-water contact.
4. Faults originating from amplitude anomaly 3 feature flags, stacked bright spots, acoustic masking and pull-down effects of underlying reflections (Figure 4.24). They are considered to be hydrocarbon indicators, and this would suggest that hydrocarbons leak from the sediment fan through N-S trending faults (Figure 4.24).

The total volume of the suggested fan, using an average thickness of 50 m and an area of $7.9*10^8$ m^2 is:

$$7.9 * 10^8 m^2 * 50m = 3.95 * 10^{10} m^3 = 39.5 km^3 \qquad \text{(Equation 5.1)}$$

The size of the fan makes it interesting as a possible prospect.

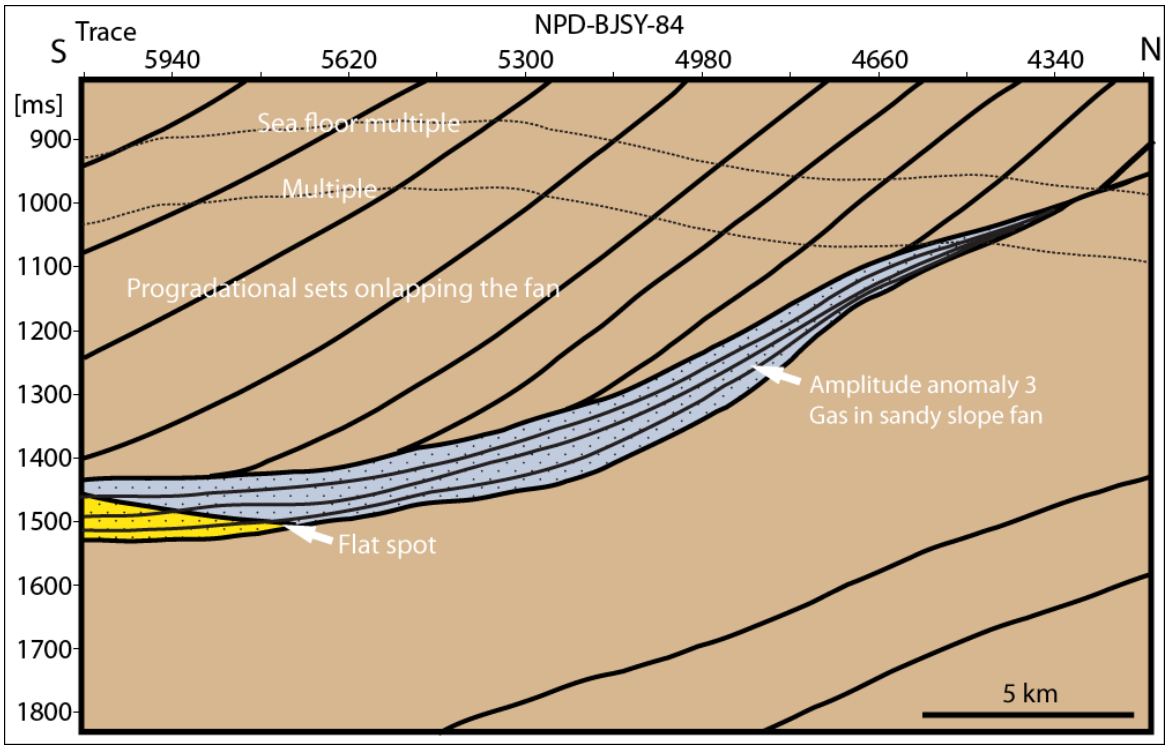

Figure 5.2. Sketch of possible interpretation of amplitude anomaly 3. Compare with Figure 4.4a. Gas is suggested to accumulate within a sandy fan. A reflection in the southern end of the anomaly may be interpreted as a flat spot. Reflections above the anomaly onlap the fan.

5.1.3 Category 3 – Mass movement deposits

Amplitude anomaly 4, 5 and 9 occur in relation to mass movement deposits. The amplitudes exhibit negative polarity reflections and acoustic masking beneath the anomalies (Figure 4.6, Figure 4.8 and Figure 4.13). Gas may be involved not only in that it accumulates within mass movement deposits but gas may also, in combination with unlithified sediments, reduce the shear strength of sediments, thereby making them more susceptible for triggering.

Amplitude anomaly 5 (Figure 4.8) is situated within GI sediments and is interpreted as a debris lobe from a mass movement deposit.

Amplitude anomaly 9 appears to be part of an area of mass movement deposits that covers the entire area in the SW part of the survey, between R7 and R1 (Figure 4.13). The high amplitude anomalies indicate that fluids accumulate within the sediments. It appears to be the root for at least 9 vertical fluid migration pathways.

Traps can be formed by slides and slumps commonly occurring within the Plio-Pleistocene sediments (Laberg and Vorren, 1996; Vorren et al., 1998). The negative anomalies indicate gas within the sediments. Acoustic masking below the anomalies is also an indication of gas that is most likely present in the slides because of the observed high seismic attenuation, which is normally caused by gas. Mass movement deposits containing gas accumulations have been interpreted to occur also within Plio-Pleistocene age sediments in Sørvestsnaget Basin (Andreassen et al., 2007a).

.

5.1.4 Category 4 – Fluid accumulations beneath and within glacial sediments

Many authors have published articles describing fluid accumulations within sediments (Laberg and Andreassen, 1996; Heggland, 1997, 1998; Fleischer et al., 2001; Mienert et al., 2005; Andreassen et al., 2007a; Hustoft et al., 2007; Løseth et al., 2008; Crutchley et al., in press). Løseth et al. (2008) has published a review article and refer to vertical fluid migration and accumulations above the Gullfaks Field, similar to some of the features found in Veslemøy High .

Multiple zones of fluid accumulations are inferred from the 3D seismic data beneath or within glacial sediments. The Plio-Pleistocene sediments (GI-GIII) contain small scale stratigraphic traps. The top section of the Plio-Pleistocene wedge shows a toplap unconformity at R1 (Figure 4.6) that was created at the base of the ice sheet (Fiedler and Faleide, 1996). Amplitude anomaly 6 is situated at this toplap unconformity (Figure 4.6 and Figure 4.9). Further up in the strata, in the Pleistocene succession, traps are very weak features associated

with Intra Pleistocene 1 and 2 (Figure 4.6). These reflections may be caused by basal tills. Amplitude anomaly 7, 11, 12 and 13 are located beneath the Intra Pleistocene 2 reflector and amplitude anomalies 8 and 14 are located beneath the Intra Pleistocene 1 reflector.

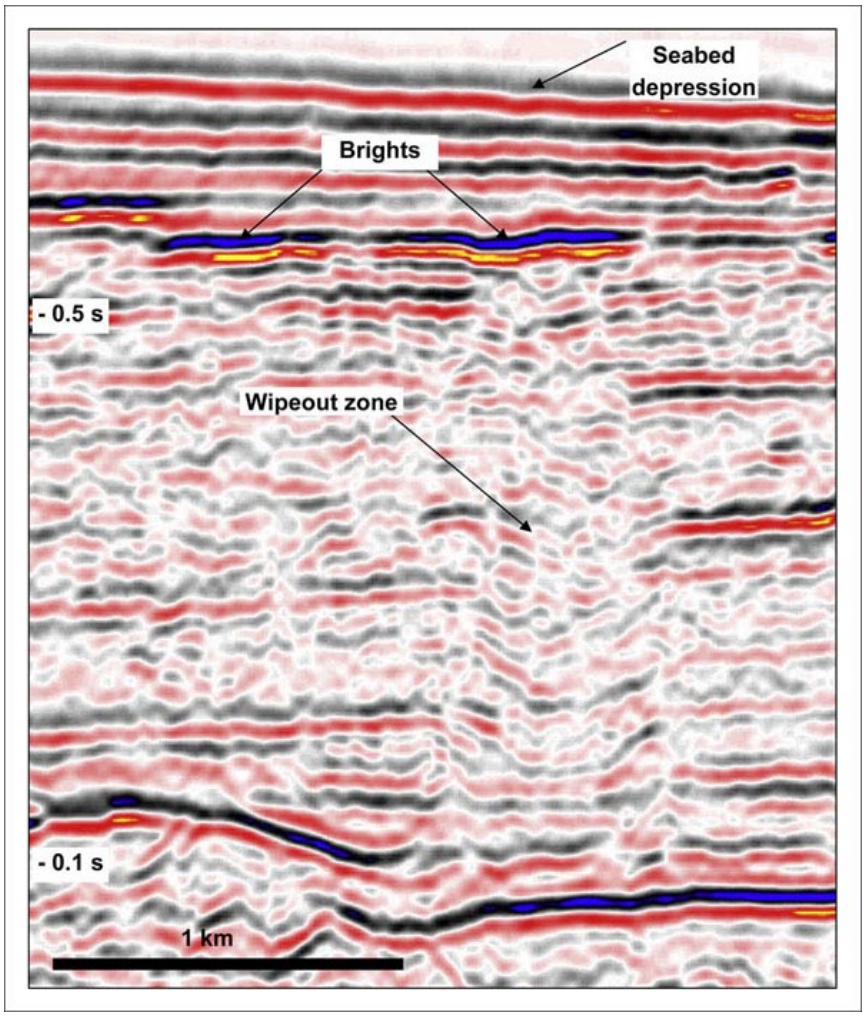

Figure 5.3. Løseth et al. (2008) has interpreted this wipe-out zone above the Gullfaks Field as a gas chimney and the high amplitude anomalies as gas-charged shallow sands and depressions as pockmarks. It is interesting to note that a connecting leakage process has been interpreted to take place between the gas-charged sands and the pockmarks but no seismic leakage anomalies are observed, demonstrating that not all leakage conduits are imaged on seismic data. (Løseth et al., 2008)

Amplitude anomalies 6.1, 6.2 and 6.3 suggest fluid accumulations within a thin layer sealed by a less permeable layer above and the toplap unconformity of the R1 reflector (Figure 4.9), a regional subcrop trap using the terminology of Allan et al. (2006). It is a single strong reflection. It is therefore interpreted as accumulation within a layer thinner then the resolution limit (see sketch of possible interpretation in Figure 5.4), e.g. between 5 (1/20 λ) and 24 m (1/4 λ). Amplitude anomalies 6.1, 6.2 and 6.3 have an uneven shape at the top and an even shape at the bottom (see Figure 5.5, where the black lines mark the even lower boundaries or

flat spots). The even bottom terminations are interpreted as the boundary between gas and water content. They are aligned along three different two-way travel times (anomaly 6.1: 928 ms TWT; anomaly 6.2: 949 ms TWT and anomaly 6.3: 904 ms TWT). This would indicate that at least three different layers exist with non-connected compartments in which gas can accumulate. Moreover, amplitude anomalies along Intra Pleistocene reflectors (amplitude anomaly 7, 8 and 11) are located above the different compartments of amplitude anomaly 6 (Figure 5.5).

Vertical fluid migration features 18, 19 and 24 along with several smaller migration pathways connect anomaly 6 to the anomalies above (anomaly 7, 8 and 11). Fluids migrate along strata within the Plio-Pleistocene wedge up to the toplap unconformity beneath R1 where they accumulate in at least three compartments (amplitude anomalies 6.1, 6.2 and 6.3). Fluids then leak vertically, from the highest points of the accumulations, up to accumulations beneath Intra Pleistocene 2 and 1 (amplitude anomalies 7, 8 and 11) (Figure 4.11, Figure 4.15 and Figure 5.5).

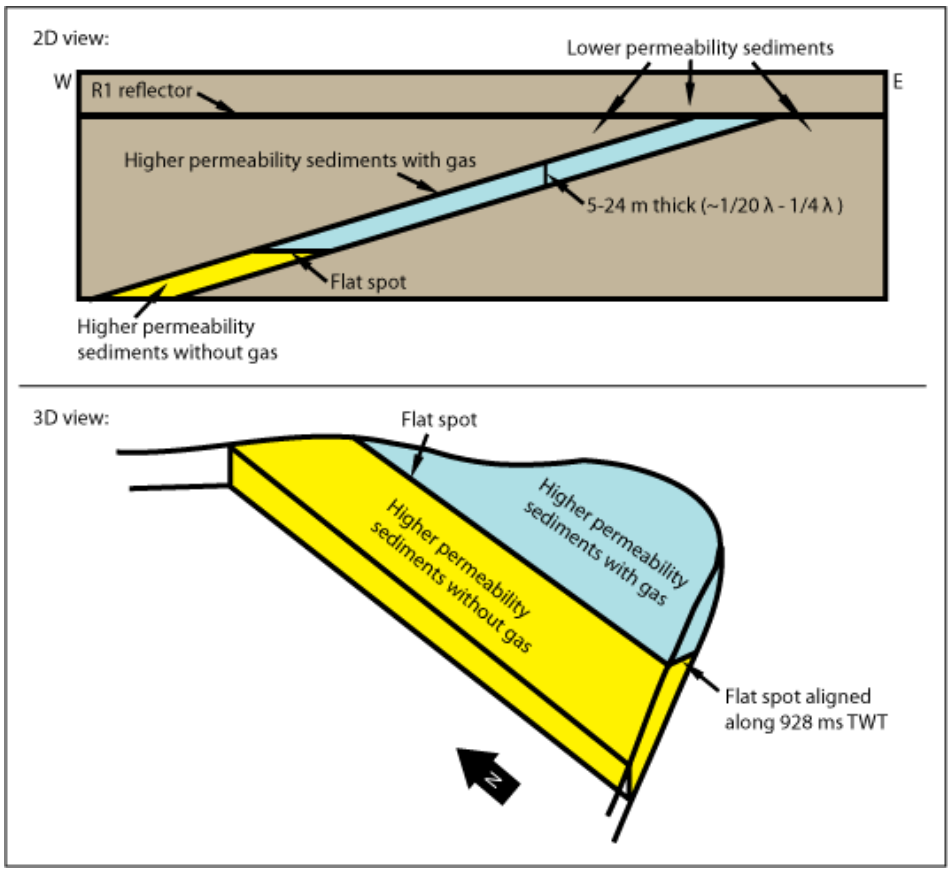

Figure 5.4. Model of possible interpretation of amplitude anomaly 6.1. The anomalies are suggested to arise from gas within thin layers of higher permeability. The flat spot cannot be observed in 2D, but in 3D the anomalies have irregular shapes in the eastern topmost section and appear to be flat in the lower western section. The lower terminations on the bright spots are laterally at a constant two-way time. Compare with Figure 4.9 and Figure 4.11 (seismic section).

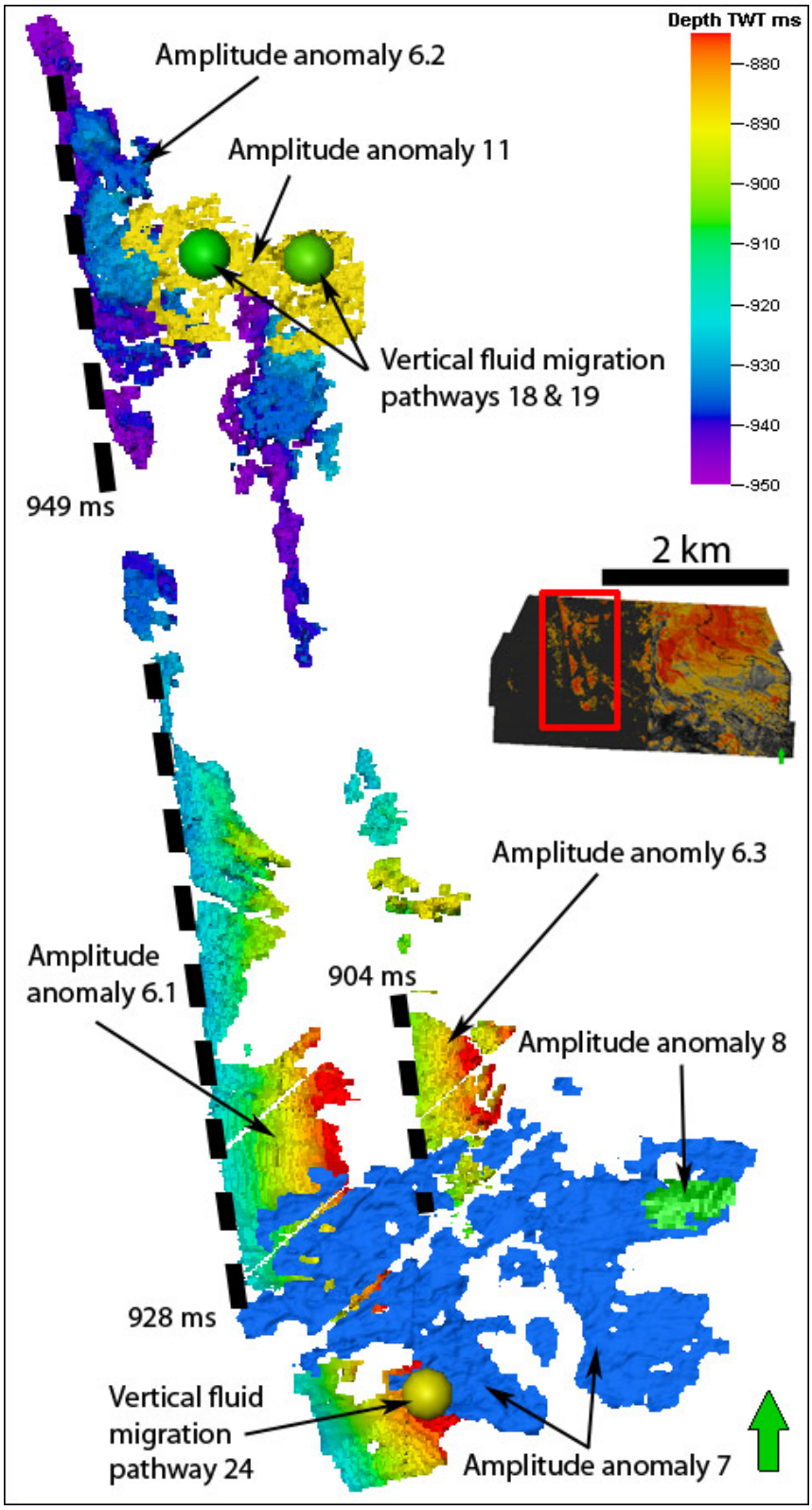

Figure 5.5. Top view map of amplitude anomaly 6, 7, 8 and 11. Amplitude anomaly 6 lies in the bottom and is displayed in timescale. Amplitude anomaly 7 (blue), amplitude anomaly 8 (green) and amplitude anomaly 11 (yellow) are located above amplitude anomaly 6 and are projected onto the map. Notice that the anomalies above amplitude anomaly 6 are located over the apexes of the different compartments of anomaly 6 and that the lowermost anomaly (anomaly 6) is connected to the anomalies above with fluid migration pathways 18, 19 and 24 (vertical migration pathways are color-coded). The flat spots of amplitude anomaly 6 are indicated with black lines. The flat spots can be mapped along three specific two-way times (Anomaly 6.1 at 928 ms TWT; anomaly 6.2 at 949 ms TWT and anomaly 6.3 at 904 ms TWT).

Amplitude anomaly 7 suggests a gas accumulation beneath the basal till of Intra Pleistocene 2 reflector (Figure 4.11). The anomaly is tilted (low in NW and high in SE) and does not appear to be contained by a trap. However, a possible trap could be a very subtle pinch-out trap. *Amplitude anomaly 8* may indicate a small gas accumulation, under the Intra Pleistocene 1 reflector and it is also tilted (deepest in W and highest in E). Both accumulations appear not to be contained by obvious traps. The lack of an obvious trap may indicate an active but low rate fluid flow system. Other possible interpretations of the amplitude anomalies along Intra Pleistocene 1 and 2 include glacially redistributed sediment blocks (e.g. Andreassen et al., 2007b), moraine material and acoustic signal interference effects. The anomalies aligned along Intra Pleistocene 1 and 2 (Figure 4.25 and Figure 4.27) do however not resemble the shape and characteristics of these types of sediments. Anomaly 6 is connected to anomaly 7 and anomaly 8 via vertical fluid migration pathway 24 (Figure 5.5).

Amplitude anomaly 11, 12 and 13, like amplitude anomaly 7, show fluid accumulations beneath the Intra Pleistocene 2 reflector. This reflector is interpreted as a low permeability layer, possibly a basal till, beneath fluids may accumulate. The shapes of the anomalies are not clearly confined but suggests very subtle traps beneath the relatively flat reflector. The anomalies are associated with several vertical zones of distorted reflections both above and below the anomalies (Figure 4.26). Anomaly 6 is connected to amplitude anomaly 11 via fluid migration paths 18 and 19 (Figure 5.5) and anomaly 9 is connected to anomaly 12 and 13 with fluid migration pathways 9 and 10.

Amplitude anomaly 14 suggests fluid accumulation beneath the basal till of the Intra Pleistocene 1 reflector (Figure 4.16 and Figure 4.17). It is the largest bright spot at this level and it is associated with a vertical fluid migration pathway (Feature 3) that originates at amplitude anomaly 1 and terminates at amplitude anomaly 14. Fluids may migrate from amplitude anomaly 1, in L. Paleocene-E. Eocene sediments, through fluid migration pathway 3, up to anomaly 14 in Pleistocene sediments.

5.1.5 Category 5 – Channels

Amplitude anomaly 10 occurs in sediments of Late Pliocene age (GI) and it has the appearance of a fan/channel system (Figure 4.14). GI sediments are, as mentioned above, of delta facies which is consistent with the interpretation of anomaly 10 as a channel/fan complex. A submarine fan/channel system consists of sorted sediments of finer and coarser fractions in different parts of the channel (Clark and Pickering, 1996). The areas with coarser sediments are likely to have higher porosities and permeabilities then finer sediments and may

therefore provide a better conduit for fluid flow. Amplitude anomaly 10 may therefore be considered as an example for fluid migration pathways in delta facies sediments within unit GI (Figure 5.6).

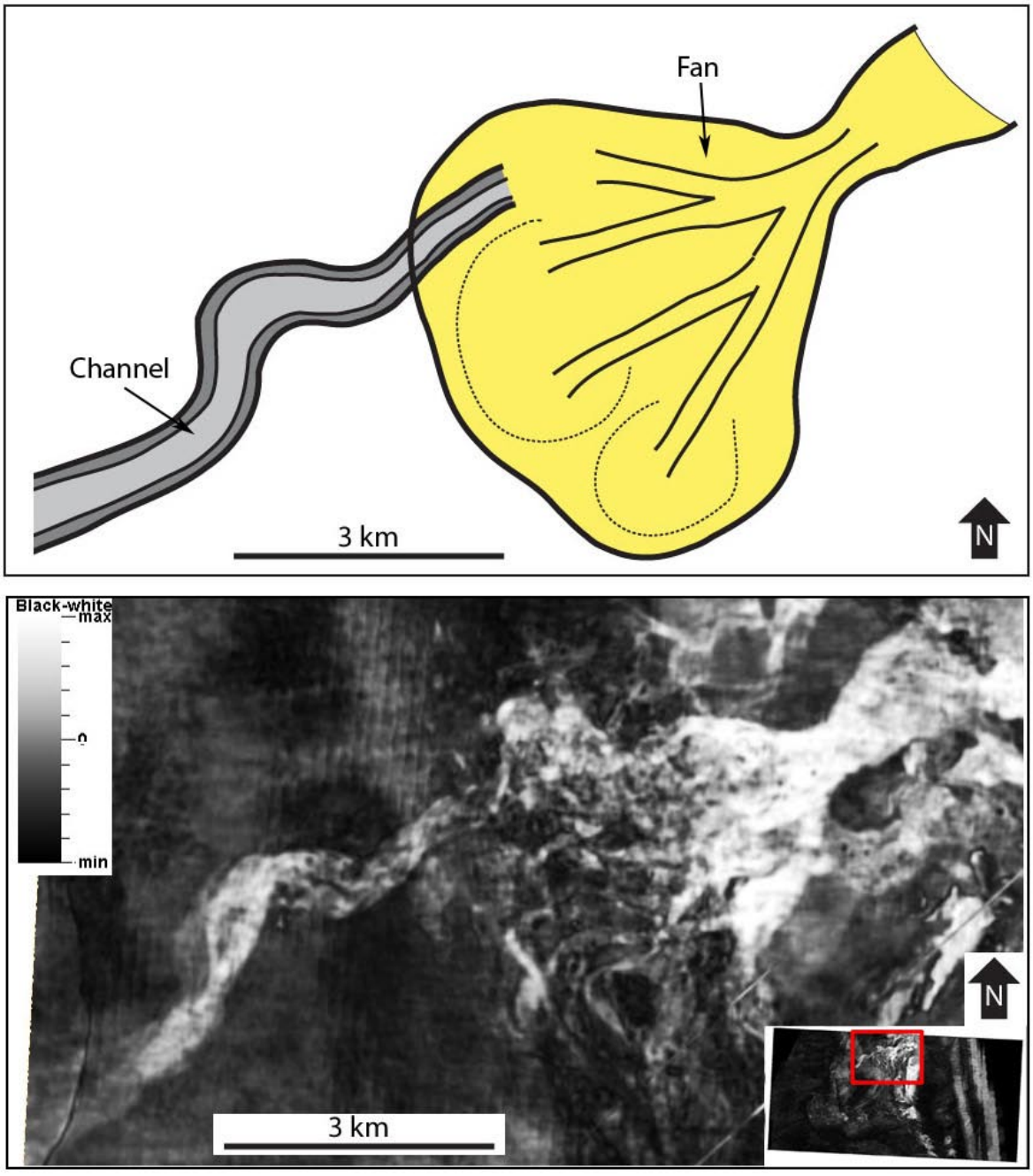

Figure 5.6. Top) Interpretation of amplitude anomaly 10 as a fan complex originating from NE and a channel (gray) extending out from the fan. Compare with bottom; Arbitrary RMS slice through amplitude anomaly 10.

5.1.6 Acoustic signal interference effects

High amplitude anomalies, like the anomalies along Intra Pleistocene 1 and 2, can be a result of interference between the seismic pulse representing the top AI contrast and the seismic pulse representing the lower AI contrast. This happens if the layer thickness is less than a quarter of a wavelength (Widess, 1973). In amplitude anomaly 8 the amplitude values vary from 32767 (potentially higher as 32767 is the maximum value of the 16 bit data) within the anomaly to about 4000 outside the anomaly, over a distance of only 50 m (Figure 5.7). The amplitude strength outside the anomaly is only 1/8th of the amplitude strength inside. The reflection has an amplitude strength varying between 2000-7000 in the areas of the reflection outside the anomalies, this corresponds to amplitude 1 (Figure 5.8).

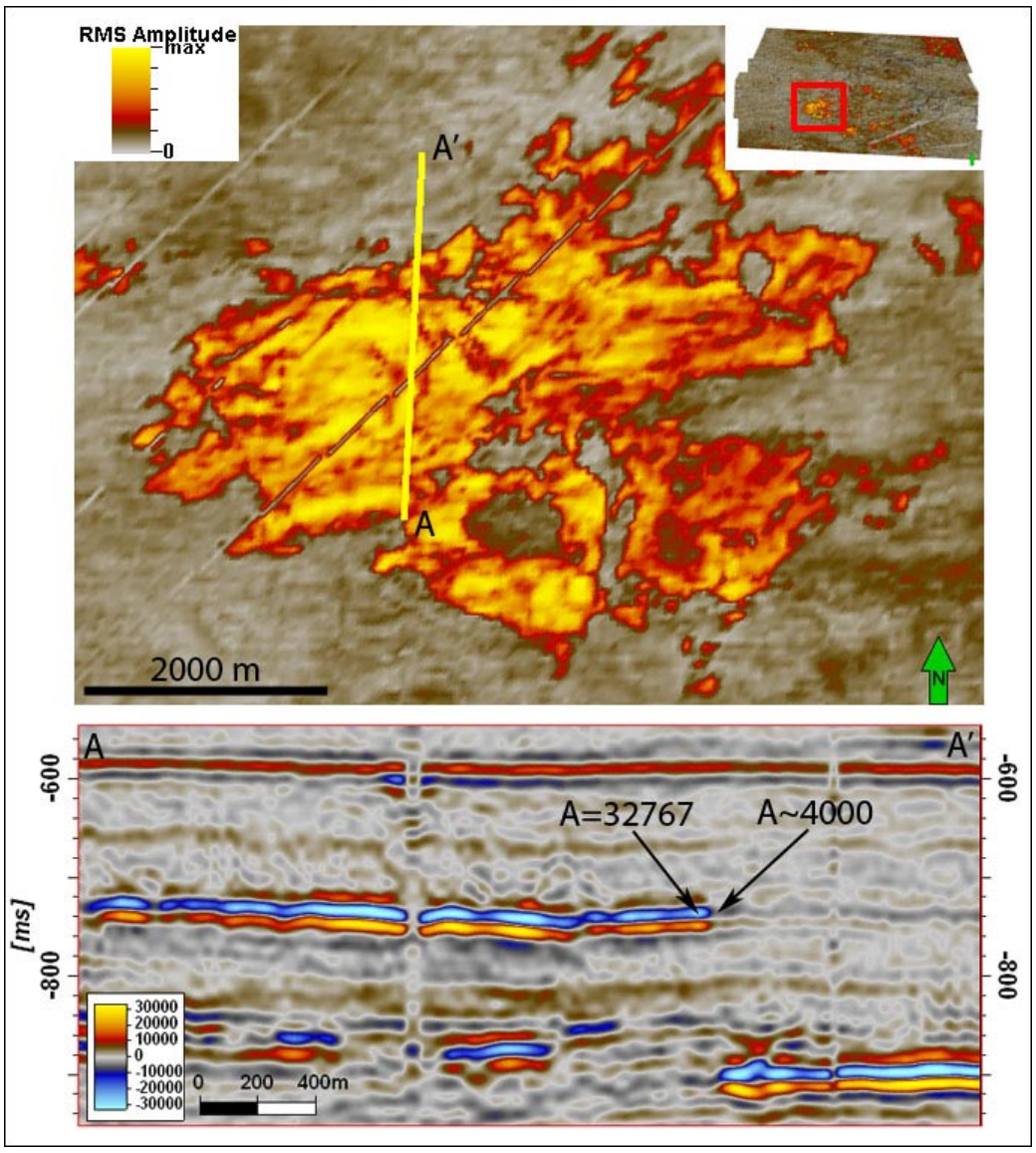

Figure 5.7. Top) RMS amplitude map of amplitude anomaly 7. Bottom) Seismic intersection A-A' with amplitude values indicated.

As can be seen in Figure 5.8 the maximum amplitude that can be attained by the interference between two layers is approximately 1.4 times the unaffected amplitude which is measured at 2000-7000 in the reflection of Intra Pleistocene 2. This also corresponds well to relative effective seismic amplitudes as a function of layer thickness described in literature (Avseth et al., 2005). An amplitude of 1.4 times the measured value of the reflector (2000-7000) corresponds to a maximum of 9800, nowhere near the value of 32767 observed in the amplitude anomalies of Intra Pleistocene 1 and 2 (Amplitude anomaly 7, 8, 11, 12, 13 and 14). An amplitude variation of eight times also corresponds to a significant difference in true thickness of the layer creating the tuning. Figure 5.8 shows an example model of a sand layer within shale (Bacon et al., 2003). Aossible explanations apart from a shallow gas accumulation are several layers that may interfere to create a stronger reflection. However, it appears unlikely that the glaciomarine processes in the study area could have deposited several layers in the pattern displayed in Figure 5.7.

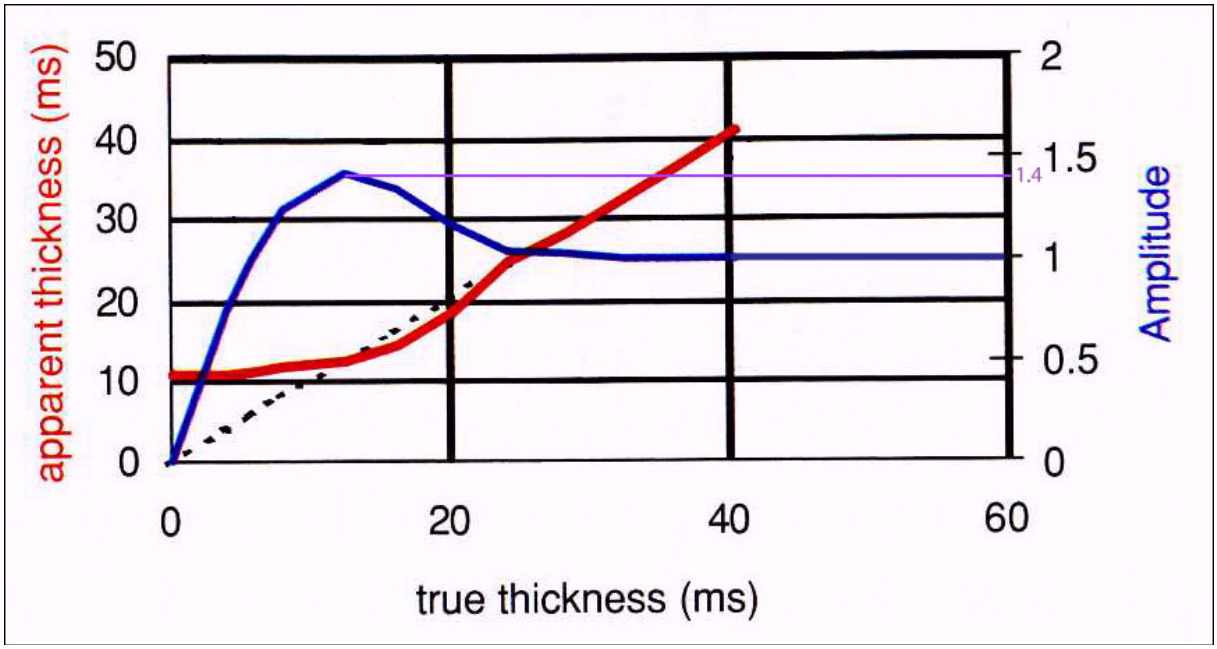

Figure 5.8. Wedge model diagram of Amplitude plotted versus apparent thickness (ms) and true thickness (ms) in a tuning scenario. (Modified after Bacon et al., 2003)

5.2 Fluid migration and accumulation from Tromsø Basin (eastern section)

Sediments of Late Cretaceous-Early Eocene age have been deposited in a marine environment. In the nearby wells these sediments consist of shales with stringers of sand and silt. The Pleistocene succession consists of glacial sediments.

High amplitude anomalies and focused fluid flow expressions are distributed throughout sediments from the Cretaceous to the Quaternary. The distribution indicates migration from deeper stratigraphic levels. The most extensive high amplitude anomalies interpreted to originate from the eastern basins are found in the SW corner of the 3D survey at the Top L. Cretaceous/L. Paleocene reflection and beneath Top E. Eocene (amplitude anomalies 1 and 2), within the E. Eocene (amplitude anomaly 3), at the URU reflection, above the URU's highest point within the Pleistocene succession and within the Pleistocene succession above amplitude anomaly 1 and 2 (amplitude anomaly 14) (Figure 4.3).

5.2.1 Fluid migration pathways in Cretaceous, Paleogene and Quaternary sediments related to fluid migration from Tromsø Basin

Distributed fluid migration may originate in the east at the deeper Tromsø Basin, and focused fluid flow may occur along strata from Tromsø Basin to Veslemøy High. As fluids reach the apex at Veslemøy High (accumulations in amplitude anomaly 1 and 2 (Figure 4.3)), vertical and focused fluid migration takes over from lateral strata migration (focused fluid flow feature 3 (Figure 4.3 and Figure 4.23)). Vertical migration may concentrate along high permeability areas and fractures. However, both Darcy flow (low flow rates) and fracture flow (high flow rates) are still possible flow mechanisms.

Bright spots aligned along a fault plane, so-called flags, and scattered bright spots at reflections along a fault, are often considered direct hydrocarbon indicators (DHIs) (Sheriff, 2006). These high amplitude anomalies are observed along small throw, N-S trending faults within the Tertiary sediments (Feature 1 and 3-6, Figure 4.23, Figure 4.24). Faults may be main conduits for fluid flow, especially at greater depths where sediments have become more consolidated or completely lithified (Ligtenberg, 2005). Fault cores often act as a conduit for fluid flow during deformation but then become cemented and sealed due to increasingly low permeability (Caine, 1996). If, however, the faults become reactivated it is more likely that they act as a conduit to fluid flow (Caine, 1996).

Regional tectonic forces associated with ridge push along the Mid-Atlantic ridge and its continuation along the Gakkel Ridge in the Arctic, create an overall N-S tectonic stress in the Barents Sea. The horizontal principal stress orientation is approximately N 177°. In the well 7219/9-1, located east of EL0001, the orientation is 164° ± 15° (Gölke and Brudy, 1996). In theory, the faults aligned along the regional stress direction (N-S in the Barents Sea) will have a greater tendency for being permeable than faults aligned perpendicular to the stress direction. N-S trending faults are likely to experience movement along the fault-plane and E-

W trending faults are likely to be closed by the forces. This fits well with observations (fluid flow feature 1-6, Figure 4.24) made within the EL0001 survey. Other possible factors in the reactivation include postglacial rebound and elevated pore pressure from underlying gas reservoirs (Wiprut and Zoback, 2000).

The high negative polarity amplitudes occur at the Top Late Cretaceous/Late Paleocene reflection (Figure 4.3 and Figure 4.23). The anomalies can be followed down to more than 1950 ms TWT below the seafloor. It corresponds to 2440 m depth using an acoustic velocity of 2500 m/s. Using the average geothermal gradient 33.9°C of the three wells in the area, sediments at 2440 m below the seafloor would have a temperature of 83 °C. Biogenic methane will not form in temperatures over 75°C (Buswell and Mueller, 1952; Ziekus and Wolfe, 1972; Rice, 1981; Rice, 1992). Thus, if there are hydrocarbons present they will have to be either from older biogenic gas reservoirs which have been buried deeper than their original depth, or gas of thermogenic origin.

Vertical migration in Paleocene to Eocene sediments is mainly associated with small N-S trending faults (fluid flow features 1 and 3-6 (Figure 4.23 and Figure 4.24)). The fluid flow expressions often terminate at mass movement deposits of the Plio-Pleistocene wedge. Here, the mass movement deposits show high negative amplitudes. Sediments below the URU reflection show distorted reflections and a diffuse acoustic pattern. One possible interpretation is the low flux and diffuse flow that terminates at the URU. The URU displays high negative polarity amplitudes over large areas that may be associated with accumulations of fluids beneath the basal till which constitutes the URU.

In the Nearby Bjørnøya Basin, bordering Veslemøy High to the north, most gas and gas hydrate accumulations are located immediately above or in the vicinity of large faults (Laberg and Andreassen, 1996). The Bjørnøyrenna Fault Complex, bordering Veslemøy High to the north-east and east shows similar features (Andreassen et al., 1990). Even though the Bjørnøyrenna Fault Complex is in a different tectonic stress regime then the Veslemøy High faults, faults are likely candidates to act as conduits for fluid flow also at Veslemøy High. Thirty vertical zones of disturbed reflections occur in the Veslemøy High area (section 4.3) and are interpreted as zones of vertical fluid migration. Eight out of thirty are migration paths connecting deeper sediments of Cretaceous and Tertiary age to the Pleistocene succession.

Vertical fluid migration through the Pleistocene succession (GIII) overlying the URU reflector is not associated with visible faults. Fluid migration processes are more likely related to overpressure that allows self enhanced fluid flow pathways through the glacial sediments.

Pockmarks at the seafloor suggest high fluid fluxes in times of episodic discharges or sudden catastrophic fluid flow events (Hovland et al., 2005). Fluids from the Cretaceous sediments and the suggested Early Eocene sediment fan (amplitude anomaly 3, Figure 4.4) migrate up to the URU through small faults. Fluids accumulate underneath the URU and migrate along the URU to shallower depths. When the shallowest depth is reached (in the NE corner of the survey) the fluids migrate vertically to the seafloor via fluid flow features 15-17 and 20-23 (Figure 4.25, Figure 4.26 (B-B') and Figure 4.27).

5.2.2 Origin of hydrocarbons in areas east of Veslemøy High

Hydrocarbons in the fluid migration system in Veslemøy High may have been trapped in reservoir formations within Tromsø Basin and sealed over extended periods of time. Triggered by the ice ages with erosion/deposition of glacial sediments, pressure differences and gas expansion, or the tilting of reservoirs took place (Kjemperud and Fjeldskaar, 1992; Nyland et al., 1992). The exhumation of the Barents Sea has been extensive in the areas surrounding Hammerfest Basin, Loppa High and the northern Barents Sea (Figure 5.9)(NPD, 1996). The zero meter erosion contour is situated in the western edge of Veslemøy High which suggests no erosion west of Veslemøy High and limited erosion on Veslemøy High. StatoilHydro operates with erosion of 0-200 m on Veslemøy High (StatoilHydro unpublished). East of Veslemøy High, however, the contours are very close which suggests large differences in erosion over small distances. This could lead to large stresses within the Bjørnøyrenna Fault Complex and nearby areas, and reactivation of faults. Hydrocarbon reservoirs may become breached by reactivation of faults in association with ice loading.

Another possibility is that hydrocarbons migrate more directly from the reservoir rocks present in the basins to accumulations present in Veslemøy High. The temperature range at which oil and gas is generated varies with kerogen type, timing and several other factors (Perrodon, 1983). Typical ranges for the oil window (65° to 150°C) and the gas window (100° to 200°C) will be used for the following discussion (Perrodon, 1983). The thermal gradient of wells 7219/8-1S and 7219/9-1, east of Veslemøy High are 37,5°C/1000 m and 33,8°C/1000 m respectively. In Tromsø Basin and Bjørnøya Basin, Cretaceous sediments occur mainly deeper than 10 km (Faleide et al., 2008), which means that Paleozoic and Triassic source rocks are probably over mature or exhibit gas window maturities. Within the Bjørnøyrenna Fault Complex and the Ringvassøy-Loppa Fault Complex tectonic activity and faulting has lead to shallower depths of parts of the Jurassic and Cretaceous source rocks (Knurr Fm. and Hekkingen Fm.). They may therefore exhibit gas or oil window maturities on shallow lying

fault blocks. Base Cretaceous is located at 3319 mMSL TVD at well 7219/8-1S which is drilled into a rotated fault block. Organic geochemical screening analyses in well 7219/8-1S show consistently high TOC over the Early Cretaceous to Late Jurassic interval, 2815 to 3740 MD RKB (typically 2-3.8%). These intervals may exhibit both oil and gas window maturities where the interval is located deeper. Significant quantities of hydrocarbons have been present in well 7219/8-1S where a 200 m (112 m gas + 88 m oil) residual paleo-hydrocarbon column has been identified (Knutsen et al., 2000). These hydrocarbons may still exist in less tectonically active parts of the area.

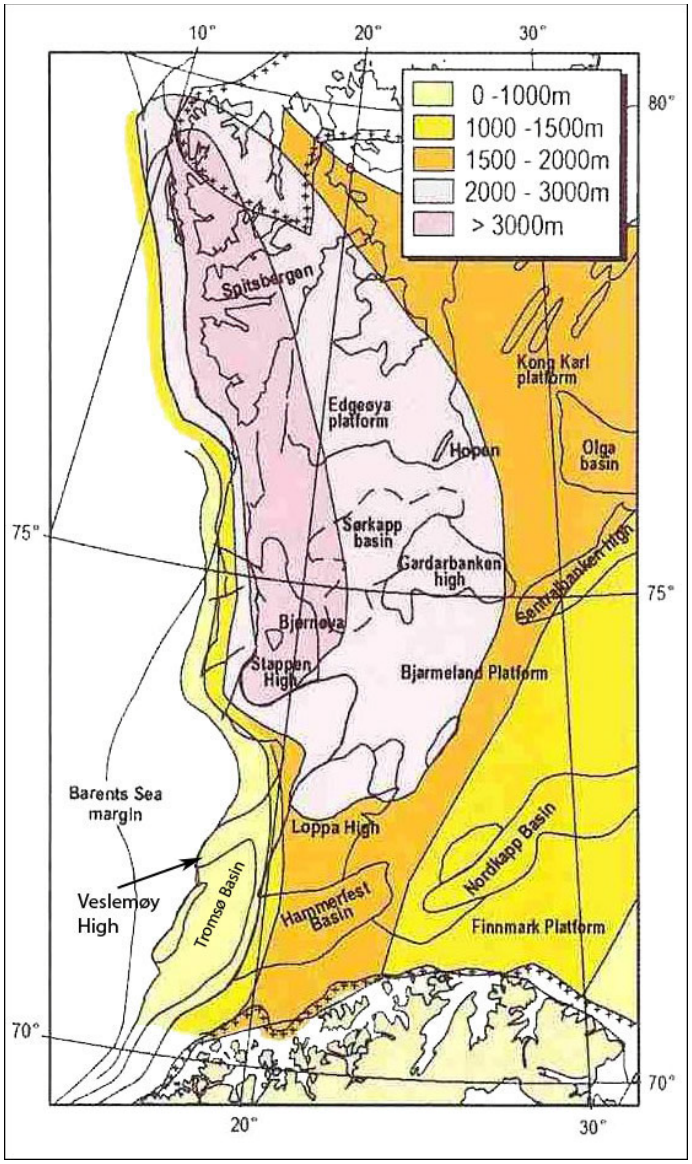

Figure 5.9. Erosion in the Barents Sea (NPD, 1996).

5.3 Fluid migration from the Sørvestsnaget Basin (western section)

In the western section of the 3D survey high amplitude anomalies and distinct vertical zones of disturbed reflections are limited to the Plio-Pleistocene wedge (GI-GII) and the overlying Pleistocene succession (GIII). Migration of fluids from the western basins takes place mainly within the upper Plio-Pleistocene sediments but seems to be absent or at least not visible deeper than R7.

5.3.1 Fluid migration pathways in the Plio-Pleistocene wedge (GI-GII) and the Pleistocene succession (GIII).

The sediments within GI are of delta facies while the sediments within GII are of slope facies in the Sørvestsnaget Basin (Andreassen et al., 2007a). They have a similar seismic appearance in Veslemøy High. The sediments within GI and GII contain gravity driven sediment flows (Laberg and Vorren, 1996; Vorren et al., 1998). Typical delta deposits will have grain size variations due to the shifting environments and discharge within the delta (Leeder, 1999). Amplitude anomalies 5 and 10 are examples of a debris lobe from a slide and a channel respectively. Variations from high energy, coarse-grained and high permeability deposits to low energy, fine-grained and low permeability deposits exists in the study area. This interlayering of high- and low permeability sediments along with the inclination of layers creates pre-conditions for lateral fluid-flow from the western basins towards Veslemøy High. Fluid migration in the western section is primarily concentrated in the GI unit.

Thirty vertical migration pathways (described in section 4.3) suggest vertical fluid migration, 22 of which originate at intervals at or above R7/URU. Most of the vertical fluid migration pathways which originate at R7/URU or further up are located above the Plio-Pleistocene wedge (14 out of 22) (Figure 4.22), this suggests that the Plio-Pleistocene wedge is a main conduit for fluid flow. The interpretation is based upon the resemblance of vertical fluid flow pathways to previously described hydrocarbon leakage pathways (Heggland, 1997, 1998; Bünz et al., 2003; Berndt, 2005; Hansen et al., 2005; Ligtenberg, 2005; Gay et al., 2006; Cartwright et al., 2007) as well as their relationship to bright spots interpreted as hydrocarbon accumulations.

Within the Plio-Pleistocene strata (GI-GIII) visible migration takes place primarily along strata from Sørvestsnaget Basin to Veslemøy High until it reaches any feature which disrupts the sealing layers, e.g. a toplap unconformity or chaotic layering within a mass movement

deposit. Afterwards, fluids may migrate vertically through the Plio-Pleistocene succession (GIII).

Fluids are geophysically observed to migrate along strata within the Plio-Pleistocene wedge up to the toplap unconformity of R1. At the toplap unconformity fluids accumulate, for example in anomaly 6 (Figure 4.9) and 9 (Figure 4.13) or migrate vertically through GIII sediments like in feature 26 (Figure 4.30). From anomaly 6 fluids migrate vertically in fluid migration paths 18 and 19 to anomaly 11 (Figure 4.15) at Intra Pleistocene 2, and through fluid migration path 24 into anomaly 7 and from there to anomaly 8 (Figure 4.11 and Figure 4.28). Within anomaly 9 the layers of the Plio-Pleistocene strata are disturbed which disrupts the migration along the layers and enables vertical migration. From anomaly 9 fluids migrate vertically through fluid migration path 10 into anomaly 12 and through fluid migration paths 9, 27 and 28 into anomaly 13 (Figure 4.17 and Figure 4.25).

The main migration may be Darcy flow and diffusion through the sediment pore-network. In this case, fluid fluxes will be low. Highly soluble gases like methane and CO2 may be transported dissolved in water. However, if the fluids reach an overpressure greater than the fracturing pressure of lithified sediments there may be a rapid expulsion of fluids to the surface until the pressure reaches equilibrium. Fractured flow has a much higher flow rate then Darcy flow (Roberts and Nunn, 1995; Krooss and Leythaeuser, 1996). After the expulsion event fractured pipes may be closed but another pipe may form or the same pipe may become reactivated when the pressure has reached the tipping point. Sediment loading of over 100 cm/ka is documented as a source of overpressure in basins around the world (Rubey and Hubbert, 1959; Fertl, 1976). Very rapid rates of deposition, on average 172 cm/ka with a maximum of 339 cm/ka, has been documented in the Bear Island Fan on the continental margin west of Veslemøy High (Fiedler and Faleide, 1996). Overpressure build up in this area may have influenced fluid migration towards the Veslemøy High. If so, episodic fluid eruptions and hydraulic fracturing leading to pipe generation may be considered at Veslemøy High. Natural hydraulic fracturing is an efficient process to create permeable pathways for focused fluid upflow at submarine venting sites (Løseth et al., 2001; 2003; Zuhlsdorff and Spiess, 2004). This may be a cause for the pockmarks observed at the seafloor.

5.3.2 Origin of hydrocarbons in western basins

In the basins west of Veslemøy High there has been no or very limited net erosion by the ice sheet (NPD, 1996). This makes erosion of glacial sediments not a likely trigger mechanism for the fluid migration system. However, high sedimentation may have caused differential

subsidence, which may have resulted in tilting of underlying reservoirs and gas migration (Andreassen et al., 2007a).

Based on the provided seismic evidence, a hypothesis is put forward that hydrocarbons migrate into Veslemøy High laterally from western basins. Either from tilted reservoirs mentioned above or more directly from the source rocks. In the following, the origin of hydrocarbons will be discussed based on measured thermal gradients and potential hydrocarbon windows. The thermal gradient (well 7216/11-1S) in Sørvestsnaget basin is 30.5°C/1000 m. Using the assumed oil and gas window ranges stated the oil window is reached between approximately 2100-4900 m below seafloor (mbsf) depth and the gas window between 3300 mbsf and 6500 mbsf.

In the western basins, Cretaceous sediments reaches down to more then 4500-5000 ms TWT (Ryseth et al., 2003), Top Jurassic is often unmapped since it is too deep. Paleozoic, Triassic and Jurassic is mapped on seismic data and the source rocks will most probably be in the higher ranges of the gas window, over mature or burned out in all areas except for localized highs. NPD states that source rocks of Early Aptian age may be present in this area. Well 7216/11-1S shows over 1000 m of Paleocene to Lower Eocene sediments that consists of dark grey, laminated mudrock deposited in a generally low-energy marine environment. Microfaunal evidence indicates a poorly oxygenated deep marine shelf or bathyal environment (Ryseth et al., 2003). These shales are located at depths from 4186 to 3166 m TVD (128° to 97°C) and may have attained oil and gas window maturities in some areas of the basin.

The Haakon Mosby Mud Volcano provides a window to the deep geosphere. It is located only 80 km west of Veslemøy High (86.5 km from the EL0001 3D survey). The composition of gases emerging from the mud volcano were studied and show clear evidence for both thermogenic and biogenic gas (Lein et al., 1999). Tertiary strata dips towards the west and the hydrocarbons detected at HMMV could resemble the composition of gas seeping out in Veslemøy High. It has therefore been speculated that the main zone of methane generation is located below the 3100 m thick layer of glacial sediments or alternatively within organic-rich interglacial sediments in the lower parts of the 3100 m thick succession of glacial sediments (Lein et al., 1999). They further argue that the generation of biogenic methane may have occurred in the upper part of hemipelagic sediments of Pleistocene to Middle Miocene age.

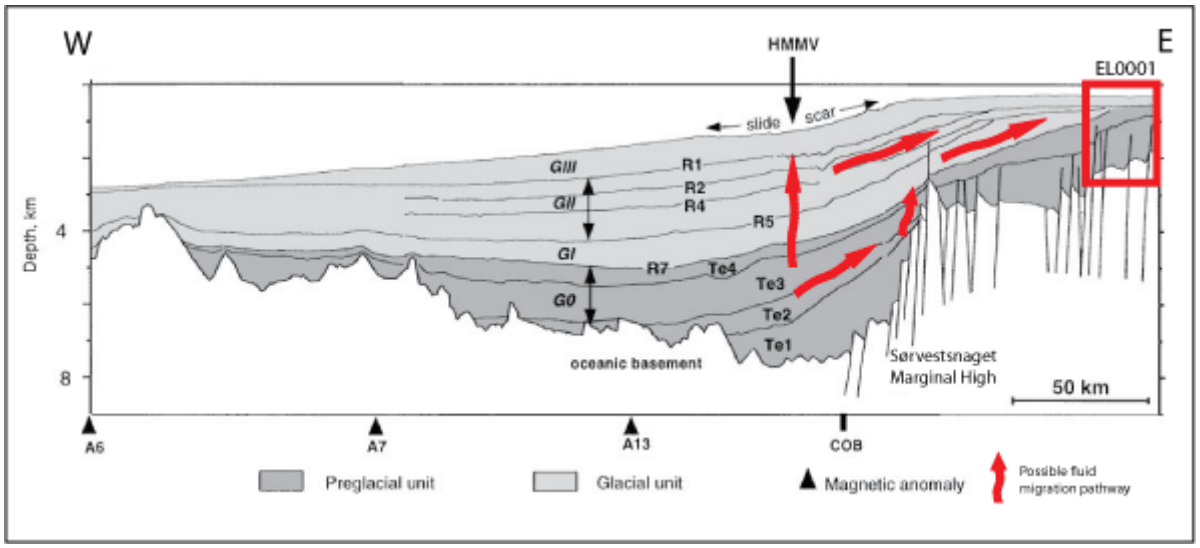

Figure 5.10. Top) Seismic profile from the continental slope through Haakon Mosby Mud Volcano (HMMV) to Veslemøy High. Approximate location of EL0001 projected onto the profile. Possible fluid migration pathways indicated with red arrows, Sørvestsnaget Marginal High may act as a barrier to flow from deeper basins. Location of profile (from 2D seismic line Nestlante 19 and L7200-77) indicated in Figure 2.1. Modified from Hjelstuen et al (1999).

Hydrocarbons leaking from the deep source areas may not only fuel the Haakon Mosby Mud Volcano but also, along strata, the Veslemøy High. Middle Eocene sediments consist of sandstones and shales and the formation could be favorable to lateral migration if the high-permeability sandstones are laterally interconnected. The Sørvestsnaget Marginal High in contrast may act as a barrier for flow of hydrocarbons from deeper sediments generated (Figure 5.10). The basins east of the Sørvestsnaget Marginal High are not as deep as the basins west of it. Fluids from deeper basins may migrate laterally until they reach Sørvestsnaget Marginal High and then vertically until they can bypass Sørvestsnaget Marginal High. The high reaches up into the Plio-Pleistocene wedge, the level where evidence exists for lateral migration (Figure 5.10). Fluids are suggested to be diverted vertically as they encounter the high and associated faults. As the fluids reach the Plio-Pleistocene wedge (GI-GII) they may commence their migration along strata towards Veslemøy High.

5.4 Indications of fluid expulsion at the seafloor

There are several possible explanations for the circular and sub-circular depressions mapped on the seafloor (Figure 4.31).

First, sub-circular depressions have been previously interpreted as formed by icebergs (Bellec et al., 2008). Icebergs may occasionally strike the seafloor and create large sub-circular depressions difficult to distinguish from pockmark depressions (Woodworth-Lynas et al.,

1985). Also, wind and waves may cause icebergs to move in such a way that it could cause a sub-circular depression (Woodworth-Lynas et al., 1991).

Second, shallow seafloor depressions resembling pockmarks in Eckernförde Bay were interpreted as features resulting from the expulsion of freshwater from Holocene glacial lags and sands to the seafloor (Whiticar, 2002). This process involves groundwater which is not readily available at sites as far from land as Veslemøy High. Therefore, it is not a likely explanation, although expulsion of over pressurized saltwater may be considered.

Third, the most likely explanation are pockmarks created by gas expulsion (Hovland, 1981, 1982). Pockmarks appear as circular and sub-circular depressions at the seafloor formed as fluids migrate up through sediments at the seafloor. The sediments may be transported away with the seeping fluids or the formation process may be more violent and episodic (Hovland et al., 2005). Pockmarks may have connections to pipes and deeper hydrocarbon sources (see depression 1, Figure 4.32). Pockmarks are often found on the continental margins and may be associated with underlying hydrocarbon reservoirs (Heggland, 1998; Judd, 2007). At the study area, pockmarks display a weak tendency of higher concentrations in the western section (2/3 of the pockmarks). The frequency of pockmarks coincides with the frequency of mapped gas accumulations, fluid migration paths and estimated fluid flux of the Plio-Pleistocene wedge if compared to the eastern section of the survey. It supports the hypothesis that fluids migrate primarily from the western basins towards east through the Plio-Pleistocene wedge.

It is important to note that even though leakage conduits are not visible on seismic data there may be connections between pockmarks and vertical fluid migration pathways (e.g. Løseth et al., 2008) (compare with Figure 5.3).

Pockmarks range in size from micro scale where the limit, in seismic data, is set by what is seismically resolvable to giants of more than a kilometer in diameter. Normal pockmarks are 10-700 m wide and up to 45 m in depth (Hovland et al., 2002). The pockmarks mapped in this study vary lateral extent; between 460x420 m and 1050x970 m. Pockmarks in the study area show no sizes smaller than 400 m in diameter. This is likely due to the interference with iceberg ploughmarks that occur all over the seafloor. Ploughmarks are typically 100–300 m wide with a relief of 3–10 m (Andreassen et al., 2008) and within this size range no pockmarks were identified (Figure 5.11). This leaves the possibility that a large number of smaller but undetectable pockmarks exist but avoid detection due to resolution limits.

Iceberg ploughmarks within the pockmarks (Figure 4.32) indicate they were formed before or during the last period of iceberg souring. Erosion by iceberg ploughmarks may have erased the evidence of small pockmarks that were present before the iceberg scouring period.

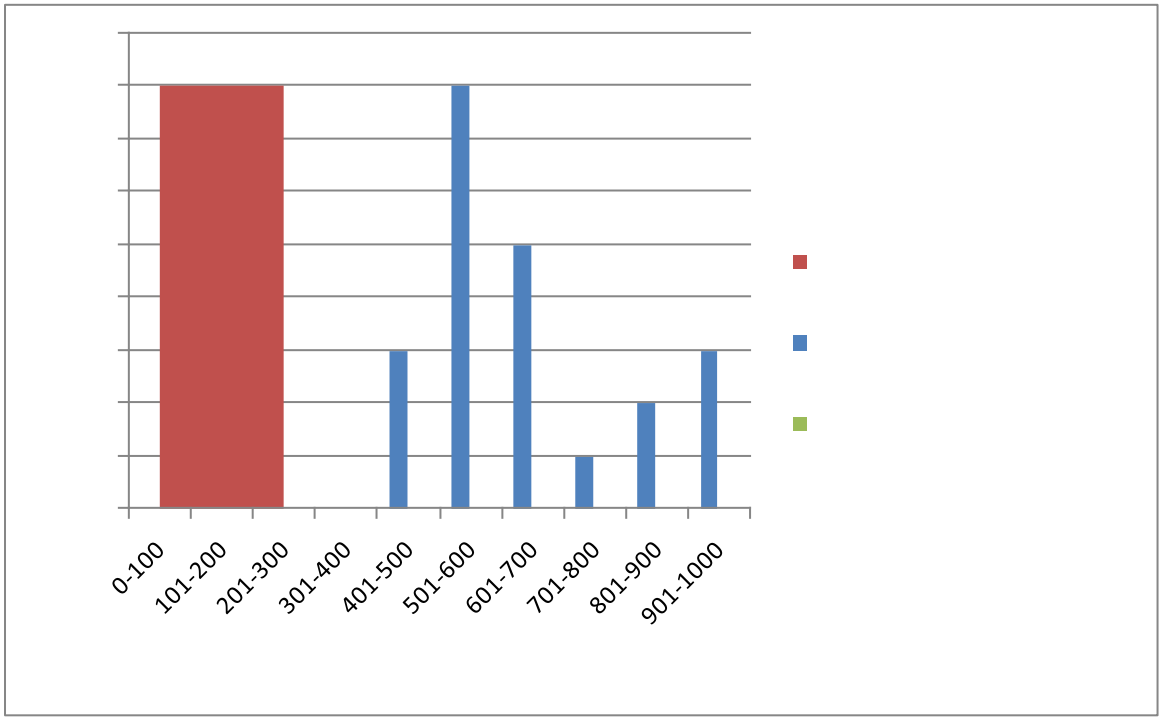

Figure 5.11. Diagram of size distribution of identified pockmarks along with the red zone which is the normal size range of ploughmarks.

5.5 An attempt to estimate fluid fluxes

An attempt was made to quantify potential fluid flux capacities in the working area. As there are no pore pressure data available for the area of Veslemøy High it was not possible to calculate permeabilities using Darcy's law. Therefore, calculations are based on typical flow rates using information from literature for different flow mechanisms (Roberts and Nunn, 1995; Krooss and Leythaeuser, 1996). They are compared with flux rates of fluids emerging at the seafloor (from literature in Table 5.2). The numbers attained from the model will be highly uncertain but provide ranges of fluid flow from the western basins relative to the eastern basins, and an approximation of the capacity of the fluid flow system.

The term Darcy flow is used to describe linear flow within permeable sediments. Darcy flow describes fluid flow in all situations except for situations in which the underlying assumption of flow through a bulk medium with a given hydraulic conductivity is not valid (Berndt, 2005). Such situations include flow through fractures if the fractures are big compared to the

area of interest and blow outs (turbulent flow, fracture flow), and flow on a microscopic scale (e.g. Fisher et al., 2003).

Fracture flow has a typical flow rate, which is often episodic, of $2*10^8$–$2.5*10^9$ $m^3/km^2/year$ (550-6850 1 m^{-2} day^{-1}) (Roberts and Nunn, 1995). Permeabilities of faults estimated from modeling and laboratory measurements range from 0.1 D-0.1 μD (10^{-13} to 10^{-20} m^2) with the higher permeabilities generally associated with the damage zone of the fault (Bruhn et al., 1994; Evans et al., 1997; Seront et al., 1998).

Darcy flow has a typical flow rate of 100–1000 $m^3/km^2/year$ (0.00027-0.0027 l m^{-2} day^{-1}) in low permeability sediments (Krooss and Leythaeuser, 1996). The Darcy flow velocities are calculated using a permeability of 1 nanodarcy (10^{-21} m^2). Laboratory measurements for shales, mudstones and clay aggregates vary widely, from 10^{-16} to 10^{-23} m^2 (Kwon et al., 2004 and references therein) so the flow velocities calculated using permeabilities of 1 nanodarcy (10^{-21} m^2) will be in the lower ranges of attainable fluid flux. Permeabilities of sedimentary rocks in general vary from 10^{-12} to less than 10^{-23} m^2 depending on rock type and depth (Tanikawa and Shimamoto, 2009).

Diffusion has a typical flow rate of 0.16–89 $m^3/km^2/year$ (Krooss and Leythaeuser, 1996) but it will be neglected within these calculations as it does not follow simple migration pathways (Krooss and Leythaeuser, 1996).

For the calculations CH_4 is assumed to be an ideal gas. According to the ideal gas equation 1 mole of gas at 0 °C and 1 bar (1 atm) (standard temperature and pressure conditions (STP)) is:

$$\boldsymbol{V_m = \frac{RT}{P} = \frac{8.314\ 472\ \mathrm{J\ mol^{-1}\ K^{-1}} * 273.15\ \mathrm{K}}{101.3\ kPa} = 22.41\ \mathrm{l}} \qquad \text{(Equation 5.2)}$$

Where:

V_m: Molar volume

R: Universal gas constant = 8.3145 J/mol K

T: Temperature

P: Pressure

The seafloor at survey EL0001 is located between 404-538 ms TWT which corresponds to 299-398 m using an acoustic velocity in water of 1480 m/s. One mole of gas at 350 m of seawater (approximately 3534 kPa) has a volume of:

$$\boldsymbol{V_m = \frac{RT}{P} = \frac{8.314\ 472\ \mathrm{J\ mol^{-1}\ K^{-1}} * 273.15\ \mathrm{K}}{3534\ kPa} = 0.6426\ l} \qquad \text{(Equation 5.3)}$$

Table 5.2. Fluid flux rates measured at seafloor, from literature for comparison.

Location	Averaged over	Flux CH_4 [mol m^{-2} day^{-1}]	Flux CH_4 [l m^{-2} day^{-1}] (350 m water depth)	Referance
Hydrate ridge, NW Pacific	-	Up to 200 mmol m^{-2} day^{-1}	0,129 l m^{-2} day^{-1}	(Treude, 2003)
Santa Barbara Channel, California	18 km^2 area	68 mmol m^{-2} day^{-1}	0,044 l m^{-2} day^{-1}	(Hovland et al., 1993)
Serendipity and Panama City seepage areas, Gulf of Mexico	Estimated from individual seepages	1.7 µmol-9.6 mmol m^{-2} day^{-1}	1.09-6.17*10^{-6} l m^{-2} day^{-1}	(Hovland et al., 1993)
Cape Lookout Bight, North Carolina	1 km^2 area	11.8 mmol m^{-2} day^{-1}	0,0076 l m^{-2} day^{-1}	(Hovland et al., 1993)
Offshore Bulgaria, Black Sea	Samplers at seabed	2.4-18.8 µmol m^{-2} day^{-1}	1.54*10^{-6}-1.21*10^{-5} l m^{-2} day^{-1}	(Hovland et al., 1993)
The Kattegat and the Skagerrak	100 m by 100 m	6.8-9.7 mmol m^{-2} day^{-1}	0.0044-0.0062 l m^{-2} day^{-1}	(Hovland et al., 1993)
Tommeliten field, North Sea	One individual bubble stream measured (out of 120)	8.0 mmol m^{-2} day^{-1}	0.0051 l m^{-2} day^{-1}	(Hovland and Judd, 1988; Hovland et al., 1993)
U.K. Block 15/25, North Sea	One large pockmark (640,000 m^2)	4.4 mmol m^{-2} day^{-1}	0.0028 l m^{-2} day^{-1}	(Hovland et al., 1993)

Darcy/diffuse flow is very low and is therefore almost neglectable compared to episodic fracture flow. This means a large part of the error margin within an estimation of total fluid flux (Darcy flow and fracture flow) lies in the estimation of fracture flow. The major uncertainty comes with how large the fractured areas actually are.

The potential fluid flow through the Plio-Pleistocene wedge (GI-GII) is also difficult to estimate because it is unknown how well permeable layers connect and how extensive permeable layers are. However an attempt is made to estimate potential fluid flow through the Plio-Pleistocene wedge (GI-GII). Note (Figure 4.21) that the combined area of mapped vertical fluid flow expressions through the Plio-Pleistocene sediments is 4.3 times larger than the area of fluid flow through deeper sediments (Table 4.2). The difference in area between mapped vertical fluid flow features within the Plio-Pleistocene (GI-GIII) (feature 9-30) and deeper sediments (feature 1-8) is:

$$5087259.5m^2 - 1167101.7m^2 = 3920157.8m^2 \quad \text{(Equation 5.4)}$$

This unbalance in area of the fluid flow pathways, and therefore also potentially in capacity, can be balanced by a significant lateral flow through the Plio-Pleistocene wedge (GI-GII).
The wedge is 582-961 ms TWT thick in the western edge of the 3D survey. This corresponds to 670-1105 m vertical thickness, using an acoustic velocity of 2300 m/s. The thickness is converted to the distance perpendicular to the layering (2.3° inclination);

$$Cos\ 2.3° * 670 = 669.46\ m \quad \text{(Equation 5.5)}$$

$$Cos\ 2.3° * 1105 = 1104.1\ m \quad \text{(Equation 5.6)}$$

Along with the width of the dataset (22 km) this corresponds to an approximate area of;

$$669.46 * 22000 + \left((1104.1 - 669.94) * \frac{22000}{2}\right) = 19.509\ km^2 \quad \text{(Equation 5.7)}$$

The difference in area between mapped vertical fluid flow features within the Plio-Pleistocene (GI-GIII) (feature 9-30) and deeper sediments (feature 1-8) (Equation 5.4) is 3920157.8 m^2, which corresponds to 20% of the area of the Plio-Pleistocene wedge (GI-GII):

$$\frac{3920157.8m^2}{19509000m^2} = 0.200 = 20\% \quad \text{(Equation 5.8)}$$

Assuming the same fluid flow per area in the Plio-Pleistocene wedge as in all mapped vertical fluid flow pathways, 20% of the area of the Plio-Pleistocene (GI-GII) wedge should be permeable interconnected layers. The assumption that 20% of the area are interconnected permeable layers appears to be reasonable considering the proximal location to the fans. For the following calculations exactly 20% of the area of the Plio-Pleistocene wedge will be used; 3.9018 km^2. A further assumption is that fluids are only entering the Plio-Pleistocene wedge from the west (Figure 4.5).
Three scenarios are outlined below; Scenario 1 uses typical Darcy flow rates in low permeability shales (Krooss and Leythaeuser, 1996). Scenario 2 is a higher permeability scenario (100 times that in scenario 1), considering possible silty and sandy mass movement

deposits within the Plio-Pleistocene wedge (GI-GII) and flow through possible fractured rock in the Paleocene-Miocene age sediments. Scenario 3 is an episodic flow scenario that is not sustainable over geological timescales, but a result of over-pressurized fluids.

In addition to flow through mapped vertical fluid flow pathways there may be a contribution from flow through smaller features, as well as low flux Darcy/diffusion flow through parts of the dataset not mapped as focused fluid flow pathways. It is however unlikely that gas is migrating in significant volumes through large areas of the sediment package as it has been shown that concentrations as low as a few percent of gas in sediment drastically reduce its P-wave velocity (Figure 5.12) (Domenico, 1974, 1977).

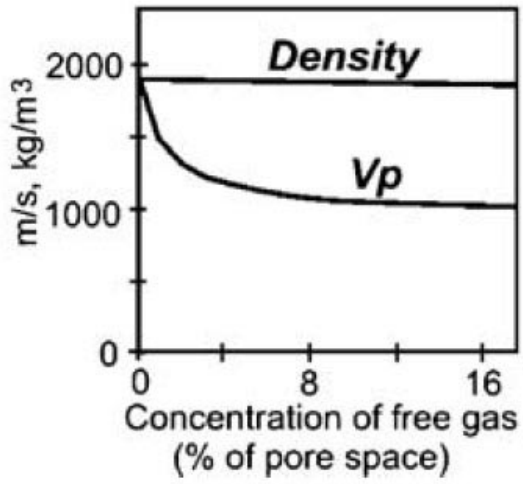

Figure 5.12. Concentration of gas versus density and P-wave velocity. From Andreassen et al. (2007a) based up on Domenico (1977)

Fluid flow outside focused fluid flow pathways is neglected in the following calculations for reasons of simplicity and lack of data. An overview of all mapped vertical fluid flow pathways is outlined in Appendix Table 1.

5.5.1 Scenario 1

In scenario 1 the assumed Darcy flow ranges from 100–1000 $m^3/km^2/year$ (Krooss and Leythaeuser, 1996) within mapped vertical fluid migration pathways. Fluid flow is assumed neglectable outside mapped fluid flow pathways. Darcy flow through all mapped fluid migration pathways creates a conceptual model (Figure 5.13). Darcy flow within the estimated 20% of the area of the Plio-Pleistocene wedge amounts to a total volume between:

$$3.90\ km^2 * 100 \frac{\frac{m^3}{km^2}}{year} = 390 \frac{m^3}{year} \quad \text{and} \qquad \text{(Equation 5.9)}$$

$$3.90\ \text{km}^2 * 1000 \frac{\frac{m^3}{\text{km}^2}}{\text{year}} = 3900 \frac{\text{m}^3}{\text{year}} \qquad \text{(Equation 5.10)}$$

The Darcy flow from mapped fluid flow pathways to the base of Pleistocene (purple, dark blue and light blue fluid migration pathways) amounts to a volume of 116-1159 m^3/year (calculations in Appendix Table 2), and through the Pleistocene succession (GIII) (green, yellow, orange and red fluid migration pathways) amounts to a volume of 509-5090 m^3/year (calculations in Appendix Table 2). Adding the fluid flux to the base of Pleistocene (fluid migration pathways through the Plio-Pleistocene wedge (GI-GII) (plus purple, dark blue and light blue migration paths) the volume adds up to:

$$390 \frac{\text{m}^3}{\text{year}} + 116 \frac{\text{m}^3}{\text{year}} = 506 \frac{\text{m}^3}{\text{year}} \quad \text{to} \qquad \text{(Equation 5.11)}$$

$$3900 \frac{\text{m}^3}{\text{year}} + 1159 \frac{\text{m}^3}{\text{year}} = 5059 \frac{\text{m}^3}{\text{year}} \qquad \text{(Equation 5.12)}$$

This model, with the majority of the fluids migrating through the Plio-Pleistocene wedge, fluids is also consistent with the frequency of mapped amplitude anomalies, with the highest concentrations in the Plio-Pleistocene wedge and sediments above it.

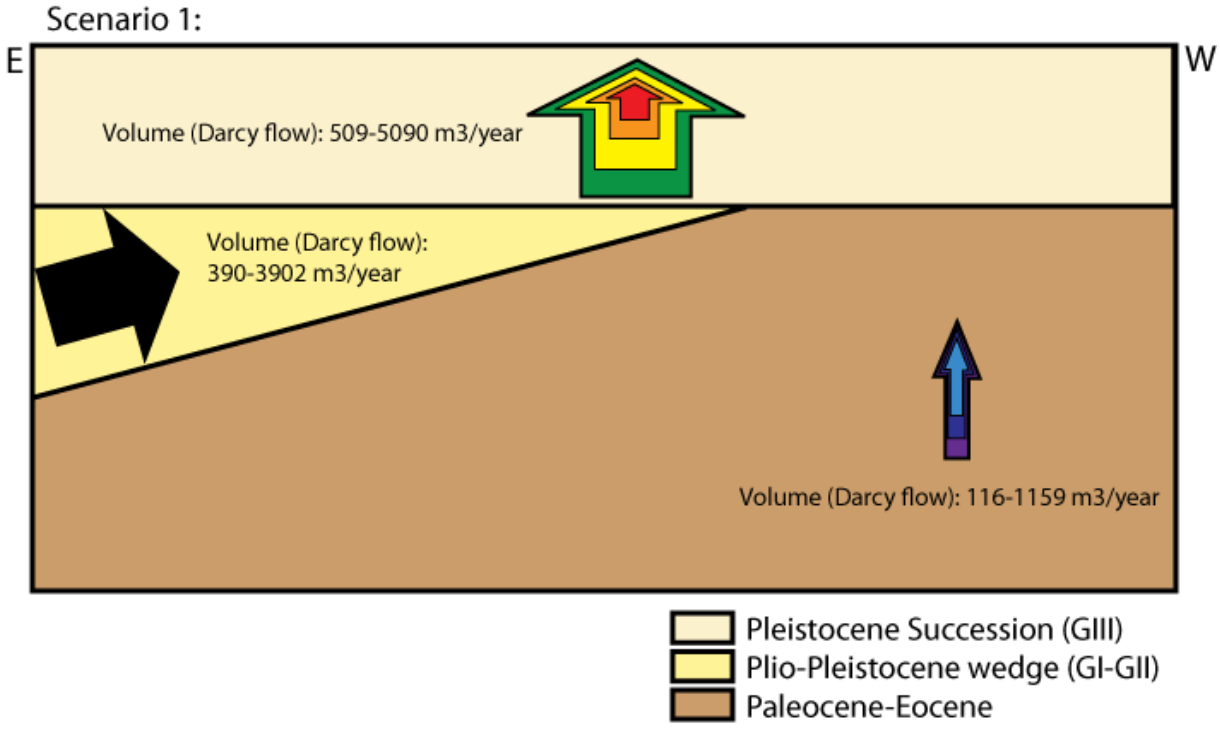

Figure 5.13. Scenario 1; Conceptual model of potential fluid volumes, assuming Darcy flow, through Paleocene-Eocene (purple, dark blue and light blue migration pathways), Plio-Pleistocene wedge (black) and Pleistocene succession (GIII) (green, yellow, orange and red migration pathways (see Figure 4.25 and

Appendix Table 1)) using typical Darcy flow rates (Roberts and Nunn, 1995; Krooss and Leythaeuser, 1996). Widths of arrows represent relative fluid flux volume.

5.5.2 Scenario 2

Most of the sediments are marine shales which presumably have low permeabilities (10^{-16} to 10^{-23} m^2 (Kwon et al., 2004 and references therein)). However, vertical fluid flow features within the Tertiary sediments appear to be associated with faults. They may increase the permeability and thereby increasing fluid flux through Paleocene-Miocene age sediments. Sediments within the Plio-Pleistocene wedge (GI-GII) and the Pleistocene succession (GIII) may have coarser sediments with higher permeabilities then the shales discussed in scenario 1.

Scenario 2 is similar to scenario 1, but permeabilities and therefore fluid fluxes, have been increased (multiplied with 100) to 0.1 μD. According to Darcy's law (equation 1.1) a permeability increase of 100 times gives a potential fluid flux increase of the same amount. Therefore fluid fluxes in scenario 2 is calculated at 10 000–100 000 m3/km2/year. Fluid flow is assumed neglectable outside mapped fluid flow pathways. Calculated fluid fluxes are shown in Appendix Table 3. The fluid flux volume relationship is the same as in scenario 1. The only consequence of higher fluid fluxes is that of possible escape of methane to the water column, this will be discussed in section 5.5.4.

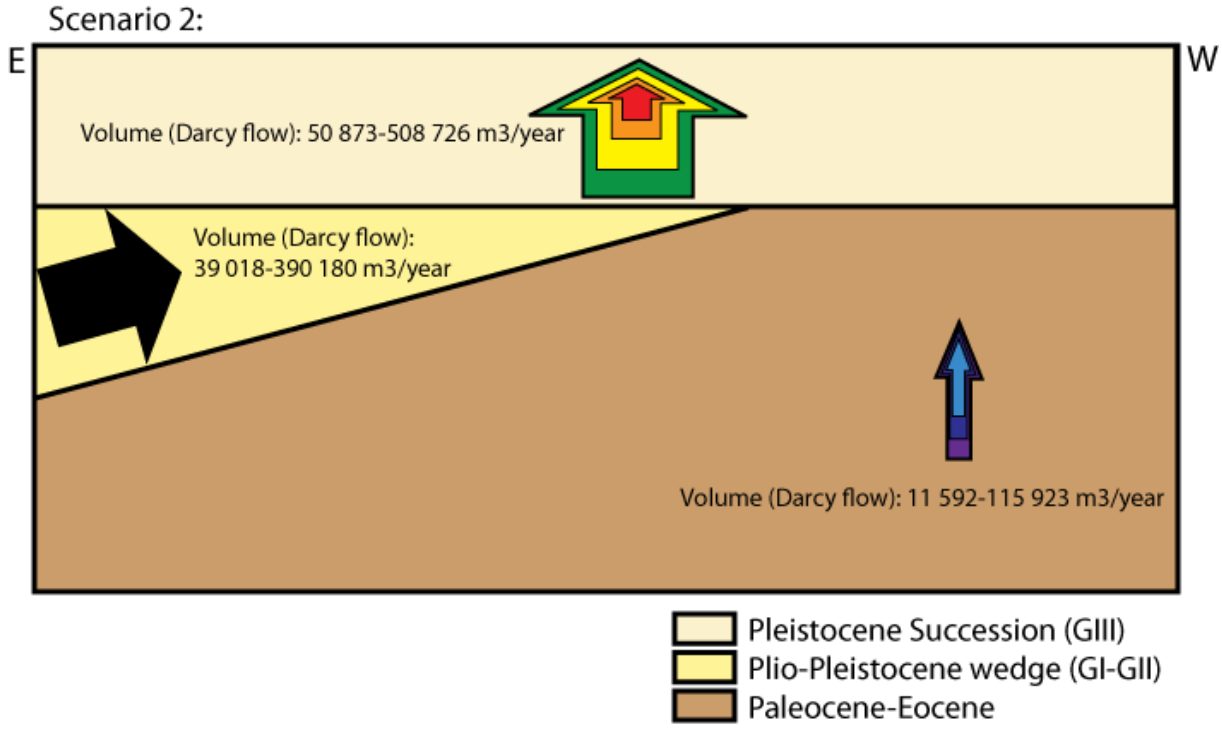

Figure 5.14 Scenario 2; Schematic sketch of potential fluid volumes, assuming all Darcy flow, but this time 100 times greater than in scenario 1, thorough Paleocene-Eocene (purple, dark blue and light blue migration pathways), Plio-Pleistocene wedge (black) and Pleistocene succession (GIII) (green, yellow,

orange and red migration pathways). Widths of arrows are representative of their fluid flux volume relationship.

5.5.3 Scenario 3

In scenario 3 fracture flow ($2*10^8$–$2.5*10^9$ m^3/km^2/year in episodic events (Roberts and Nunn, 1995)) is assumed through vertical fluid flow pathways associated with faults (Feature 1, 3, 4, 5 and 6) and all other fluid flow pathways including 20% of the Plio-Pleistocene wedge, are assumed to feature Darcy flow of 10 000–100 000 m^3/km^2/year. Fluid flow is assumed neglectable outside mapped fluid flow pathways.

Feature 1, 3, 4, 5 and 6 suggest fluid migration associated with small faults (Figure 4.23 and Figure 4.24). The throws of the faults are approximately 15 to 25 m. Fault cores often act as conduits for fluid flow during deformation processes but afterwards fault cores may become cemented which can result in low permeability. The damage zone often tends to be a conduit compared to both the fault core and the protholith (Caine, 1996), but the damage zone does not display a linear correlation to the displacement of the fault (Childs et al., 2009). Damage zone thicknesses seem to be created at small throws and do not grow in direct proportion to the displacement (Childs et al., 2009). According to data gathered by Childs et al. (2009), faults with throws of magnitudes observed in the study area (15-25 m) show damage zones of approximately 0.1 to 3(10) m (Figure 5.15). Based on these observations, a conservative estimation of 0.5 m is assumed for our calculations. It is combined with the width of the features from Appendix Table 1.

The collective potential gas volume from the mapped fluid migration pathways up to Pleistocene (purple, dark blue and light blue fluid migration pathways) is estimated to between $1.35*10^5$ m^3/year and $1.66*10^6$ m^3/year in episodic events (see Appendix Table 4).

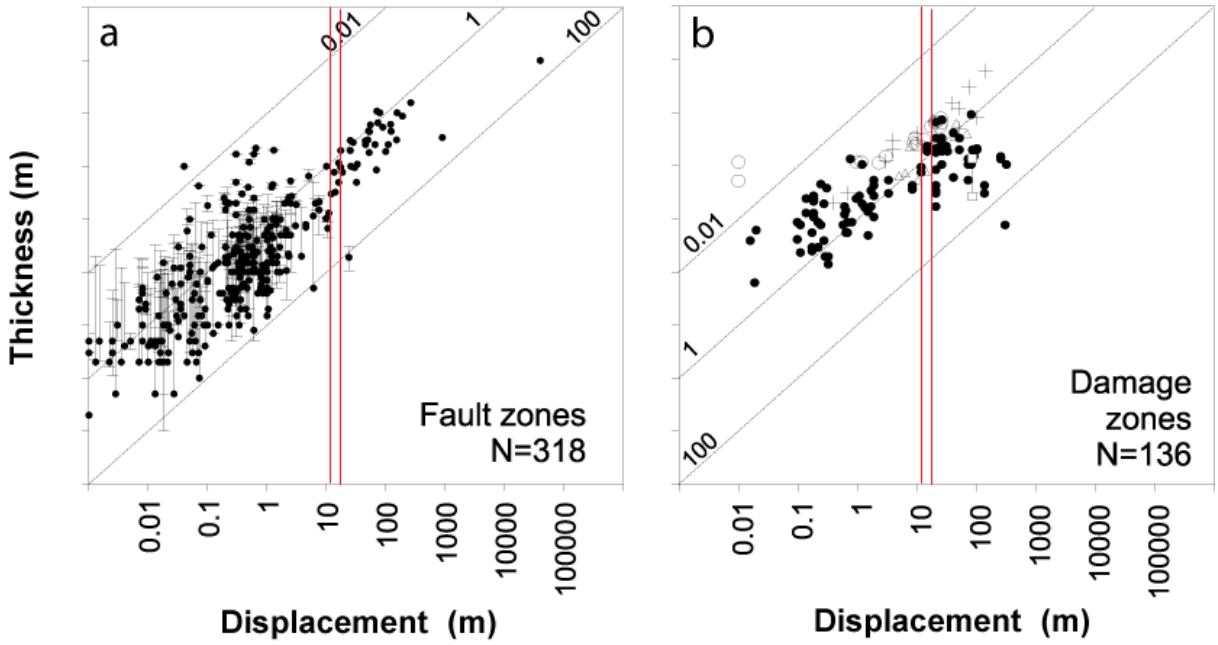

Figure 5.15. Thickness (logarithmic scale) plotted against fault displacement (x axis) for a) Fault zone width and b) damage zone width. The two red lines mark the range of displacement of the faults in question (between 15 and 25 m in the x axis). Values of damage zone widths between the red lines range from approximately 0.1 to 3 m in the logarithmic scale shown in figure b. From Childs et al. (2009).

Assuming flow flux of 10 000–100 000 m3/km2/year within the permeable interconnected layers of the Plio-Pleistocene wedge, this would correspond to a potential volume of between:

$$3.9018\ km^2 * 10\ 000\ \frac{\frac{m^3}{\mathrm{km^2}}}{\mathrm{year}} = 39\ 018\ \frac{\mathrm{m^3}}{\mathrm{year}} \quad \text{and} \qquad \text{(Equation 5.13)}$$

$$3.9018\ \mathrm{km^2} * 100\ 000\ \frac{\frac{m^3}{\mathrm{km^2}}}{\mathrm{year}} = 390\ 180\ \frac{\mathrm{m^3}}{\mathrm{year}} \qquad \text{(Equation 5.14)}$$

The collective potential vertical fluid flux through the Pleistocene succession (fluid migration pathways green, yellow, orange and red), assuming Darcy flow, amounts to a volume between 50 873-508 726 m^3/year (see calculations in Appendix Table 4). In addition to this come episodic discharges of fluids, both though the Plio-Pleistocene wedge and the faults in Cretaceous and Tertiary sediments, which may multiply the values many times. A fluid flux this high is not sustainable over geological time, rather until the overpressures causing the episodic discharges are equalized.

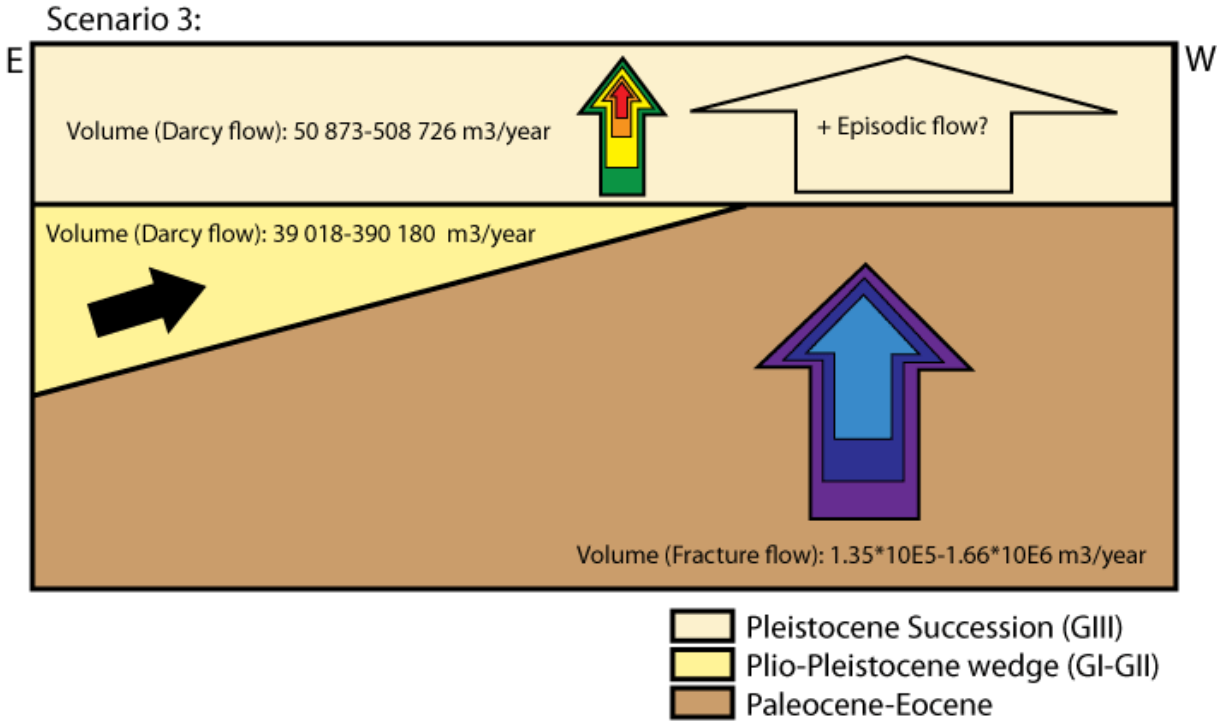

Figure 5.16. Scenario 3; Schematic sketch of potential fracture fluid volumes thorough Paleocene-Eocene (purple, dark blue and light blue migration pathways), Darcy flow through Plio-Pleistocene wedge (black) and Darcy flow with possible episodic flow through the Pleistocene succession (GIII) (green, yellow, orange and red migration pathways) using typical flow rates (Roberts and Nunn, 1995; Krooss and Leythaeuser, 1996). Widths of arrows are representative of their fluid flux volume relationship.

As mentioned before, fracture flow is often episodic. Large volumes of fluids can be transported through a fractured seal during short-lived expulsion events. Averaged over geological time flow is likely to be much lower because otherwise fluid fluxes on a larger scale would be much too high. It is common for fluid pressures to build up higher than hydrostatic pressures in shale-rich sedimentary basins (Bethke, 1986; Hunt, 1990). When the pressure exceeds 85% of the lithostatic pressure fractures opens the seal. The increase in pressure that reaches the fracture criteria is a process that takes 10 000 to 500 000 years (Roberts and Nunn, 1995). Fractures in relatively incompressible rocks, such as cemented or compacted sediments, typically remain open for 20-50 years. Fractures in unconsolidated sediments like the shallowest Pleistocene sediments will remain open for even shorter periods. The episodic flow event is likely to create large accumulations of fluids under and within the Pleistocene succession but this was not observed in the study area. Pressure build up beneath the URU could form self enhanced pipes. These pipes would create fluid flow pathways to the seafloor and could transport gas during short lived expulsion events.

Overpressure may have existed in basins both to the E and W of Veslemøy High which may have produced episodic flow and self-enhanced fluid migration pathways.

When applying Darcy flow throughout as a fluid flow mechanism the ratios of flow beneath the Pleistocene succession (GIII) is very similar to the ratios of flow within the fluid flow pathways in the Pleistocene succession (flow beneath the Pleistocene succession (GIII) equals 99.4% of flow within the Pleistocene succession (GIII)). The volume relationship of flow from the western and eastern basins respectively is consistent with the frequency of brightspots observed in the 3D survey. Most fluids are likely to come from western basins through the Plio-Pleistocene wedge, 77% in scenario 1 and 2. If overpressure builds up from fluids in the eastern basins and these are released in episodic expulsive events the proportions may be reversed with the dominant fluid fluxes from the eastern basins.

The suggested fracture flow in the area is likely to be episodic. The extremely high rates of flux through episodic discharge through faults in Paleocene-Eocene are likely to be compensated by self enhanced fractures and pipes through the Pleistocene succession. Otherwise enormous volumes of gas would accumulate beneath the URU reflector, of which there is no sign. At Veslemøy High it seems more likely that the flow mechanism within the mapped fluid flow features is Darcy flow, through areas with enhanced permeabilities.

5.5.4 Fluid leakage into the water column

Fluids seeping into the water column along the margin west of Veslemøy High contain methane showing both thermogenic and biogenic origin (Lein et al., 1999). Methane is the second most important greenhouse gas and accounts for 15–20% of the radiative forcing added to the atmosphere (IPCC, 1996). As methane migrates upwards a major barrier for gas flux are the gas hydrate stability zones where hydrate may form. If methane leaves the stability zone anaerobic oxidation of methane (AOM) retains most of the methane in the seabed. AOM is a microbial process in anoxic marine sediments, which uses sulphate instead of oxygen as an electron receptor (Treude et al., 2003). It has been found that AOM in the top 20 cm of surface sediments drastically reduce the methane being released to the water column by approximately 0.15 1 m^{-2} day^{-1} (Lein et al., 2000). Carbon dioxide which is oxidized from methane is forms carbonate illite-calcite-barite chimneys, crusts, and nodules (Treude et al., 2003). Even if methane reaches the water column it will be aerobically oxidized by proteobacteria (Madigan et al., 2000), and dissolved and diluted within the water column (Judd et al., 2002). The biota of the water column consumes methane and incorporates it into

its biomass. In doing so they effectively act as a filter to prevent or at least inhibit the movement of methane into the atmosphere (Joye et al., 2005).

A good example of the methane consumption processes is the Haakon Mosby Mud Volcano (HMMV) on the SW Barents Sea slope. At the HMMV, methane is rapidly oxidized, dissolved, and diluted by bottom currents in the water column, at rates as great as 48.5 nl CH_4 l^{-1} day^{-1} (Lein et al., 2000). This is probably occurring in most areas of active methane venting. However, methane is traceable in seawater 800 m above the HMMV (Damm and Budeus, 2003). At Veslemøy High the water depths are only 300-400 m, which is one third of the water depth at HMMV. It is possible that high rates of fluid flux allow methane to be released to the atmosphere. The main effect of the methane released into the water column is indirect, in that it reduces the sink capacity of the water masses for atmospheric methane, which indirectly leads to higher concentrations of methane in the atmosphere.

It has been suggested that at the HMMV direct release of methane into seawater only takes place in the warm central caldera. Here, high geothermal gradient prevents formation of gas hydrates or bacterial mat formation within sediments (Damm and Budeus, 2003).

I will now discuss the three different scenarios outlined above.

In scenario 1 only Darcy flow is assumed, at leakage velocities of 100–1000 m3/km2/year (Krooss and Leythaeuser, 1996) corresponding to 0.00027-0.0027 l m^{-2} day^{-1}. Anaerobic oxidation of methane in the top 20 cm of surface deposits can reduce the methane being released into the water column by approximately 0.15 1 m^{-2} day^{-1} (Lein et al., 2000). Therefore, no methane should escape into the water column, since it will all be oxidized and consumed by sulphate reducing bacteria, no effect on green house gas concentrations is to be considered.

In scenario 2 fluid fluxes may reach 0.027-0.27 l m^{-2} day^{-1} where the fluid flow pathways exit on the seafloor. Considering anaerobic oxidation of methane in the top 20 cm of surface deposits of 0.15 1 m^{-2} day^{-1} (Lein et al., 2000) a maximum of 0.12 1 m^{-2} day^{-1} of methane may remain (compare with Table 5.2). At Hydrate ridge, off Oregon, USA, AOM rates up to 5 μmol cm^{-3} d^{-1} exist (Treude, 2003) indicating that AOM rates are higher in areas of high methane flux (Treude, 2003). Measurements at the Hydrate Ridge have also demonstrated that even at the highest methane fluxes of 200 mmol m^{-2} day^{-1} (0.13 l m^{-2} day^{-1} at 36 atm), between 50-90 % of the methane is consumed by anaerobic oxidation. Fluid flux at Veslemøy High may be lower or higher than the flux recorded at the Hydrate Ridge.

Even if these fluid fluxes were to occur at Veslemøy High, any methane leaking into the water column will rapidly be aerobically oxidized, dissolved and diluted. Due to the relatively large water depth of Arctic shelves, methane releases are not very likely to reach the water air interface and thus will have no direct influence on the greenhouse gases and climate. An increased concentration of methane in the water column may however, as previously mentioned, reduce the sink capacity of the water masses for atmospheric methane and have an indirect effect on the greenhouse gas concentrations in the atmosphere.

Only scenario 3 offers the high flux fluid flow mechanism needed for methane to escape into the water column and further into the atmosphere. Fracture fluid flow within Tertiary sediments may have built up overpressures beneath the Pleistocene sediments. The overpressures may have created fractures. Fractures in glacially consolidated sediments like the shallow Pleistocene sediments are likely to remain open for short periods only. In addition the rapid sedimentation west of Veslemøy High in glacial periods may have produced additional overpressures. The rapid increases in overpressure may have led to episodic discharges with high flux rates (Hustoft et al., in press).

Episodic fracture flow may have produced methane flow rates that are high enough to escape to the water column at rates between 550-6850 1 m^{-2} day^{-1} (Roberts and Nunn, 1995). The high fluid flux rates in areas with over-pressurized fluids may create pipes and major fractured fluid flow pathways.

High fluid flux rates during expulsive events are likely to produce seafloor fluid escape features such as pockmarks. Even though the assumed rates are high they are much lower than at vent sites on ocean ridges, for example at Mohns Ridge near Jan Mayen. Here, flow rates at a smoker plume were approximately ½ m/s (Schultz et al., 2005), corresponding to $4.32*10^7$ l m^{-2} day^{-1}.

Depressions found on the seafloor interpreted to be pockmarks are large features, with an area of up to 780 000 m^2 (Table 4.3). The requirements for pockmark formation have not been fully understood yet as their formation and dynamics are still poorly constrained.

The existence of ploughmarks within the pockmarks suggests they have been formed after the last deglaciation when sea level was suitable for iceberg scouring. Rapid deglaciation of the Barents Sea Ice Sheet started at about 15 ka (Jones and Keigwin, 1988; Vorren and Laberg, 1996; Landvik et al., 1998). The latest period of intense iceberg scouring in the SW Barents Sea is not constrained but Lien (1983) has done thorough research on the timing of

ploughmarks on the Norwegian shelf. He came to the conclusion that the formation of ploughmarks must have ended about 12.5-11.5 ka.

This leaves a time span of 2500-3500 years for the formation of the pockmarks. Assuming non-explosive fluid leakage with sediment suspension as function this would indicate 6.54-9.16 mm (22.9 m/3500 yr to 22.9 m/2500 yr) of fine-grained sediments per year being suspended from within the pockmark. It cannot be excluded that Darcy flow leakage of under 0.27 l m^{-2} day^{-1} (minus the methane trapped as gas hydrates and bound within carbonate), as in scenario 2, could be able to remove a net sum of 6.54-9.16 mm of fine-grained sediments per year. But if fine-grained sediments were to be suspended from the poorly sorted glacial sediments which constitutes the seabed (Fiedler and Faleide, 1996), a lag deposit of coarser sediments would be left behind and hinder further deepening of the pockmark, long before it reaches a depth of over 22 m. A higher energy outflow of fluids over a short period of time appears as a more likely forming mechanism.

6 CONCLUSIONS

- Fluids migrate into Veslemøy High primarily from the basins in the west (Sørvestsnaget Basin) and east (Tromsø Basin). There are no or limited indications of fluid migration from directly below Veslemøy High.
- Fluid migration through the Cretaceous to Miocene is associated with lateral migration along strata from eastern basins and vertical migration through N-S trending small throw faults.
- Fluids predominantely (estimated at ¾) migrate into Veslemøy High through the Plio-Pleistocene wedge (GI-GII) from the western basins.
- Fluid migration through the Pleistocene succession (GIII) is associated with vertical migration through focused self enhanced fluid flow pathways.
- Overpressure may result from rapid sedimentation in the Bjørnøya Through Mouth Fan during glacial times. The slope strata may provide lateral fluid migration pathways that connect the Veslemøy High with the deep basins. At times of overpressure episodic discharges with high fluid flux rates may have occurred, creating pipes and pockmarks at Veslemøy High.
- Higher fluid flux rates then at present are likely to have existed in between the retreat of the icesheet (15 ka) and 12.5-11.5 ka that triggered seabed fluid flow expulsions documented in pockmarks.
- At low flux rates (Darcy flow) gas migrating into Veslemøy High may not escape to the water column and have no direct effect on climate. Episodic expulsive events may however release enough gas for it to escape into the atmosphere and have a direct effect on climate.
- Pockmarks are formed in association with the deglaciation events and the fluid expulsion events were violent enough to remove up to 22 m of glaciomarine sediments.

7 REFERENCES

Allan, J.R., Sun, S.Q. and Trice, R., 2006. The deliberate search for stratigraphic and subtle combination traps; where are we now? In: R. Allen Matthew, P. Goffey Graham, K. Morgan Richard and M. Walker Ian (Editors), Geological Society Special Publications. Geological Society of London, London, United Kingdom, pp. 57-103.

Andreassen, K., Hogstad, K. and Berteussen, K.A., 1990. Gas hydrate in the southern Barents Sea, indicated by a shallow seismic anomaly. First Break, 8: 235-245.

Andreassen, K., Laberg, J.S. and Vorren, T.O., 2008. Seafloor geomorphology of the SW Barents Sea and its glaci-dynamic implications. Geomorphology, 97(1-2): 157-177.

Andreassen, K., Nilssen, E. and Ødegaard, C., 2007a. Analysis of shallow gas and fluid migration within the Plio-Pleistocene sedimentary succession of the SW Barents Sea continental margin using 3D seismic data. Geo-Marine Letters, 27(2): 155-171.

Andreassen, K., Nilssen, L.C., Rafaelsen, B. and Kuilman, L., 2004. Three-dimensional seismic data from the Barents Sea margin reveal evidence of past ice streams and their dynamics. Geology (Boulder), 32(8): 729-732.

Andreassen, K., Ødegaard, C.M. and Rafaelsen, B., 2007b. Imprints of former ice streams, imaged and interpreted using industry three-dimensional seismic data from the southwestern Barents Sea. Geological Society, London, Special Publications, 277: 151-169.

Avseth, P., Mukerji, T. and Gary, M., 2005. Quantitative seismic interpretation - Applying rock physics tools to reduce interpretation risk. Cambridge University Press, Cambridge, 359 pp.

Aydin, A., 2000. Fractures, faults, and hydrocarbon entrapment, migration and flow. Marine and Petroleum Geology, 17: 797-814.

Bacon, M., Simm, R. and Redshaw, T., 2003. 3-D Seismic Interpretation. Cambridge University Press, Cambridge, 225 pp.

Bahorich, M.S. and Farmer, S.L., 1995. 3D seismic discontinuity for faults and stratigraphic features: The coherence cube: Expanded Abstracts, 65th Annual International Meeting, SEG, pp. 93–96.

Barnes, A.E., 2007. Redundant and useless seismic attributes. GEOPHYSICS, VOL. 72(3): 33-38.

Bellec, V. et al., 2008. Bottom currents interpreted from iceberg ploughmarks revealed by multibeam data at Tromsøflaket, Barents Sea. Marine Geology, 249(3-4): 257-270.

Berndt, C., 2005. Focused fluid flow in passive continental margins. Phil. Trans. R. Soc. A, 363: 2855-2871.

Berndt, C., Bünz, S. and Mienert, J., 2003. Polygonal fault systems on the Mid-Norwegian margin: a long-term source for fluid flow. In: P.V. Rensbergen, R. Hillis, A. Maltman and C. Morley (Editors), Subsurface Sediment Mobilization. Geological Society, Special Publication, London, pp. 283-290.

Bethke, C.M., 1986. Inverse hydrologic analysis of the distribution and origin of gulf coast-type geopressured zones. Journal of Geophysical Research, 91: 6535-6545.

Bjørkum, P.A. and Nadeau, P.H., 1998. Temperature controlled porosity/permeability reduction, fluid migration, and petroleum exploration in sedimentary basins. Aust. Pet. Prod. & Expl. Assoc. Journal, 38: 453-464.

Breivik, A.J., Faleide, J.I. and Gudlaugsson, S.T., 1998. Southwestern Barents Sea margin; late Mesozoic sedimentary basins and crustal extension. Tectonophysics, 293: 1-2.

Brekke, H. and Riis, F., 1987. Tectonics and basin evolution of the Norwegian shelf between 62 degrees N and 72 degrees N. Norsk Geologisk Tidsskrift(67): 295-321.

Brown, A.R., 1999. Interpretation of three-dimensional seismic data.

Bruhn, R.L., Parry, W.L., Yonkee, W.A. and Thomson, T., 1994. Fracturing and hydrothermal alteration in normal fault zones. Pure and Applied Geophysics, 142: 609-644.

Bulat, J., 2005. Some considerations on the interpretation of seabed images based on commercial 3D seismic in the Faroe-Shetland Channel. Basin Research, 17(1): 21-42.

Buswell, A.M. and Mueller, H.F., 1952. Mechanism of Methane Fermentation. Industrial & Engineering Chemistry, 44(3): 550-552.

Bünz, S. and Mienert, J., 2004. Acoustic imaging of gas hydrate and free gas at the Storegga Slide. J. Geophys. Res., 109.

Bünz, S., Mienert, J. and Berndt, C., 2003. Geological controls on the Storegga gas-hydrate system of the mid-Norwegian continental margin. Earth and Planetary Science Letters, 209(3-4): 291-307.

Caine, J.S., Evans, J.P., Forster, C.B., 1996. Fault zone architechture and permeability structure. Geology, 24(11): 1025-1028.

Carstens, H., 2005. Gas found in glacial, shallow sands. GEO ExPro, 2(4): 24-25.

Cartwright, J., Huuse, M. and Aplin, A., 2007. Seal bypass systems. AAPG Bulletin, 91(8): 1141-1166.

Cavanagh Andrew, J., Di Primio, R., Scheck Wenderoth, M. and Horsfield, B., 2006. Severity and timing of Cenozoic exhumation in the southwestern Barents Sea. Journal of the Geological Society, 163(5): 761.

Chand, S. et al., 2008. Gas hydrate stability zone modelling in areas of salt tectonics and pockmarks of the Barents Sea suggests an active hydrocarbon venting system. Marine and Petroleum Geology, 25(7): 625-636.

Chester, F.M. and Logan, J.M., 1986. Implications for mechanical properties of brittle faults from observations of the Punchbowl fault zone, California. Pure and Applied Geophysics, 124(1-2): 79-106.

Childs, C. et al., 2009. A geometric model of fault zone and fault rock thickness variations. Journal of Structural Geology, 31(2): 117-127.

Clark, J.D. and Pickering, K.T., 1996. Submarine Channels - Processes and Architecture. Vallis Press, London, 231 pp.

Crutchley, G.J., Pecher, I.A., Gorman, A.R., Henrys, S.A. and Greinert, J., in press. Seismic imaging of gas conduits beneath seafloor seep sites in a shallow marine gas hydrate province, Hikurangi Margin, New Zealand. Marine Geology: 13pp.

Dalland, A., Worsley, D., Ofstad, K., 1988. A lithostratigraphic scheme for the Mesozoic and Cenozoic succession offshore mid- and northern Norway. Norw. Pet. Dir. Bull. 4: 65 p.

Damm, E. and Budeus, G., 2003. Fate of vent-derived methane in seawater above the Hakon Mosby mud volcano (Norwegian Sea). Marine Chemistry, 82: 1-2.

Davison, I., Alsop, G.I., Evans, N.G. and Safaricz, M., 2000. Overburden deformation patterns and mechanisms of salt diapir penetration in the Central Graben, North Sea. Marine and Petroleum Geology, 17(5): 601-618.

Domenico, S.N., 1974. Effect of water saturation on seismic reflectivity of sand reservoirs encased in shale. Geophysics, 39(6): 759-769.

Domenico, S.N., 1977. Elastic properties of unconsolidated porous sand reservoirs. Geophysics, 42(7): 1339-1368.

Doré, A.G., 1995. Barents Sea Geology, Petroleum Resources and Commercial Potential. Arctic, 48(3): 207–221.

Duranti, D. and Hurst, A., 2004. Fluidization and injection in the deep-water sandstones of the Eocene Alba Formation (UK North Sea). Sedimentology, 51(3): 503-529.

Eidvin, T. and Riis, F., 1989. Nye dateringer av de tre vestligste borhullene i Barentshavet. Resultater og konsekvenser for den tertiaere hevingen. Nor. Pet. Director. Contrib., , 27: 27, 44 pp.

Evans, J.P., Forster, C.B. and Goddard, J.V., 1997. Permeability of fault-related rocks, and implications for hydraulic structure of fault zones. Journal of structural Geology, 19: 1393-1404.

Faleide, J.I., Gudlaugsson, S.T. and Jacquart, G., 1984. Evolution of the western Barents Sea. Marine and Petroleum Geology, 1(May): 123-150.

Faleide, J.I., Gudlaugsson, S.T., Eldholm, O., Myhre, A.M., Jackson, H.R., 1991. Deep seismic transects across the sheared western Barents Sea – Svalbard continental margin. . Tectonophysics, 189: 73–89.

Faleide, J.I., Myhre, A.M. and Eldholm, O., 1988. Early Tertiary volcanism at the western Barents Sea margin. Early Tertiary volcanism and the opening of the NE Atlantic. London GBR United Kingdom. Mar. Geological Society of London London United Kingdom.

Faleide, J.I. et al., 1996. Late Cenozoic evolution of the western Barents Sea-Svalbard continental margin. Global and Planetary Change, 12(1-4): 53-74.

Faleide, J.I. et al., 2008. Structure and evolution of the continental margin off Norway and the Barents Sea. Episodes, 31: 82-91.

Faleide, J.I., Vagnes, E. and Gudlaugsson, S.T., 1993. Late Mesozoic-Cenozoic evolution of the south-western Barents Sea in a regional rift-shear tectonic setting. Marine and Petroleum Geology, 10(3): 186-214.

Fertl, W.H., 1976. Abnormal Formation Pressures. Elsevier, Amsterdam.

Fiedler, A. and Faleide, J.I., 1996. Cenozoic sedimentation along the southwestern Barents Sea margin in relation to uplift and erosion of the shelf. Global and Planetary Change, 12(1-4): 75-93.

Fisher, Q.J., Casey, M., Harris, S.D. and Knipe, R.J., 2003. Fluid-flow properties of faults in sandstone; the importance of temperature history. Geology (Boulder), 31(11): 965-968.

Fleischer, P., Orsi, T.H., Richardson, M.D. and Anderson, A.L., 2001. Distribution of free gas in marine sediments: a global overview Geo-Marine Letters, 21(2 September): 103-122.

Gabrielsen, R.H., Færseth, R.B., Jensen, L.N., Kalheim, J.E. and Riis, F., 1990. Structural elements of the Norwegian continental shelf, Part I. The Barents Sea Region. Norwegian Petroleum Directorate Bulletin, 6: 33 pp.

Gay, A. et al., 2006. Isolated seafloor pockmarks linked to BSRs, fluid chimneys, polygonal faults and stacked Oligocene-Miocene turbiditic palaeochannels in the Lower Congo Basin. Marine Geology, 226(1-2): 25-40.

Gudlaugsson, S.T., Faleide, J.I., Johansen, S.E. and Breivik, A.J., 1998. Late Palaeozoic structural development of the South-western Barents Sea. Marine and Petroleum Geology, 15(1): 73-102.

Gölke, M. and Brudy, M., 1996. Orientation of crustal stresses in the North Sea and Barents Sea inferred from borehole breakouts. Tectonophysics, 266(1-4): 25-32.

Gölke, M. and Coblentz, D., 1996. Origins of the European regional stress field. Tectonophysics, 266(1-4): 11-24.

Hansen, J.P.V., Cartwright, J.A., Huuse, M. and Clausen, O.R., 2005. 3D seismic expression of fluid migration and mud remobilization on the Gjallar Ridge, offshore mid-Norway. Basin Research, 10: 1365-2117.

Heggland, R., 1997. Detection of gas migration from a deep source by the use of exploration 3D seismic data. Marine Geology, 137(1-2): 41-47.

Heggland, R., 1998. Gas seepage as an indicator of deeper prospective reservoirs; a study based on exploration 3D seismic data. Marine and Petroleum Geology, 15(1): 1-9.

Hickman, S., Sibson, R.H. and Bruhn, R., 1995. Introduction to special section; Mechanical involvement of fluids in faulting. Journal of Geophysical Research, B, Solid Earth and Planets, 100(7): 12,831-12,840.

Hjelstuen, B.O., Eldholm, O. and Skogseid, J., 1999. Cenozoic evolution of the northern Vøring margin. Geological Society of America Bulletin, 111(12): 1792-1807.

Hovland, M., 1981. Characteristics of pockmarks in the Norwegian Trench. Marine Geology, 39: 103-117.

Hovland, M., 1982. A coast-parallel depression, possibly caused by gas migration, off Western Norway. Mar. Geol., 50: 11-20.

Hovland, M., Gardner, J.V. and Judd, A.G., 2002. The significance of pockmarks to understanding fluid flow processes and geohazards. Geofluids, 2(2): 127-136.

Hovland, M. and Judd, A.G., 1988. Seabed pockmarks and seepages: Impact on geology, biology and the marine environment. Graham & Trotman Ltd., London, 293 pp.

Hovland, M., Judd, A.G. and Burke Jr, R.A., 1993. The global flux of methane from shallow submarine sediments. Chemosphere, 26(1-4): 559-578.

Hovland, M. et al., 2005. Complex pockmarks with carbonate-ridges off mid-Norway: Products of sediment degassing. Marine Geology, 218(1-4): 191-206.

Hunt, J.M., 1990. Generation and migration of petroleum from abnormally pressured fluid compartments. AAPG Bulletin, 74(1): 1-12.

Hustoft, S., Dugan, B. and Mienert, J., in press. Effects of rapid sedimentation on developing the Nyegga pockmark-field; constraints from hydrological modeling and 3D seismic data, offshore mid-Norway. Geochemistry, Geophysics, Geosystems (G-cubed).

Hustoft, S., Mienert, J., Bünz, S. and Nouzé, H., 2007. High-resolution 3D-seismic data indicate focussed fluid migration pathways above polygonal fault systems of the mid-Norwegian margin. Marine Geology, 245(1-4): 89-106.

Huuse, M. et al., 2004. Seismic characteristics of large-scale sandstone intrusions in the Paleogene of the south Viking Graben, UK and Norwegian North Sea. Memoirs of the Geological Society of London, 29

263-277.

IPCC, 1996. International Panel on Climate Change, Climate Change 1995. The Science of Climate Change, XII. Cambridge University Press, Cambridge (UK).

Jakobsson, M. et al., 2008. An improved bathymetric portrayal of the Arctic Ocean: Implications for ocean modeling and geological, geophysical and oceanographic analyses. Geophysical Research Letters, , 35.

Johansen, S.E. et al., 1993. Hydrocarbon potential in the Barents Sea region; play distribution and potential. In: T.O. Vorren et al. (Editors), Arctic geology and petroleum potential, Norwegian Petroleum Society special publ. . Elsevier New York International.

Jolly, R.J.H. and Lonergan, L., 2002. Mechanisms and controls on the formation of sand intrusions. Journal of the Geological Society, 159: 605-617.

Jones, G.A. and Keigwin, L.D., 1988. Evidence from Fram Strait (78”) for early deglaciation. . Nature(336): 56-59.

Joye, S., Boetius, A., Montoya, J., Niemann, H. and Orcutt, B., 2005. Water column methane oxidation in the vicinity of benthic methane seeps in the North Sea and Gulf of Mexico. www.cosis.net/abstracts/EGU05/01657/EGU05-A-01657.pdf, European Geosciences Union.

Judd, A., Hovland, M., 2007. Seabed Fluid Flow. Cambridge University Press.

Judd, A.G., Hovland, M., Dimitrov, L.I., Gil, S.G. and Jukes, V., 2002. The geological methane budget at Continental Margins and its influence on climate change. Geofluids(2): 109-126.

King Lewis, H. and MacLean, B., 1970. Pockmarks on the Scotian shelf. Geological Society of America Bulletin, 81(10): 3141-3148.

Kjemperud, A. and Fjeldskaar, W., 1992. Pleistocene glacial isostasy - implications for petroleum geology. . In: R.M. Larsen, H. Brekke, B.T. Larsen and E. Talleraas (Editors), Tectonic modelling and its application to petroleum geology. Norwegian Petroleum Society Spec Publ 1. Elsevier, Amsterdam, pp. 187–195.

Knutsen, S.-M., Harald Augustson, J., Haremo, P., Kari Ofstad, J.E.K. and Alexander-Marrack, P., 2000. Exploring the Norwegian part of the Barents Sea--Norsk Hydro's lessons from nearly 20 years of experience, Norwegian Petroleum Society Special Publications. Elsevier, pp. 99-112.

Knutsen, S.-M. and Vorren, T.O., 1991. Early Cenozoic sedimentation in the Hammerfest Basin. Marine Geology, 101(1-4): 31-48.

Knutsen, S.G., Skjold, L.J. and Skott, P.H., 1992. Palaeocene and Eocene development of the Tromso Basin sedimentary response to rifting and early sea-floor spreading in the Barents Sea area. Norsk Geologisk Tidsskrift, 72(2): 191-207.

Krooss, B.M. and Leythaeuser, D., 1996. Molecular diffusion of light hydrocarbons in sedimentary rocks and its role in migration and dissipation of natural gas. In: D. Schumacher and A. Abrams Michael (Editors), AAPG Memoir. 66. American Association of Petroleum Geologists Tulsa OK United States., pp. 173-183.

Kwon, O., Kronenberg Andreas, K., Gangi Anthony, F., Johnson, B. and Herbert Bruce, E., 2004. Permeability of illite-bearing shale; 1, Anisotropy and effects of clay content and loading. Journal of Geophysical Research, 109.

Laberg, J.S. and Andreassen, K., 1996. Gas hydrate and free gas indications within the Cenozoic succession of the Bjørnøya Basin, western Barents Sea. Marine and Petroleum Geology, 13(8): 921-940.

Laberg, J.S., Andreassen, K. and Knutsen, S.M., 1998. Inferred gas hydrate on the Barents Sea shelf — a model for its formation and a volume estimate. Geo-Marine Letters, 18(1): 26-33.

Laberg, J.S. and Vorren, T.O., 1996. The middle and late Pleistocene evolution of the Bear Island Trough mouth fan. Global and Planetary Change, 12: 309-330.

Landvik, J.Y. et al., 1998. The Last Glacial Maximum of the Svalbard and the Barents Sea area: Ice sheet extent and configuration. Quarternary Science Reviews, 17: 43-75.

Leeder, M., 1999. Sedimentology and sedimentary basins - From turbulence to tectonics. Blackwell Publishing, Oxford, 592 pp.

Lein, A., Vogt, P.R., Crane, K., Egorov, A.V. and Ivanov, M., 1999. Chemical and isotopic evidence for the nature of the fluid in CH (sub 4) -containing sediments of the Hakon Mosby mud volcano. Geo Marine Letters, 19: 1-2.

Lein, A.Y. et al., 2000. Methane as a source of organic matter and carbon dioxide of carbonates at a cold seep in the Norway Sea. Geochemistry International, 38(3): 232-245.

Lien, R., 1983. Iceberg Scouring on the Norwegian Continental Shelf, Offshore Technology Conference, Houston, Texas, pp. 41-48.

Ligtenberg, J.H., 2005. Detection of fluid migration pathways in seismic data; implications for fault seal analysis. Basin Research, 17(1): 141-153.

Linjordet, A. and Olsen, R.G., 1992. The Jurassic Snohvit gas field, Hammerfest Basin, offshore northern Norway. AAPG Memoir, 54: 349-370.

Løseth, H., Gading, M. and Wensaas, L., 2008. Hydrocarbon leakage interpreted on seismic data. Marine and Petroleum Geology, In Press, Corrected Proof.

Løseth, H. et al., 2001. 1000 m long blow-out pipes. In: L. Wensaas (Editor), 63rd EAGE Conference & Technical Exibition, 11-15 June, Extended Abstract. EAGE, Amsterdam, Netherlands.

Løseth, H., Wensaas, L., Arntsen, B. and Hovland, M., 2003. Gas and fluid injection triggering shallow mud mobilization in the Hordaland Group, North Sea. In: P. Van Rensbergen, R. Hillis, A.J. Maltman and C.K. Morley (Editors), Subssurface Sediment Mobilization. Geological Society, Special Publications, London, pp. 139-157.

Madigan, M.T., Martino, J.M. and Parker, J., 2000. Brock Biology of Microorganisms 9/e. Prentice Hall, New Jersey, 1175 pp.

Magara, K., 1986. Geological Models of Petroleum Entrapment. Springer.

Marfurt, K.J., 1998. 3-D seismic effects using a running window semblance algorithm: . Geophysics, 63: 1150-1165.

Marfurt, K.J., 1999. Coherency calculations in the presence of structural dip. Geophysics, 64: 104-111.

Marfurt, K.J., Scheet, R.M., Sharp, J.A. and Harper, M.G., 1998. Suppression of the acquisition footprint for seismic sequence attribute mapping. Geophysics, 63: 1024-1035.

Mienert, J., Bünz, S., Guidard, S., Vanneste, M. and Berndt, C., 2005. Ocean bottom seismometer investigations in the Ormen Lange area offshore mid-Norway provide evidence for shallow gas layers in subsurface sediments. Marine and Petroleum Geology, 22: 287-297.

Mjelde, R. et al., 2002. Geological development of the Sorvestsnaget Basin, SW Barents Sea, from ocean bottom seismic, surface seismic and potential field data. Norsk Geologisk Tidsskrift, 82(3): 183-202.

Mueller, B. et al., 1992. Regional patterns of tectonic stress in Europe. Journal of Geophysical Research, 97(11): 783-11.

Muir, W.R., 1994. Earthquakes, strain-cycling and the mobilization of fluids. Geological Society Special Publications, 78: 85-98.

NPD, 2009. Norwegian Petroleum Directorate Factpages, http://www.npd.no/engelsk/cwi/pbl/en/index.htm.

NPD, N.P.D., 1996. Geology and Petroleum Resources in the Barents Sea. NPD.

Nyland, B., Jensen, L.N., Skagen, J., Skarpnes, O. and Vorren, T.O., 1992. Tertiary uplift and erosion in the Barents Sea: magnitude, timing and consequences. In: R.M. Larsen, H. Brekke, B.T. Larsen and E. Talleraas (Editors), Tectonic modelling and its application to petroleum geology. Norwegian Petroleum Society Spec Publ 1. Elsevier, Amsterdam, pp. 153–162.

Pedersen, S.I., Randen, T., Sonneland, L. and Steen, O., 2002. Automatic fault extraction using artificial ants, Society of Exploration Geophysicists, 72nd annual meeting. Salt Lake City, UT USA United States. Oct. Society of Exploration Geophysicists Tulsa OK United States.

Perrodon, A., 1983. Dynamics of oil and gas accumulations. Elf-Aquitaine, Pau, 368 pp.

Rice, D.D., 1992. Controls, habitat, and resource potential of ancient bacterial gas. Bacterial Gas, Editions Technip.

Rice, D.D.a.C., G.E., , 1981. Generation, accumulation, and resource potential of biogenic gas. Am. Assoc. Petrol. Geol. Bull. , 65: 1–25.

Roberts, S.J. and Nunn, J.A., 1995. Episodic fluid expulsion from geopressured sediments. Marine and Petroleum Geology, 12(2): 195-202.

Rubey, W.W. and Hubbert, M.K., 1959. Role of fluid pressure in mechanics of overthrust faulting, Part 2. Overthrust belt in geosynclinal area of western Wyoming in light of fluid-pressure hypothesis. Geological Society of America Bulletin, 70: 167-205.

Ryseth, A. et al., 2003. Cenozoic stratigraphy and evolution of the Sorvestsnaget Basin, southwestern Barents Sea. Norsk Geologisk Tidsskrift, 83(2): 107-130.

Saettem, J. et al., 1994. Cenozoic margin development and erosion of the Barents Sea; core evidence from southwest of Bjornoya. Marine Geology, 118: 3-4.

Schultz, A., Pedersen, R.B., Thorseth, I.H., Taylor, P. and Flynn, M., 2005. Fluid flow rate, temperature and heat flux at Mohns Ridge vent fields: evidence from isosampler measurements for phase separated hydrothermal circulation along the arctic ridge system, American Geophysical Union, Fall Meeting 2005.

Seront, B. et al., 1998. Laboratory characterization of hydromechanical properties of a seismogenic normal fault system. Journal of Structural Geology, 20: 865-882.

Sheriff, R.E., 2006. Encyclopedic Dictionary of Applied Geophysics. Society of Exploration Geophysicists, 429.

Sibson, R.H., 1981. Fluid flow accompanying faulting; field evidence and models. Maurice Ewing Series.

Sloan, E.D., 1990. Clathrate Hydrates of Natural gases. Marcel Dekker, New York.

Sloan, E.D., 1998. Gas Hydrates: Review of Physical/Chemical Properties. Energy & Fuels, 12: 191-196.

Smith, L., Forster, C. and Evans, J., 1990. Interaction of fault zones, fluid flow, and heat transfer at the basin scale. In: P. Neuman Shlomo and I. Neretnieks (Editors), 28th international geological congress. Washington, DC, United States.

Solheim, A. and Kristoffersen, Y., 1984. The physical environment, Western Barents Sea; Sediments above the upper regional unconformity: thickness, seismic stratigraphy and outline of the glacial history. Nor. Polarinst. Skr., 179B: 26pp.

Swarbrick, R.E., Osborne, M.J. and Yardley, G.S., 2002. Comparison of overpressure magnitude resulting from the main generating mechanisms. AAPG Memoir, 76, 1-12 pp.

Tanikawa, W. and Shimamoto, T., 2009. Comparison of Klinkenberg-corrected gas permeability and water permeability in sedimentary rocks. International Journal of Rock Mechanics and Mining Sciences, 46(2): 229-238.

Treude, T., 2003. Anaerobic oxidation of methane in marine sediments, University of Bremen, Bremen.

Treude, T., Boetius, A., Knittel, K., Wallmann, K. and Jørgensen, B.B., 2003. Anaerobic oxidation of methane above gas hydrates (Hydrate Ridge, NE Pacific). Marine Ecology Progress Series, 264: 1-14.

Vorren, T.O. and Laberg, J.S., 1996. Late glacial air temperature, oceanographic and ice sheet interactions in the southwestern Barents Sea region. In: J.T. Andrews, W.E.N. Austin, H. Bergsten and A.E. Jennings (Editors), Late Quaternary Paleoceanography of the North Atlantic Margins. Geological Society Special Publication, pp. 303-321.

Vorren, T.O. et al., 1998. The Norwegian-Greenland Sea continental margins: morphology and Late Quaternary sedimentary processes and environment. Quaternary Science Reviews, 17(1-3): 273-302.

Weibull, W., 2008. Geological Fluid Flow Systems at Nyegga of the Mid-Norwegian Margin, University of Tromsø http://hdl.handle.net/10037/1677, 104 pp.

Westbrook, G., Russell, E., Minshull, T., Nouze, H., Gailler, A., Jose, T., Ker, S., Plaza, A.,, 2008. High resolution 3D seismic investigations of hydrate-bearing fluid-escape chimneys in the Nyegga region of the Vøring Plateau, Norway, 6th International Conference on Gas Hydrates (ICGH 2008), Vancouver, British Columbia, Canada.

Whiticar, M.J., 2002. Diagenetic relationships of methanogenesis, nutrients, acoustic turbidity, pockmarks and freshwater seepages in Eckernförde Bay. Marine Geology, 182(1-2): 29-53.

Widess, M.B., 1973. How thin is a thin bed? Geophysics, 38(6): 1176-1180.

Wiprut, D. and Zoback, M.D., 2000. Fault reactivation and fluid flow along a previously dormant normal fault in the northern North Sea. Geology, 28(7): 595-598.

Woodworth-Lynas, C.M.T., Josenhans, H.W., Barrie, J.V., Lewis, C.F.M. and Parrott, D.R., 1991. The physical processes of seabed disturbance during iceberg grounding and scouring. Continental Shelf Research, 11(8-10): 939-961.

Woodworth-Lynas, C.M.T., Simms, A. and Rendell, C.M., 1985. Iceberg grounding and scouring on the Labrador Continental Shelf. Cold Regions Science and Technology, 10(2): 163-186.

Yilmaz, Ö., 1987. Seismic Data Analysis, Vol II, Second Edition. Society of Exploration Geophysicists, Tulsa, Oklahoma, 2027 pp.

Ziekus, J.G. and Wolfe, R.S., 1972. Methanobacterium thermoautotrophicum sp. n., an anaerobic, autotrophic, extreme thermophile. J. Bacteriol(109): 707-713.

Zuhlsdorff, L. and Spiess, V., 2004. Three-dimensional seismic characterization of a venting site reveals compelling indications of natural hydraulic fracturing. Geology, 32(2): 101-104.

Ødegaard, C., 2005. 3D seismisk geomorfologisk studie av paleoisstrømavsetninger på den SV Barentshavs marginen, University of Tromsø, Tromsø, 143 pp.

8 APPENDIX

Table 1. vertical zones of distorted reflections interpreted as vertical fluid migration paths.

Feat. #	Inline	Xline	Root	Top	Vert. extent [ms]	Width Inline Xline [m]	Area [m^2]	Shape	Interpreted flow path/ mechanism	Associated amplitude anomaly	Anomalous pattern and additional description
1	600	3368	Top L. Cret-L.Paleocene	Top L. Paleocene-E. Eocene	290	I 120 X 300	28274,3	Pipe	N-S Fault (20-25 ms TWT displacement)	Stacked bright spots	Vertical high amplitude zone, bright spots aligned along fault plane
2	1100	3296	Top L. Cret-L.Paleocene	Top L. Paleocene-E. Eocene	275	I 750 X 200	117809,7	Irregular cloud	Below seismic resolution	Stacked bright spots, decreased continuity, reduced frequency	Vertical high amplitude low continuity zone, root at fault/onlap
Feat. #	**Inline**	**Xline**	**Root**	**Top**	**Vert. extent [ms]**	**Width [m]**	**Area [m^2]**	**Shape**	**Interpreted flow path/ mechanism**	**Associated amplitude anomaly**	**Anomalous pattern and additional description**
3	880	3036	L. Paleocene-E. Eocene	Intra Pleistocene 1	710	I 200 X 300	47123,9	Pipe	N-S Fault/ Fractures (15 ms TWT displacement)	Dim zone below URU, Bright spots above URU, Bright spot att terminating layer (Intra Pleist. 1) and at root.	Vertical dim zone, pulldown, root point at Cretaceoous crest

Feat. #	Inline	Xline	Root	Top	Vert. extent [ms]	Width [m]	Area [m^2]	Shape	Interpreted flow path/ mechanism	Associated amplitude anomaly	Anomalous pattern and additional description
4	284	3412	E.Eocene	R7	600	I200 X400	62831,9	Follows fault	N-S Fault (10 ms TWT displacement)	Flags along reflections at sides of fault	Vertical low continuity zone, root at E. Eocene fan
5	348	3828	E.Eocene	E.Eocene	310	I 250 X 300	58904,9	Follows fault	N-S Fault (10 ms TWT displacement)	Stacked bright spots, Reduced frequency	Vertical high amplitude zone, pulldown at underlying reflection (E. Eocene Fan), root at E. Eocene fan
6	412	3912	E.Eocene	URU/R7	610	I 100 X 300	23561,9	Scattered	N-S Fault (20 ms TWT displacement)	Bright spots	Bright spots aligned along fault plane, root at E. Eocene fan
7	614	3584	E.Eocene	URU/R7	525	I 350 X 700	192422,5	Irregular cloud	Below seismic resolution	Stacked bright spots, decreased continuity, reduced frequency	Vertical high amplitude low continuity zone, root at E. Eocene fan
8	892	3728	E.Eocene	URU/R7	560	I 800 X 1000	628318,5	Irregular cloud/ chimney	Diffuse/ Darcy flow/ Below seismic resolution	Increased amplitude	Vertical high amplitude zone, chaotic reflections, pulldown and weakening of amplitude of underlying reflection (E. Eocene Fan), root at E. Eocene fan

Feat. #	Inline	Xline	Root	Top	Vert. extent [ms]	Width [m]	Area [m^2]	Shape	Interpreted flow path/ mechanism	Associated amplitude anomaly	Anomalous pattern and additional description
9	276	3076	R1	Intra Pleist 1	210	I 600 X 500	235619,4	Irregular cloud/ column	Diffuse/ Darcy flow	Decreased continuity, bright spots at R1, Intra Pleist. 2 and Intra Pleist. 1.	Vertical high amplitude zone, pulldown, random pattern, root at mass movement deposits/toplap base Pleistocene
10	660	2564	R1	Intra Pleist 1	235	I 490 X 250	96211,3	Irregular Column/ pipe	Diffuse/ Darcy flow	Decreased continuity and frequency, bright spots at R1, Intra Pleist. 2 and Intra Pleist. 1.	Random pattern, root at mass movement deposits/toplap base Pleistocene
11	738	2876	R1	Intra Pleist 1	260	I 430 X 250	84430,3	Irregular Column/ pipe	Diffuse/ Darcy flow	Decreased continuity amplitude and frequency, bright spot at Intra Pleist. 1	Vertical low amplitude low continuity zone, random reflections, root at toplap base Pleistocene
12	818	2728	R1	Intra Pleist 1	310	I 290 X 200	45553,1	Pipe	Diffuse/ Darcy flow	Decreased continuity and amplitude, bright spot at Intra Pleist. 1	Vertical low amplitude low continuity zone, pulldown, root at toplap base Pleistocene
13	868	2188	R1	Intra Pleist 1	260	I 240 X 350	65973,4	Irregular cloud/ column	Diffuse/ Darcy flow	Decreased continuity and frequency, bright spot at Intra Pleist. 1 and Intra Pleist. 2	Random pattern, root at mass movement deposits/toplap base Pleistocene

14	1044	2436	R!	Intra Pleist 1	235	I 150 X 200	23561,9	Pipe	Diffuse/ Darcy flow	Stacked bright spots, bright spot at Intra Pleist. 2	Vertical high amplitude zone
15	1628	3308	URU (Possibly E. Eocene/ Cret.)	Intra Pleist 1	130	I 660 X 430	222896,0	Irregular Column/ pipe	Diffuse/ Darcy flow	Bright spots at URU and Intra Pleist. 1	Vertical high amplitude low continuity zone, Pulldown and weakening of URU reflection.
16	1628	3524	URU (Possibly E. Eocene/ Cret.)	Intra Pleist 1	110	I 230 X 200	36128,3	Irregular Column/ pipe	Diffuse/ Darcy flow	Bright spots at URU and Intra Pleist. 1	Vertical high amplitude low continuity zone
17	1702	3340	URU	Intra Pleist 1	105	I 1900 X 900	1343030, 9	Irregular cloud/ chimney	Diffuse/ Darcy flow	Bright spot at URU, weakening of Intra Pleist. 1 reflection	Vertical high amplitude low continuity zone
18	1730	1312	R1	Intra Pleist 1	230	I 200 X 700	109955,7	Irregular cloud/ column	Diffuse/ Darcy flow	Bright spot at root and Intra Pleist. 2	Vertical high amplitude low continuity zone. Top at mass movement deposit Intra Pleist 1, root at mass movement deposits/toplap base Pleistocene
19	1730	1400	R1	Intra Pleist 1	270	I 150 X 1000	117809,7	Irregular Column/ pipe	Diffuse/ Darcy flow	Bright spot at root and Intra Pleist. 2	Vertical high amplitude low continuity zone, root at mass movement deposits/toplap base Pleistocene

20	1756	3244	URU	Intra Pleist 1	120	I 1100 X 450	388772,1	Irregular cloud/ chimney	Diffuse/ Darcy flow	Bright spot at Intra Pleist. 1 and URU, dim spot on URU reflection directly underneath the feature.	Vertical high amplitude, low frequency zone. Pulldown and weakening of underlying URU reflection
21	1796	3292	URU	Intra Pleist 1	110	I 550 X 2000	863938,0	Irregular cloud/ column	Diffuse/ Darcy flow	Bright spots at Intra Pleist. 1 and URU, dim spot on URU reflection directly underneath the feature.	Vertical high amplitude zone, random pattern.
22	1880	3196	URU	Intra Pleist 1	120	I 350 X 180	49480,1	Irregular cloud/ column	Diffuse/ Darcy flow	Bright spots at Intra Pleist. 1 and URU,	Vertical high amplitude zone, random pattern.
23	1880	3372	URU	Intra Pleist 1	100	I 400 X 100	31415,9	Irregular cloud/ column	Diffuse/ Darcy flow	Bright spots at Intra Pleist. 1 and URU,	Vertical high amplitude zone,, random pattern.
Feat. #	**Inline**	**Xline**	**Root**	**Top**	**Vert. extent [ms]**	**Width [m]**	**Area [m^2]**	**Shape**	**Interpreted flow path/ mechanism**	**Associated amplitude anomaly**	**Anomalous pattern and additional description**
24	720	1568	R5	Seafloor	280	I 450 X 300	106028,8	Irregular Column/ pipe	Diffuse/ Darcy flow	Bright spots at Intra Pleist. 1, Intra Pleist. 2 and R5	Vertical low continuity low frequency zone,, random pattern. Root at mass movement deposits/toplap base Pleistocene.

25	1124	2474	URU (Possibly E. Eocene)	Seafloor	380	I 250 X 300	58904,9	Pipe	Focused fluid flow, fractures	Bright spot at URU	Vertical wipe-out zone, root associated with termination of Pliocene wedge.
26	1916	1748	R1	Seafloor	340	I 1000 X >800	628318,5	Irregular chimney/ pipe	Focused fluid flow, fractures	Scattered bright spots W of pipe/chimney	Vertical low amplitude zone with ass. Stacked bright spots in W part. Root at mass movement deposits/toplap base Pleistocene.
Feat. #	**Inline**	**Xline**	**Root**	**Top**	**Vert. extent [ms]**	**Width [m]**	**Area [m^2]**	**Shape**	**Interpreted flow path/ mechanism**	**Associated amplitude anomaly**	**Anomalous pattern and additional description**
27	226	2884	Intra Pleist 2	Intra Pleist 1	110	I 250 X 200	39269,9	Irregular Column	Diffuse/ Darcy flow	Bright spots at Intra Pleist. 1 and Intra Pleist. 2	Vertical disturbed zone. 50 ms below Intra Pleist 2 lies toplap base Pleistocene which probably is the originating area of the vertical feature.
28	248	3148	Intra Pleist 2	Intra Pleist 1	110	I 300 X 200	47123,9	Irregular cloud/ column	Diffuse/ Darcy flow	Bright spots at Intra Pleist. 1 and Intra Pleist. 2	Vertical low frequency disturbed zone
29	770	2212	Intra Pleist 2	Intra Pleist 1	120	I 150 X 500	58904,9	Irregular Column/ pipe	Diffuse/ Darcy flow	Stacked high amplitude anomalies. Bright spots at Intra Pleist. 1 and Intra Pleist. 2	Vertical high amplitude disturbed zone.

Feat. #	Inline	Xline	Root	Top	Vert. extent [ms]	Width [m]	Area [m^2]	Shape	Interpreted flow path/ mechanism	Associated amplitude anomaly	Anomalous pattern and additional description
30	528	956	R1	Seafloor	280	I 850 X 650	433932,5	Chimney/pipe	Diffuse/ Darcy flow	Dim zone	Vertical low amplitude low frequency zone. Terminates in a large pockmark. Root at base Pliocene toplap. Pull-down.

Table 2. Scenario 1

Feature #	Width Inline [m]	Width Xline [m]	Area [m2]	Flow mechanism	Typical flow velocity (Krooss et al., 1996), (Roberts et al., 1995)	Flow Low [m3/year]	Flow High [m3/year]	Total per level (low flow) [m3/year]	Total per level (high flow) [m3/year]	Sum (low flow) [m3/year]	Sum (high flow) [m3/year]
1	120	300	28274,3	N-S Fault	100–1000 m3/km2/year	2,8	28,3				
2	750	200	117809,7	Below seis resolution	100–1000 m3/km2/year	11,8	117,8				
								14,6	146,1		
3	200	300	47123,9	N-S Fault/ Fractures	100–1000 m3/km2/year	4,7	47,1				
								4,7	47,1		
4	200	400	62831,9	N-S Fault/ Fractures	100–1000 m3/km2/year	6,3	62,8				
5	250	300	58904,9	N-S Fault/ Fractures	100–1000 m3/km2/year	5,9	58,9				
6	100	300	23561,9	N-S Fault/ Fractures	100–1000 m3/km2/year	2,4	23,6				
7	350	700	192422,5	Below seismic resolution	100–1000 m3/km2/year	19,2	192,4				
8	800	1000	628318,5	Below seismic resolution	100–1000 m3/km2/year	62,8	628,3				
								96,6	966,0	115,9	1159,2
9	600	500	235619,4	Diffuse/ Darcy flow	100–1000 m3/km2/year	23,6	235,6				
10	490	250	96211,3	Diffuse/ Darcy flow	100–1000 m3/km2/year	9,6	96,2				
11	430	250	84430,3	Diffuse/ Darcy flow	100–1000 m3/km2/year	8,4	84,4				
12	290	200	45553,1	Diffuse/ Darcy flow	100–1000 m3/km2/year	4,6	45,6				
13	240	350	65973,4	Diffuse/ Darcy flow	100–1000 m3/km2/year	6,6	66,0				
14	150	200	23561,9	Diffuse/ Darcy flow	100–1000 m3/km2/year	2,4	23,6				
15	660	430	222896,0	Diffuse/ Darcy flow	100–1000 m3/km2/year	22,3	222,9				
16	230	200	36128,3	Diffuse/ Darcy flow	100–1000 m3/km2/year	3,6	36,1				
17	1900	900	1343030,9	Diffuse/ Darcy flow	100–1000 m3/km2/year	134,3	1343,0				
18	200	700	109955,7	Diffuse/ Darcy flow	100–1000 m3/km2/year	11,0	110,0				
19	150	1000	117809,7	Diffuse/ Darcy flow	100–1000 m3/km2/year	11,8	117,8				
20	1100	450	388772,1	Diffuse/ Darcy flow	100–1000 m3/km2/year	38,9	388,8				
21	550	2000	863938,0	Diffuse/ Darcy flow	100–1000 m3/km2/year	86,4	863,9				
22	350	180	49480,1	Diffuse/ Darcy flow	100–1000 m3/km2/year	4,9	49,5				
23	400	100	31415,9	Diffuse/ Darcy flow	100–1000 m3/km2/year	3,1	31,4				
								371,5	3714,8		
24	450	300	106028,8	Diffuse/ Darcy flow	100–1000 m3/km2/year	10,6	106,0				
25	250	300	58904,9	Diffuse/ Darcy flow/ Fractures	100–1000 m3/km2/year	5,9	58,9				
26	1000	800	628318,5	Diffuse/ Darcy flow/ Fractures	100–1000 m3/km2/year	62,8	628,3				
								79,3	793,3		
27	250	200	39269,9	Diffuse/ Darcy flow	100–1000 m3/km2/year	3,9	39,3				
28	300	200	47123,9	Diffuse/ Darcy flow	100–1000 m3/km2/year	4,7	47,1				
29	150	500	58904,9	Diffuse/ Darcy flow	100–1000 m3/km2/year	5,9	58,9				
								14,5	145,3		
30	850	650	433932,5	Diffuse/ Darcy flow	100–1000 m3/km2/year	43,4	433,9				
								43,4	433,9	508,7	5087,3
Total			6246507,2			624,7	6246,5				

Table 3. Scenario 2

Feature #	Width Inline [m]	Width Xline [m]	Area [m2]	Flow mechanism	Modified fluid flow velocities	Flow Low [m3/year]	Flow High [m3/year]	Total per level (low flow) [m3/year]	Total per level (high flow) [m3/year]	Sum (low flow) [m3/year]	Sum (high flow) [m3/year]
1	120	300	28274,3	N-S Fault	10 000–100 000 m3/km2/year	282,7	2827,4				
2	750	200	117809,7	Below seis resolution	10 000–100 000 m3/km2/year	1178,1	11781,0				
								1460,8	14608,4		
3	200	300	47123,9	N-S Fault/ Fractures	10 000–100 000 m3/km2/year	471,2	4712,4				
								471,2	4712,4		
4	200	400	62831,9	N-S Fault/ Fractures	10 000–100 000 m3/km2/year	628,3	6283,2				
5	250	300	58904,9	N-S Fault/ Fractures	10 000–100 000 m3/km2/year	589,0	5890,5				
6	100	300	23561,9	N-S Fault/ Fractures	10 000–100 000 m3/km2/year	235,6	2356,2				
7	350	700	192422,5	Below seismic resolution	10 000–100 000 m3/km2/year	1924,2	19242,3				
8	800	1000	628318,5	Below seismic resolution	10 000–100 000 m3/km2/year	6283,2	62831,9				
								9660,4	96604,0	11592,5	115924,8
9	600	500	235619,4	Diffuse/ Darcy flow	10 000–100 000 m3/km2/year	2356,2	23561,9				
10	490	250	96211,3	Diffuse/ Darcy flow	10 000–100 000 m3/km2/year	962,1	9621,1				
11	430	250	84430,3	Diffuse/ Darcy flow	10 000–100 000 m3/km2/year	844,3	8443,0				
12	290	200	45553,1	Diffuse/ Darcy flow	10 000–100 000 m3/km2/year	455,5	4555,3				
13	240	350	65973,4	Diffuse/ Darcy flow	10 000–100 000 m3/km2/year	659,7	6597,3				
14	150	200	23561,9	Diffuse/ Darcy flow	10 000–100 000 m3/km2/year	235,6	2356,2				
15	660	430	222896,0	Diffuse/ Darcy flow	10 000–100 000 m3/km2/year	2229,0	22289,6				
16	230	200	36128,3	Diffuse/ Darcy flow	10 000–100 000 m3/km2/year	361,3	3612,8				
17	1900	900	1343030,9	Diffuse/ Darcy flow	10 000–100 000 m3/km2/year	13430,3	134303,1				
18	200	700	109955,7	Diffuse/ Darcy flow	10 000–100 000 m3/km2/year	1099,6	10995,6				
19	150	1000	117809,7	Diffuse/ Darcy flow	10 000–100 000 m3/km2/year	1178,1	11781,0				
20	1100	450	388772,1	Diffuse/ Darcy flow	10 000–100 000 m3/km2/year	3887,7	38877,2				
21	550	2000	863938,0	Diffuse/ Darcy flow	10 000–100 000 m3/km2/year	8639,4	86393,8				
22	350	180	49480,1	Diffuse/ Darcy flow	10 000–100 000 m3/km2/year	494,8	4948,0				
23	400	100	31415,9	Diffuse/ Darcy flow	10 000–100 000 m3/km2/year	314,2	3141,6				
								37147,8	371477,6		
24	450	300	106028,8	Diffuse/ Darcy flow	10 000–100 000 m3/km2/year	1060,3	10602,9				
25	250	300	58904,9	Diffuse/ Darcy flow / Fractures	10 000–100 000 m3/km2/year	589,0	5890,5				
26	1000	800	628318,5	Diffuse/ Darcy flow / Fractures	10 000–100 000 m3/km2/year	6283,2	62831,9				
								7932,5	79325,2		
27	250	200	39269,9	Diffuse/ Darcy flow	10 000–100 000 m3/km2/year	392,7	3927,0				
28	300	200	47123,9	Diffuse/ Darcy flow	10 000–100 000 m3/km2/year	471,2	4712,4				
29	150	500	58904,9	Diffuse/ Darcy flow	10 000–100 000 m3/km2/year	589,0	5890,5				
								1453,0	14529,9		
30	850	650	433932,5	Diffuse/ Darcy flow	10 000–100 000 m3/km2/year	4339,3	43393,2				
								4339,3	43393,2	50872,6	508726,0
Total			6246507,2			62465,1	624650,7				

Table 4. Scenario 3

Feature	Width Inline [m]	Width Xline [m]	Area [m2]	Flow mechanism	Fault Displacement in m at 2700m/s (ms)	Modified typical flow velocity (Krooss et al., 1996), (Roberts et al., 1995)	Flow Low [m3/year]	Flow High [m3/year]	Total per level (low flow) [m3/year]	Total per level (high flow) [m3/year]	Sum (low flow) [m3/year]	Sum (high flow) [m3/year]
1	0,5	300	117,8	N-S Fault	27 m	$2*10^8$–$2.5*10^9$ m3/km2/year	23561,9	294524,3				
2	750	200	117809,7	Below seis resolution		10000–100000 m3/km2/year	1178,1	11781,0				
									24740,0	306305,3		
3	0,5	300	117,8	N-S Fault/ Fractures	20,25 m	$2*10^8$–$2.5*10^9$ m3/km2/year	23561,9	294524,3				
									23561,9	294524,3		
4	0,5	400	157,1	N-S Fault/ Fractures	14 m	$2*10^8$–$2.5*10^9$ m3/km2/year	31415,9	392699,1				
5	0,5	300	117,8	N-S Fault/ Fractures	14 m	$2*10^8$–$2.5*10^9$ m3/km2/year	23561,9	294524,3				
6	0,5	300	117,8	N-S Fault/ Fractures	20,25 m	$2*10^8$–$2.5*10^9$ m3/km2/year	23561,9	294524,3				
7	350	700	192422,5	Below seismic resolution		10000–100000 m3/km2/year	1924,2	19242,3				
8	800	1000	628318,5	Below seismic resolution		10000–100000 m3/km2/year	6283,2	62831,9				
									86747,2	1063821,8	135049,2	1664651,4
9	600	500	235619,4	Diffuse/ Darcy flow		10000–100000 m3/km2/year	2356,2	23561,9				
10	490	250	96211,3	Diffuse/ Darcy flow		10000–100000 m3/km2/year	962,1	9621,1				
11	430	250	84430,3	Diffuse/ Darcy flow		10000–100000 m3/km2/year	844,3	8443,0				
12	290	200	45553,1	Diffuse/ Darcy flow		10000–100000 m3/km2/year	455,5	4555,3				
13	240	350	65973,4	Diffuse/ Darcy flow		10000–100000 m3/km2/year	659,7	6597,3				
14	150	200	23561,9	Diffuse/ Darcy flow		10000–100000 m3/km2/year	235,6	2356,2				
15	660	430	222896,0	Diffuse/ Darcy flow		10000–100000 m3/km2/year	2229,0	22289,6				
16	230	200	36128,3	Diffuse/ Darcy flow		10000–100000 m3/km2/year	361,3	3612,8				
17	1900	900	1343030,9	Diffuse/ Darcy flow		10000–100000 m3/km2/year	13430,3	134303,1				
18	200	700	109955,7	Diffuse/ Darcy flow		10000–100000 m3/km2/year	1099,6	10995,6				
19	150	1000	117809,7	Diffuse/ Darcy flow		10000–100000 m3/km2/year	1178,1	11781,0				
20	1100	450	388772,1	Diffuse/ Darcy flow		10000–100000 m3/km2/year	3887,7	38877,2				
21	550	2000	863938,0	Diffuse/ Darcy flow		10000–100000 m3/km2/year	8639,4	86393,8				
22	350	180	49480,1	Diffuse/ Darcy flow		10000–100000 m3/km2/year	494,8	4948,0				
23	400	100	31415,9	Diffuse/ Darcy flow		10000–100000 m3/km2/year	314,2	3141,6				
									37147,8	371477,6		
24	450	300	106028,8	Diffuse/ Darcy flow		10000–100000 m3/km2/year	1060,3	10602,9				
25	250	300	58904,9	Diffuse/ Darcy flow/ Fractures		10000–100000 m3/km2/year	589,0	5890,5				
26	1000	800	628318,5	Diffuse/ Darcy flow/ Fractures		10000–100000 m3/km2/year	6283,2	62831,9				
									7932,5	79325,2		
27	250	200	39269,9	Diffuse/ Darcy flow		10000–100000 m3/km2/year	392,7	3927,0				
28	300	200	47123,9	Diffuse/ Darcy flow		10000–100000 m3/km2/year	471,2	4712,4				
29	150	500	58904,9	Diffuse/ Darcy flow		10000–100000 m3/km2/year	589,0	5890,5				
									1453,0	14529,9		
30	850	650	433932,5	Diffuse/ Darcy flow		10000–100000 m3/km2/year	4339,3	43393,2				
									4339,3	43393,2	50872,6	508726,0
Total			6026438,6				185921,8	2173377,4				